

**SIMULATION AND EXPERIMENTAL PREDICTIONS FOR THE
STRUCTURAL RESPONSE OF SATELLITES**

A Thesis

by

ANGELA NOEL MCLELLAND

Submitted to the Office of Graduate and Professional Studies of
Texas A&M University
in partial fulfillment of the requirements for the degree of

MASTER OF SCIENCE

Chair of Committee,	Helen Reed
Committee Members,	Srinivas Vadali
	Luciana Barroso
Head of Department,	Rodney Bowersox

December 2013

Major Subject: Aerospace Engineering

Copyright 2013 Angela McLelland

ABSTRACT

This research investigated the structural response of satellites and space rated payloads. Throughout the work, SolidWorks Simulation was utilized to subject the aforementioned systems to both experimental test loads as well as program specific flight environments. While the methods presented within this document were exclusively employed with the SolidWorks Simulation software, all finite element analysis (FEA) techniques and computer aided design (CAD) best practices discussed are valid for a variety of commercially available CAD packages. Primarily, the programs under investigation were the Low earth Orbiting Navigation Experiment for Spacecraft Testing Autonomous Rendezvous and docking (LONESTAR) and Space-based Telescopes for Actionable Refinement of Ephemeris (STARE) programs. Both investigations studied satellite responses due to free and forced vibrations as well as various thermal environments and loading. Additionally, where experimental data was available, simulation solutions were validated against CAD generated values and evaluated for accuracy.

Ultimately, the natural frequency and random vibration responses of four systems are presented as part of this research and the sensitivity of these results, due to various modeling variables, is discussed. The transient and steady state thermal profiles of two satellite flight configurations are also presented in an effort to predict on orbit thermal conditions. The CAD tool was evaluated and deemed appropriate for investigative studies within the laboratory.

DEDICATION

For my mother, Barbara S. Angelucci, who has shown unconditional love, support, and sacrifice and to whom I will be eternally grateful

ACKNOWLEDGEMENTS

I would like to extend my sincerest gratitude to Dr. Barroso and Dr. Vadali for serving on my committee. Their continued flexibility and approachability was paramount to my success. Additionally, this work would not have been possible without sponsor support and leadership. NASA Johnson Space Center and Lawrence Livermore National Laboratory are prime examples of industry excellence and I appreciate the opportunity to have supported such technically relevant projects. Likewise, I want to recognize all the hard work and countless hours AggieSat members contributed which made this research possible. The team's dedication and passion sustain AggieSat and truly enhanced my graduate school experience.

On a personal note, I would also like to acknowledge Ms. Rebecca Marianno for all of her guidance throughout my time at Texas A&M. Without Rebecca's organization, cheery disposition, and willingness to help, I would have missed several important deadlines and smiled a lot less. Also, I owe a huge thank you to my friend and coworker Hyder Hasan. To list the times Hyder exceeded my expectations would undoubtedly surpass the space allotted. I will forever be grateful for his unwavering support.

Lastly, I would like to thank my committee chair, advisor, and role model, Dr. Helen Reed. Dr. Reed gave me the unquantifiable opportunity to further my education while researching a topic I have always loved. Throughout my time as a graduate student, Dr. Reed defined by example the professional woman I hope to become and showed unimaginable generosity, patience and kindness.

NOMENCLATURE

AFM	Autonomous Flight Manager
AFRL	Air Force Research Laboratory
AGS2/4	AggieSat2/4
AGSL	AggieSat Laboratory
Al 6061-T6	Aluminum 6061-T6
ARD	Autonomous Rendezvous and Docking
ASD	Acceleration Spectral Density
CI/II	Colony I/II
CAD	Computer Aided Design
CDH	Computer and Data Handling
CMOS	Complementary Metal-Oxide-Semiconductor
DOD	Department Of Defense
DOF	Degrees Of Freedom
DRAGON	Dual RF Astrodynamic GPS Orbital Navigator
EDU	Engineering Design Unit
EPS	Electrical and Power System
FEA	Finite Element Analysis
FS	Factor of Safety
GN&C	Guidance Navigation and Control
GPS	Global Positioning System

IMU	Inertial Measurement Unit
IR	Infrared
ISS	International Space Station
JEM	Japanese Experiment Module
LLNL	Lawrence Livermore National Laboratory
LONESTAR	Low earth Orbiting Navigation Experiment for Spacecraft Testing Autonomous Rendezvous and docking
LU	Lower triangle and Upper triangle
NASA	National Aeronautics and Space Administration
NPS	Naval Postgraduate School
ODE	Ordinary Differential Equation
OUTSat	Operationally Unique Technology Satellite
PCB	Printed Circuit Board
P-Pod	Poly-Picosatellite Orbital Deployer
PSD	Power Spectral Density
PSI	Pounds per Square Inch
RCS	Reaction Control System
RMS	Root Mean Square
SMAD	Space Mission Analysis and Design
SSPL	Space Shuttle Picosat Launcher
STARE	Space-based Telescopes for Actionable Refinement of Ephemeris
TAMU	Texas A&M University

TEC	Thermoelectric Cooler
TIM	Technical Interchange Meeting
TML	Tool Maturity Level
UT	University of Texas
V2/3	Version 2/3
V&V	Validation and Verification

TABLE OF CONTENTS

	Page
ABSTRACT	ii
DEDICATION	iii
ACKNOWLEDGEMENTS	iv
NOMENCLATURE	v
TABLE OF CONTENTS	viii
LIST OF FIGURES	xii
LIST OF TABLES	xvi
1. INTRODUCTION	1
1.1 Thesis Organization	2
2. BACKGROUND	5
2.1 Trends in the Aerospace Industry and Academia	5
2.2 Programmatic Background	6
2.2.1 The Low Earth Orbiting Navigation Experiment for Spacecraft Testing Autonomous Rendezvous and Docking Campaign	7
2.2.2 The Space-based Telescopes for Actionable Refinement of Ephemeris Campaign	9
2.3 Computer Aided Design Packages	10
2.3.1 SolidWorks in Other Applications	12
3. MOTIVATION	15
3.1 Validation and Verification of Simulation Results	16
3.2 Tool Maturity Level Evaluation	17

3.3	Objectives	20
4.	METHODOLOGY	21
4.1	Governing Equations	21
4.1.1	Strain-Stress Relationship	21
4.1.2	Free and Forced Vibration	24
4.1.3	Steady State and Transient Heat Transfer .	26
4.2	Mesh Generation	28
4.3	Finite Element Analysis Solvers	32
4.3.1	Direct Methods	33
4.3.2	Iterative Methods	34
4.4	Simulated Loading	34
4.5	General Processes for Finite Element Analysis	36
4.5.1	Iterative Simulation Practices	37
4.6	Sources of Uncertainty	38
4.6.1	Experimental Uncertainty	39
4.6.2	Simulation Uncertainty	39
4.7	Validation Metrics and Post Processing	45
5.	COMPUTER AIDED DESIGN MODELS AND VALIDATION METRICS	47
5.1	The Space-based Telescopes for Actionable Refinement of Ephemeris Structural Payloads and Test Pod Models ...	47
5.1.1	Version 2 Computer Aided Design Model	48
5.1.2	Version 3 Computer Aided Design Model	49
5.1.3	Version 2 Boundary Conditions and Model Constraints	51
5.1.4	Version 2 Simulated Loading	52
5.1.5	Version 2 Mesh Convergence	54
5.1.6	Version 2 Validation Metrics	55
5.1.7	Version 3 Boundary Conditions and Model Constraints	56
5.1.8	Version 3 Simulated Loading	57
5.1.9	Version 3 Mesh Convergence	59
5.1.10	Version 3 Validation Metrics	60
5.2	The Space-based Telescopes for Actionable Refinement of Ephemeris Thermal Models	61
5.2.1	Colony I and Colony II Thermal Simulations	63
5.2.2	Thermal Computer Aided Design Models .	64
5.2.3	Thermal Inputs and Boundary Conditions .	67
5.2.4	Thermal Validation Metrics	72

5.3	The Low Earth Orbiting Navigation Experiment for Spacecraft Testing Autonomous Rendezvous and Docking AggieSat4 Structural Model	73
5.3.1	AggieSat4 Computer Aided Design Model	73
5.3.2	AggieSat4 Boundary Conditions and Model Constraints	75
5.3.3	AggieSat4 Simulated Loading	77
5.3.4	AggieSat4 Mesh Convergence	79
5.3.5	AggieSat4 Validation Metrics	80
5.4	The Low Earth Orbiting Navigation Experiment for Spacecraft Testing Autonomous Rendezvous and Docking AggieSat2 Model	81
5.4.1	AggieSat2 Computer Aided Design Model	82
5.4.2	AggieSat2 Boundary Conditions and Model Constraints	84
5.4.3	AggieSat2 Simulated Loading	85
5.4.4	AggieSat2 Mesh Convergence	86
5.4.5	AggieSat2 Validation Metrics	88
6.	RESULTS	90
6.1	Version 2 Structural Results	90
6.1.1	Version 2 Natural Frequency	90
6.1.2	Version 2 Random Vibration (X-Axis)	92
6.1.3	Version 2 Random Vibration (Y-Axis)	96
6.1.4	Version 2 Random Vibration (Z-Axis)	98
6.2	Version 3 Structural Results	100
6.2.1	Version 3 Natural Frequency	100
6.2.2	Version 3 Random Vibration (X-Axis)	102
6.2.3	Version 3 Random Vibration (Y-Axis)	104
6.2.4	Version 3 Random Vibration (Z-Axis)	105
6.3	Colony I Thermal Results	106
6.3.1	Colony I $\beta=0^\circ$ Case	107
6.3.2	Colony I $\beta=90^\circ$ Case	109
6.3.3	Colony I Comparison of $\beta=0^\circ$ and $\beta=90^\circ$.	111
6.3.4	Proposed Thermal Management System ...	112
6.4	Colony II Thermal Results	115
6.4.1	Colony II $\beta=90^\circ$ Case	115
6.5	AggieSat4 Structural Results	116
6.5.1	AggieSat4 Natural Frequency	117
6.5.2	AggieSat4 Random Vibration (X-Axis) ...	118
6.5.3	AggieSat4 Random Vibration (Y-Axis) ...	121
6.5.4	AggieSat4 Random Vibration (Z-Axis) ...	124

6.6	AggieSat2 and DragonSat Structural Results	127
6.6.1	AggieSat2 and DragonSat Natural Frequency	127
6.6.2	DragonSat Random Vibration (X-Axis) ...	130
6.6.3	DragonSat Random Vibration (Y-Axis) ...	133
6.6.4	DragonSat Random Vibration (Z-Axis) ...	134
7.	CONCLUSIONS	136
7.1	Version 2 Investigation	138
7.1.1	Version 2 Sensitivity Analysis	140
7.2	Version 3 Investigation	145
7.3	Colony I and Colony II Investigations	146
7.4	AggieSat4 Investigation	146
7.5	AggieSat2 Investigation	147
7.6	Recommendations	149
	REFERENCES	150
	APPENDIX	156

LIST OF FIGURES

		Page
Figure 4.1	Spring/damper system	25
Figure 4.2	Elemental mesh types	29
Figure 4.3	Run time trend for increased node counts	31
Figure 4.4	Progression of steps taken in SolidWorks from component design and modeling to analysis	37
Figure 4.5	Relative uncertainty of FEA processes	40
Figure 4.6	X-Axis results for three configurations: fully constrained bottom plane, roller/slider bottom plane and fixed holes, and fixed holes	42
Figure 4.7	Y-Axis results for three configurations: fully constrained bottom plane, roller/slider bottom plane and fixed holes, and fixed holes	44
Figure 5.1	Physical test pod and modeled test pod with coordinate system ..	49
Figure 5.2	OUTSat test level profile as applied in SolidWorks	53
Figure 5.3	STARE V2 mesh convergence data	54
Figure 5.4	GEMSat X-Axis, Y-Axis, and Z-Axis test level profile as applied in SolidWorks	58
Figure 5.5	STARE V3 mesh convergence data	59
Figure 5.6	Simplified Colony I and Colony II models	62
Figure 5.7	Panel nomenclature of Colony I and Colony II configurations ...	68
Figure 5.8	$\beta=90^\circ$, steady-state scenario and spacecraft orientations	69
Figure 5.9	Colony I $\beta=0^\circ$, transient scenario and spacecraft orientation	70
Figure 5.10	Isometric view of AGS4 structure before and after de-featuring	

	with +Z constraints shown	74
Figure 5.11	Bottom panel showing AGS4 feet and Cyclops knob and model constraints	76
Figure 5.12	Dragon PSD test levels and attenuated profiles as applied in SolidWorks	78
Figure 5.13	AGS4 mesh convergence data	79
Figure 5.14	AGS2 flight unit, full detail CAD model, and structural model, de-featured internally and externally	82
Figure 5.15	Interior of AGS2 flight unit and CAD model	83
Figure 5.16	SSPL EDU and SSPL CAD model	84
Figure 5.17	DragonSat X-Axis, Y-Axis, and Z-Axis test level profile as applied in SolidWorks	86
Figure 5.18	DragonSat mesh convergence data	87
Figure 5.19	AGS2 mesh convergence data	87
Figure 6.1	LLNL V2 4 th mode natural frequency	91
Figure 6.2	LLNL V2 -X Face: PSD probe locations and physical test pod model with accelerometers	93
Figure 6.3	LLNL V2 +X Face: PSD probe locations and physical test pod model with accelerometers	94
Figure 6.4	LLNL V2 PSD response for X-Axis excitation	95
Figure 6.5	LLNL V2 PSD probe locations and physical test pod model with accelerometers	96
Figure 6.6	LLNL V2 PSD response for Y-Axis excitation	97
Figure 6.7	LLNL V2 PSD probe locations and +X/-Z faces of the physical test pod model with accelerometers	98
Figure 6.8	LLNL V2 PSD response for Z-Axis excitation	99

Figure 6.9	LLNL V3 1 st mode natural frequency	101
Figure 6.10	LLNL V3 PSD probe locations	102
Figure 6.11	LLNL V3 PSD response for X-Axis excitation	103
Figure 6.12	LLNL V3 PSD response for Y-Axis excitation	104
Figure 6.13	LLNL V3 PSD response for Z-Axis excitation	106
Figure 6.14	Heat strap potential mounting locations	106
Figure 6.15	LLNL CI Transient thermal results	107
Figure 6.16	LLNL CI Transient response of primary interface locations	108
Figure 6.17	LLNL CI Transient response of the X facing frame/wall	109
Figure 6.18	LLNL CI Steady state thermal results	110
Figure 6.19	LLNL CI Temperature variation along the X frame/wall cross bar	112
Figure 6.20	Resistance models for Configuration I and Configuration II	113
Figure 6.21	Thermal strap configurations	114
Figure 6.22	LLNL CII Steady state thermal results	115
Figure 6.23	AGS4 1 st mode natural frequency	118
Figure 6.24	AGS4 PSD X-Axis probe locations	120
Figure 6.25	AGS4 PSD response for X-Axis excitation	121
Figure 6.26	AGS4 PSD Y-Axis probe locations	123
Figure 6.27	AGS4 PSD response for Y-Axis excitation	124
Figure 6.28	AGS4 PSD Z-Axis probe locations	126
Figure 6.29	AGS4 PSD response for Z-Axis excitation	127
Figure 6.30	AGS2 1 st mode natural frequency	128

Figure 6.31	DragonSat and SSPL 1 st mode natural frequency	130
Figure 6.32	SSPL rear PSD probe locations and physical model with accelerometers	131
Figure 6.33	SSPL side PSD probe locations and physical model with accelerometers	131
Figure 6.34	DragonSat and SSPL PSD response for X-Axis excitation	132
Figure 6.35	DragonSat and SSPL PSD response for Y-Axis excitation	133
Figure 6.36	DragonSat and SSPL PSD response for Z-Axis excitation	134
Figure 7.1	LLNL V2 PSD response for X-Axis excitation, Sensor A	141
Figure 7.2	LLNL V2 PSD response for X-Axis excitation, Sensor B	141
Figure 7.3	LLNL V2 PSD response for X-Axis excitation, Sensor D	142
Figure 7.4	LLNL V2 PSD response for Y-Axis excitation, +Y face sensor ..	143
Figure 7.5	LLNL V2 PSD response for Y-Axis excitation, +X face sensor ..	143
Figure 7.6	LLNL V2 PSD response for Z-Axis excitation, -Z face sensor	144
Figure 7.7	LLNL V2 PSD response for Z-Axis excitation, +X face sensor ..	145

LIST OF TABLES

	Page
Table 2.1	Mission Specific LONESTAR Campaign Objectives 8
Table 3.1	Tool Maturity Level Assessment Guide 18
Table 5.1	STARE Payload Model Material Properties 50
Table 5.2	Exterior STARE Payload Material Properties 65
Table 5.3	STARE Payload Thermal Material Properties 66
Table 5.4	Itemized Spacecraft Heat Power Loads 67
Table 5.5	Simulation Shape Factors Used 71
Table 6.1	LLNL V2 Natural Frequency of First Five Modes 91
Table 6.2	LLNL V2 Probed Locations for X-Axis PSD Response 93
Table 6.3	LLNL V2 Probed Locations for Y-Axis PSD Response 97
Table 6.4	LLNL V2 Probed Locations for Z-Axis PSD Response 99
Table 6.5	LLNL V3 Natural Frequency of First Five Modes 100
Table 6.6	LLNL V3 Probed Locations for X-Axis PSD Response 103
Table 6.7	LLNL V3 Probed Locations for Y-Axis PSD Response 105
Table 6.8	LLNL V3 Probed Locations for Z-Axis PSD Response 105
Table 6.9	LLNL CI Transient Average Temperatures 108
Table 6.10	LLNL CI Steady State Temperatures 111
Table 6.11	LLNL CII Potential Strap Locations 116
Table 6.12	AGS4 Natural Frequency of First Five Modes 117

Table 6.13	AGS4 RMS Values for X-Axis Excitation	119
Table 6.14	AGS4 Probed Locations for X-Axis PSD Response	120
Table 6.15	AGS4 RMS Values for Y-Axis Excitation	122
Table 6.16	AGS4 Probed Locations for Y-Axis PSD Response	123
Table 6.17	AGS4 RMS Values for Z-Axis Excitation	125
Table 6.18	AGS4 Probed Locations for Z-Axis PSD Response	126
Table 6.19	AGS2 Natural Frequency of First Five Modes	128
Table 6.20	DragonSat Natural Frequency of First Five Modes	129

1. INTRODUCTION

Current trends in academic, government, and commercial satellite designs are moving towards smaller, less expensive integrated systems. This decrease in satellite size renders the requirement of large launch vehicles obsolete. Many smaller programs are beginning to take advantage of the resulting frequency increase of launch opportunities. As the aerospace industry transitions from a once highly compartmentalized entity into an era of higher exposure and increased accessibility, experimental payloads and student-designed satellites have seen tremendous growth. AggieSat Laboratory (AGSL), at Texas A&M University (TAMU), is one such example of a student organization thriving in the wake of a changing space industry.

Like many satellite designs, AGSL programs benefit from the technological advancements of computer aided design (CAD) software and integrated finite element analysis (FEA) solvers.¹ The use of such technology places AGSL at the center of a necessary discourse among industry and academia leaders regarding the role such computational solutions should play in the design process. Despite great efforts to establish clear validation and verification (V&V) standards² within the field of computational solid mechanics, little documentation regarding specific simulation packages is available to analysts. For this reason, FEA results are generally presented conjointly or supplementary to structural response predictions obtained through more conventional methods e.g., experimental testing.

1.1 Thesis Organization

This work utilized CAD generated simulation solutions as well as experimental test data to predict the structural responses of three different AGSL supported satellites. By examining both historical and current designs from the Low earth Orbiting Navigation Experiment for Spacecraft Testing Autonomous Rendezvous and docking (LONESTAR) and Space-based Telescopes for Actionable Refinement of Ephemeris (STARE) programs, the research presented here can be utilized to improve future design iterations. Additionally, the CAD tool utilized was qualitatively evaluated for AGSL simulation needs. As part of this evaluation, the Tool Maturity Level (TML) guide created by the United States Air Force Research Laboratory (AFRL) helped determine how best to utilize simulation data in the future. This assessment, having previously never been investigated within AGSL, provided essential internal insight as to the limitations of stand-alone CAD packages for satellite design and development. While the research presented within this document utilized SolidWorks and SolidWorks Simulation, the methods utilized in response prediction and TML evaluation are generally applicable to other CAD software as well.

Section 2 of this thesis briefly outlines the satellite programs through which this investigation was made possible as well as provides industry examples for which SolidWorks was used as an optimization tool. Section 3 highlights the motivation for this study from a V&V perspective and defines clear goals for the research. Next, Section 4 presents general governing equations for stress, strain, steady state conductive heat transfer, free vibration and forced vibration analyses.³⁻⁷ The text highlights how

CAD packages implement and solve, either iteratively or directly, the aforementioned systems of equations. Sources of uncertainty for both experimental and simulated data⁸⁻¹¹ were investigated and the corresponding impacts on result integrity weighed.

In an effort to consider the variability of experimental and simulation results, validation metrics^{12,13} for comparison of the two data types are defined in Section 5. Also outlined in Section 5, are the general techniques for utilizing FEA CAD packages to predict structural responses and how such steps were employed throughout this research. Additionally presented in Section 5 are simulation assumptions, geometric simplifications, material selections, mesh details, and boundary conditions for all three AGSL supported programs-six total CAD models.

In Section 6, the simulated and available experimental structural responses of the six models are summarized. Such simulated evaluations include: stress, deflection, acceleration, factor of safety (FS) and thermal output plots. Accelerometer readings from the experimental vibration tests of both AGS2 and the STARE payload are also captured. Within the text concerning simulation results is an overview of noteworthy model features, the material library utilized, and simplifying assumptions for each of the six models. Mesh convergence plots are shown as well to demonstrate the variability of non-converged solutions and the importance of mesh independent simulations.

As part of the final evaluation of the data, discrepancies between experimental and simulation results are discussed in Section 7.^{14,15} This final section also includes a recommendation¹⁶ for future uses of the CAD tool, as an independent design evaluation tool at AGSL. This suggestion will be based on the simulations' ability to meet

validation metrics and the standards established in the TML guide. Ultimately, this work adds to a limited literature archive of both satellite structural response predictions using CAD software and the usefulness of the TML guide in assessing application-specific software.¹⁷

2. BACKGROUND

2.1 Trends in the Aerospace Industry and Academia

In the past decade, nano-satellites (1-10kg) and micro-satellites (10-100kg) have made a drastic emergence in commercial, academic and military arenas. The size and cost of these compact spacecraft as well as the ability for many smaller payloads to ‘piggyback’ on large launch vehicles have contributed to an increase in launch frequency.^{18,19} Consequently, in an industry that was once exclusively controlled by government agencies such as the National Aeronautics and Space Administration (NASA) and the Department of Defense (DOD), there is now a spike in public launch opportunities through the government and private sector. One assessment suggests that civil users, classified largely as universities and research groups, are projected to increase the number of small satellites launches from a current annual average of 108 to almost 200 before 2015.²⁰ The impacts of this trend, while widespread, can easily be seen to include an increased rate of design, testing, and production.

As the space industry and academic worlds merge, a largely less-experienced faction of engineers is tasked with creating budget conscience, space rated systems on accelerated timelines. Furthermore, in order for these satellites to be successful in this changing market, designs will need to push the envelopes of size, weight, and power consumption.

2.2 Programmatic Background

Two examples of student-supported programs benefitting from small, space based research platforms are the LONESTAR and STARE campaigns under investigation at AGSL. AGSL, a student managed organization sponsored by the Aerospace Engineering Department at TAMU, was founded by Dr. Helen Reed in 2005. Still the principal investigator at the lab, Dr. Reed invests in programs that foster the goals of the lab, “to develop and demonstrate modern technologies by using a small-satellite platform, while educating students and enriching the undergraduate experience.”[†] Additionally, the lab fulfills analysis needs for a variety of third party programs. The myriad of opportunities at AGSL allows engineering fundamentals to be assessed both from a business and research perspective.

The design process within AGSL highlights the importance of a strict configuration management policy, similar to that practiced in industry. This policy allows students to track design deviations and test failures through well-documented procedures, development plans, and certification logs. Document control and configuration management, on this level, have contributed to launch manifests on manned vehicles and deployment opportunities from the International Space Station (ISS). In order to ensure these international resources are utilized to the fullest potential, the lab partners with industry and academic leaders to gain guidance and insight regarding the design, testing, manufacturing, integration, and operation of space-rated hardware.

[†] Reed, Helen, Dr. "AggieSat Lab - Home." 15 May 2013. <http://aggiesatweb.tamu.edu/>.

2.2.1 The Low Earth Orbiting Navigation Experiment for Spacecraft Testing

Autonomous Rendezvous and Docking Campaign

One such partnership is the LONESTAR campaign, which represents the largest student led enterprise at AGSL. Below is the agreed upon LONESTAR campaign statement.

“LONESTAR, Low earth Orbiting Navigation Experiment for Spacecraft Testing Autonomous Rendezvous and docking, is a programmatic partnership among the University of Texas at Austin (UT), Texas A&M University and NASA-JSC aimed at exploring and developing alternative Autonomous Rendezvous and Docking (ARD) systems for use on cost effective, low power microsatellite infrastructures. Over the course of four missions, the University of Texas at Austin and Texas A&M University will design and build four pairs of cooperative satellites to test and implement systems to ultimately demonstrate ARD on the fourth and final mission.”²¹

Leading up to the final mission and ultimate campaign goal of ARD, AGSL has clearly defined objectives for intermediate flights. These goals are briefly outlined in Table 2.1 and include a variety of hardware checkouts and evaluations, attitude control demonstrations, and visual confirmation capabilities. The technical objectives are further used to develop satellite and system requirements as well as mission success criteria for each flight.²¹

In addition to the below mission objectives all parties of the LONESTAR campaign are held to NASA and contractor safety standards.²²⁻²⁵ These standards dictate design constraints ranging from viable material selections to testing requirements. Furthermore, each university satellite is subjected to multiple, independent safety board reviews. NASA and third party entities oversee such reviews in order to verify structural integrity and ensure crew safety. It is therefore the exclusive responsibility of AGSL to

ensure satellite subsystems satisfy all mission success criteria. Internally, such assurance comes from a combination of simulations of the flight environment and hardware testing, on the component, subsystem, and integrated satellite level.

Table 2.1: Mission Specific LONESTAR Campaign Objectives²¹

-	Mission 2 Objectives
M2O-1	Evaluate sensors including but not limited to: Global Positioning System (GPS) receivers, Inertial Measurement Units (IMUs), rate gyroscope, accelerometers.
M2O-2	Evaluate Reaction Control System (RCS).
M2O-3	Evaluate Guidance Navigation and Control (GN&C) system including guidance algorithms, absolute navigation, and relative navigation.
M2O-4	Evaluate communications capabilities between two spacecraft and from each spacecraft to their ground stations.
M2O-5	Evaluate the capability to take video.

-	Mission 3 Objectives
M3O-1	Evaluate RCS.
M3O-2	Demonstrate ability to maintain relative velocity and attitude within TBD requirements.
M3O-3	Evaluate Autonomous Flight Manager (AFM).
M3O-4	Demonstrate docking system.

-	Mission 4 Objectives
M4O-1	Demonstrate full ARD capability using GN&C, RCS, and AFM.

Currently AGSL is working towards the second mission of the LONESTAR campaign, AggieSat4 (AGS4). AGS4 has a mass constraint of 50kg and will be limited in size by the ISS Japanese Experiment Module (JEM) airlock dimensions. AggieSat2 (AGS2) was the first AGSL LONESTARE satellite and launched in 2009 on Space Shuttle Endeavour, STS-127, for a 230 day mission.²⁶ AGS2 had a mass of approximately 2.3kg and was a 5x5x5in cube shaped satellite. The structural responses

of both satellites are investigated throughout this research and will be discussed further in subsequent sections.

2.2.2 The Space-based Telescopes for Actionable Refinement of Ephemeris Campaign

Another venture supported by AGSL is the Lawrence Livermore National Laboratory (LLNL) STARE Campaign. This project represents a five-program partnership among the Naval Postgraduate School (NPS), the National Reconnaissance Office, the Boeing Company, LLNL and TAMU. The goal of the campaign is to monitor space debris and predict collisions. In a March 2012 survey, conducted by the NASA Orbital Debris Program Office, the importance of such technology was clearly demonstrated on an international scale. NASA reported that, at the time of the update, there were 21,000 items larger than 10cm, 500,000 objects between 1-10cm and over 100 million objects smaller than 1cm in orbit around Earth.[†] Considering that these items travel with an average speed of 8km/s and that there are currently 560^{††} functioning satellites in space, the risk of collision is not only probable, it could be costly and catastrophic.

In order to develop a network of satellites capable of predicting collisions, the STARE campaign utilizes a specific class of satellites, known as CubeSats. Satellites classified as “1U” CubeSats generally fit in a 10x10x10cm volume and weigh less than

[†] NASA Orbital Debris Program Office. <http://orbitaldebris.jsc.nasa.gov/index.html>

^{††} Space Surveillance Network. <http://www.au.af.mil/au/awc/awcgate/usspc-fs/space.htm>

1kg. The size and weight of CubeSats make them cost effective to build and allow for more frequent launch opportunities. These satellites can also be ‘stacked’ to demonstrate higher complexity in a modular configuration. One common form factor is the 30x10x10cm or “3U” CubeSat. The STARE mission employs this 3U configuration, with 1U of the satellite dedicated to the payload, attitude control system and power system, respectively.

The STARE payload represents just one of several small satellite payloads which contributed to the Operationally Unique Technology Satellite (OUTSat) program. The OUTSat program was a collection of eleven CubeSats and eight Poly-Picosatellite Orbital Deployers (P-Pods) and included the STARE payload.[†] All eight P-Pods were located at a unique position, and thus launch environment, in an NPS designed launcher, the NPSCul. In order to support the needs of the STARE program, AGSL performs structural and thermal analyses for improved design and system characterization. The results of these studies are presented as part of this work and will be discussed in greater detail in a later section.

2.3 Computer Aided Design Packages

As is the case in most technical design fields, satellite programs almost exclusively utilize CAD to draft and validate proposed solutions. Such software with

[†] “CubeSat.org”. June 20, 2013. <http://www.cubesat.org/index.php/missions/upcoming-launches/122-136-launch-aler>

built in FEA solvers, i.e. CATIA[†], SolidWorks^{††}, and Inventor^{†††}, afford users the opportunity to create one-to-one digital models of designs while vetting manufacturing, integration, and integrity concerns. These CAD packages also allow designs to be virtually tested under operational static, frequency, and thermal loads. The cost benefit of virtual testing for realistic environments has proven to be quite impressive for large-scale projects.^{27,28} Furthermore, independent analysis of CAD usage in industry shows companies using CAD software achieve, “revenue, cost, launch date, and quality targets for 86% or more of their products.”²⁹

Engineers today benefit from countless commercial CAD packages. Of these options, the majority offers integrated FEA solvers for performing complex structural analyses. While this arsenal seems abundant, factors such as: supported import/export file formats, platform compatibility, technical support, and cost all impact and limit the viable options available for any given application. For the purposes of this research, SolidWorks 2011 Professional was utilized.

Many, if not most, CAD packages feature built-in FEA solvers, which aim to create seamless transitions between design and design validation. Within CAD simulation suites, designers have the option of conducting linear static, frequency, buckling, thermal, drop test, fatigue, forced vibration and non-linear dynamic

[†] "Login to 3DEXPERIENCE Platform." *3DEXperience Platform*. <http://www.3ds.com/products/catia/>

^{††} "SolidWorks Simulation Premium." *3D CAD Design Software SolidWorks*. <http://www.solidworks.com>

^{†††} "Software for Mechanical Design and Simulation." *Inventor and Inventor Professional*. <http://www.autodesk.com/products/autodesk-inventor-family/overview>

simulations, to name a few. Most commercially available CAD software accept many import formats e.g., DXF, DWG, Parasolid, IGES, STEP, ACIS, STL, ProE, and Solid Edge, which allow for ease of file sharing as well as data encryption. Likewise, information can be exported in a variety of formats ensuring safe and efficient result archives. Such features made commercially available CAD software a suitable choice for the research presented.

Additionally, the CAD tool utilized in this research offers a Hardware Benchmark to ensure system compatibility. The benchmark measures central processing power, graphics card, and input/output performance by averaging the times of five performance tests. Each test cycles through a part rebuild, rotate/zoom, render, close, a drawing open, pan/zoom, add sheet, close, and an assembly open, rotate/zoom, and close. The SolidWorks Hardware Benchmark was run on the machine used in this research and provides confidence that variances between simulation run times, discussed later, were minimally impacted by hardware performance. Computer specifications and benchmark results can be found in the Appendix.

2.3.1 SolidWorks in Other Applications

The SolidWorks Simulation package has been used for similar research in a variety of different applications. The information and research summarized below is not meant as an exhaustive literary review. Rather, the examples provided are intended to establish merit for the simulation tool and to highlight current uses of SolidWorks in a variety of industries.

In the automotive industry for example, SolidWorks Simulation was utilized to analyze and optimize drums of tire testing machines.³⁰ In such machines, drums are utilized to simulate road interfaces for the purposes of endurance, speed, and material tests. Bu's research aimed at optimizing the mass of a 5m drum, for testing large engineering grade tires. Specifically, the investigation utilized stress, displacement and geometric measurements from SolidWorks as inputs for constraint variables in an optimization function. Ultimately, Bu concluded that utilization of SolidWorks in the design process contributed to budget, schedule and optimization success.

Another application where the benefits of SolidWorks can be seen in product design is the oil and gas industry.³¹ Feiyu and Qingyan of the College of Construction at Jilin University in China demonstrate SolidWorks' usefulness as a comparison tool. The research investigates two topdrive stems, used to provide rotational force on drilling rigs, and compares simplified models of each. Final assessments of each topdrive stem's stress and fatigue are achieved with Simulation.

An additional industry that benefitted from SolidWorks Simulation analyses was pharmaceutical drug production.³² In the research conducted at Tianjin University of Science, solid-state fermentation equipment was optimized using SolidWorks. This body of work utilized FEA to make parametric studies of shaft dimensions and material selections. Due to the fact that virtual assemblies were used in the optimization process rather than prototype testing, production costs were significantly reduced. Furthermore, SolidWorks COSMOSMotion plug-in was used to further optimize the drum design and verify that fermentation could be achieved for the specified operating conditions.

In addition to the structural analyses presented, SolidWorks has proven to be extremely useful in conducting thermal investigations. In 2012, research was presented showing the benefits of SolidWorks Simulation in modeling the steady-state behavior of support equipment, internal to steel working ovens.³³ The study considered the steady state results of both ANSYS Workbench and SolidWorks Simulation for an infrared temperature measurement installation support. While the two simulations' results differed by only 0.5°C, Mr. Ying Peng concluded that ANSYS Workbench was the better solution for solving multiphysics simulations, i.e. problems coupling FEA with molecular phenomenon.

3. MOTIVATION

Throughout the literary research for this study, a deficiency in the applications for which Simulation has been utilized became apparent. Few, if any, examples exist of the package being used to evaluate small satellites. Rectifying this gap in the literature is one fundamental goal of the research. The analyses of the STARE, AGS2, and AGS4 systems will serve as three independent examples of how CAD software can be employed in predicting the structural responses of small satellites.

Another area of insufficient data exists surrounding the validity of simulation results. To truly understand how this deficit impacts current and future work in the aerospace industry, the following sub-section investigates the difference between software validation and verification and how a failure to address either can adversely impact designs. This discussion serves as additional motivation towards another primary objective of this work, to assess the ability of CAD software to produce stand-alone structural response predictions. The evaluation of the software's limitations adds to a sparse database currently available for CAD users and product designers.

In order to complete a review of the simulation tools and to present results in a concise and meaningful manner, this work will look at employing proposed verification and validation guides. Such standards have been developed by professional associations³⁴ as well as government funded research organizations and provide a common language with which to discuss results. For this reason, a tertiary objective of

this research is the adherence to standard definitions and success metrics in the evaluations of both the simulated and experimental results.

3.1 Validation and Verification of Simulation Results

In order to achieve the last of the above research objectives, an important distinction must be made between software validation and verification. While varying definitions for each are presented in the literature, the majority differs only in semantics. Throughout this research the distinction between the two will be as follows:

- *Validation-Identification of correct mathematical model to physically represent the system in questions*³⁵
- *Verification- Assurance that computational model and its algorithms accurately solve the mathematical model*³⁵

Both validation and verification represent important steps in obtaining accurate simulation results. In a paper on simulation governance the author, Barna Szabo, suggests that a large majority of the engineering community both recognize the need for and would benefit from V&V procedures. Two key obstacles, which restrict implementation of such procedures, Szabo states, are a general frustration among users and developers over the veracity of results and a lack of V&V support within existing software.

Furthermore, the question of accountability must be addressed. Using the above definitions for V&V one could argue that a natural delineation of responsibility exists between vendor and analyst. While this may be the case, unless standards are put into

place and upheld with consistency in industry, the burden to validate results and verify code will continue to fall on those who rely on CAD accuracy. This long-standing habit will only serve to further the notion that CAD results cannot serve, independently, as sufficient commentary on design integrity.

3.2 Tool Maturity Level Evaluation

In an effort to rectify the inconsistencies of software evaluations and elevate computational packages beyond the supporting role most currently play in design, the United States AFRL sponsored a Technical Interchange Meeting (TIM) in February of 2011. The results of this meeting, while aimed at V&V within integrated computational materials engineering, have numerous crossovers to the processes utilized in computational solid mechanics. Perhaps the most beneficial outcome of this TIM was the TML assessment guide.³⁶

“The TML descriptions are intended to be general in nature and broadly applicable... [They] convey increasing fidelity, supporting data, documentation, level of V&V, and hence confidence in the decisions or results- with increasing tool maturity.”³⁶ Each of the five levels of the TML guide assess categories of model basis and definition, complexity and documentation, supporting data, model verification, rules of applicability, uncertainty quantification, and validation. Table 3.1, on the next page, highlights the developmental level of each category for a given TML classification.

Table 3.1: Tool Maturity Level Assessment Guide ^{Modified from 36}

Assesment Category Tool Maturity Level	<i>Model Basis and Definition</i>	<i>Complexity and Documentation</i>	<i>Supporting Data</i>	<i>Model Verification</i>	<i>Range of Applicability and Uncertainty Quantification</i>	<i>Validation</i>
TML 1	*Model defined *Inputs/Outputs defined *Application defined	*Process has been mapped through flow diagram	*Supporting data identified	*Code and model verification plan developed	*Uncertainty quantification (UQ) and verification plan developed	
TML 2	*Models and sub-models defined *I/O defined for sub-model *I/O ranges defined	*Dependence on sequential or interdependent computations defined *User guide conceptualized	*Adequate supporting data available, documented and archived	*Computer code verified *Model computations verified against supporting data	*Range of applicability and input parameters defined *UQ sensitivity analysis performed *Demonstrate trends consistent with known results	*Validation plan developed *Initial Risk-Consequence assessment completed
TML 3		*Dependence on inputs from other analytical tools defined *User guide developed and documented	*Supporting data represents full range of application	*Model computations verified over range of use *Version control documented and implemented	*Model output exercised and assessed over full range of applicability *Limitations imbedded to control use beyond range	*Sub-models validated *Selected validation cases completed *Risk-Consequences assessed for application
TML 4		*User guide references supporting data, UQ analysis, and validation cases	*Supporting data adequate to determine accuracy and validation of model	*Code and model verification complete per ASME V&V Guide	*UQ analysis performed for model output	*Model validation over range of interest *Model accuracy validated
TML 5					*Benchmark cases including UQ established *Model performance validated equivalent or better than experimental capacity	*Model uncertainty validated *Benchmark validation cases established

At the conclusion of this work, the table above will be utilized as the primary assessment measure for CAD software as analytical tools in small satellite development. A TML-1 verdict will be given for an analytical tool with unverified potential. If the CAD tool receives a TML-1 rating for the analysis of satellites in the capacity of this research, the recommendation for future use will be limited to investigative explorations. The results of a TML-1 tool would not be considered adequate to limit or impact previously accepted physical qualification tests. A TML-2 tool is capable of predicting performance trends and relative results. As with the prior level, outputs of TML-2 software should not decrease either the intensity or quantity of physical tests but could be used to plan appropriate analytical assessments. TML-3 software would produce findings with fidelity appropriate for lessening testing requirements and evaluating alternatives to industry standard processes. Results of a TML-3 package would lack the complete validation required for a TML-4 ranking. Software that falls under the TML-4 heading would be considered fully vetted and validated for the stated application. Uncertainty within the model will have been quantified and the impact on results characterized. Lastly, a TML-5 score would produce results, which consistently achieved higher accuracy than experimental testing. TML-5 tools would be the only software capable of stand-alone results and complete V&V confidence. A complete user guide comprised of supporting documentation and V&V activities would support the recommendation for use of TML-5 results in lieu of physical testing.

Ultimately, the TML determined appropriate for the use of CAD at AGSL will dictate how an analyst will use this software package in the future. The level determined

appropriate for the results presented will allow designers to use the iterative FEA processes, integrated within CAD software, to more efficiently turn around designs. While the final assessment will not impact NASA safety standards and/or any related physical testing practices, it is the goal of this research to define the level of confidence appropriate for subsequent projects.

3.3 Objectives

This work aims to contribute to an admittedly limited body of literature concerning structural response predictions of small satellites using CAD packages, specifically, SolidWorks Simulation. Also, efforts will be made so that comparisons of future simulations and observed physical behavior might be possible. Specifically, validation metrics for the LLNL-STARE program and LONESTAR-AGS2 and AGS4 missions will be presented as specific examples by which to evaluate simulation performance. The end goal of the proposed research will be predictions of all three satellites' structural responses based on simulation and experimental data as well as an assessment of predicted responses in both test and launch environments.

4. METHODOLOGY

This section investigates the governing systems of equations for the analyses utilized throughout this research as well as the available solvers for completing FEA problems within CAD packages. Also discussed, are the processes within modeling where uncertainties and solution errors can occur. These errors as well as the errors associated with experimental testing are outlined later in this section to facilitate the discussion of results in Section 7.

4.1 Governing Equations

4.1.1 Strain-Stress Relationship

Consider an infinitesimal material element anchored at one corner to the Cartesian coordinate system. If the material element were subjected to a load or temperature distribution, strain or deformation would occur. Strain is defined as the ratio between changes in an object's form, due to externally applied loads, and the object's original dimensions. The resulting element shape could be expressed in a matrix equation using Eq. (4.1).

$$\boldsymbol{\varepsilon} = \begin{bmatrix} \boldsymbol{\varepsilon}_{xx} & \boldsymbol{\varepsilon}_{xy} & \boldsymbol{\varepsilon}_{xz} \\ \boldsymbol{\varepsilon}_{yx} & \boldsymbol{\varepsilon}_{yy} & \boldsymbol{\varepsilon}_{yz} \\ \boldsymbol{\varepsilon}_{zx} & \boldsymbol{\varepsilon}_{zy} & \boldsymbol{\varepsilon}_{zz} \end{bmatrix} = \begin{bmatrix} \frac{\partial u}{\partial x} & \frac{\partial u}{\partial y} + \frac{\partial v}{\partial x} & \frac{\partial w}{\partial x} + \frac{\partial u}{\partial z} \\ \frac{\partial u}{\partial y} + \frac{\partial v}{\partial x} & \frac{\partial v}{\partial y} & \frac{\partial v}{\partial z} + \frac{\partial w}{\partial y} \\ \frac{\partial w}{\partial x} + \frac{\partial u}{\partial z} & \frac{\partial v}{\partial z} + \frac{\partial w}{\partial y} & \frac{\partial w}{\partial z} \end{bmatrix} \quad (4.1)$$

Where u , v , and w represent the deformations of the element in the x , y , and z -axes, respectively. This matrix is clearly symmetric and therefore only has six, rather than nine, independent terms. Furthermore, the off diagonal terms are known as shear strain while the diagonal elements are normal strain values. Hooke's Law, for linearly elastic isotropic material, suggests there is a linear relationship between normal stresses (σ) and normal strain (ϵ) as shown in Eqs. (4.2-4.4).³

$$\epsilon_{xx} = \epsilon_x = \frac{1}{E}(\sigma_x - \nu(\sigma_y + \sigma_z)) \quad (4.2)$$

$$\epsilon_{yy} = \epsilon_y = \frac{1}{E}(\sigma_y - \nu(\sigma_x + \sigma_z)) \quad (4.3)$$

$$\epsilon_{zz} = \epsilon_z = \frac{1}{E}(\sigma_z - \nu(\sigma_x + \sigma_y)) \quad (4.4)$$

Likewise, the shear stress (γ) can be related to shear strain by the following three equations.

$$\gamma_{xy} = \frac{2\sigma_{xy}(1+\nu)}{E} = \epsilon_{xy} \quad (4.5)$$

$$\gamma_{yz} = \frac{2\sigma_{yz}(1+\nu)}{E} = \epsilon_{yz} \quad (4.6)$$

$$\gamma_{zx} = \frac{2\sigma_{zx}(1+\nu)}{E} = \epsilon_{zx} \quad (4.7)$$

In the above equations, E is Young's modulus (Pa) and ν is Poisson's ratio.

These relationships can be written in a more simplified matrix form as follows.

$$\epsilon = A\sigma \quad (4.8)$$

Where in Eq. (4.8) $\epsilon = [\epsilon_x \ \epsilon_y \ \epsilon_z \ \epsilon_{xy} \ \epsilon_{yz} \ \epsilon_{zx}]^T$, $\sigma = [\sigma_x \ \sigma_y \ \sigma_z \ \sigma_{xy} \ \sigma_{yz} \ \sigma_{zx}]^T$, T is the transposed matrix and A is a 6 by 6 matrix of the following form, Eq. (4.9).

$$A = \frac{1}{E} \begin{bmatrix} 1 & -\nu & -\nu & 0 & 0 & 0 \\ -\nu & 1 & -\nu & 0 & 0 & 0 \\ -\nu & -\nu & 1 & 0 & 0 & 0 \\ 0 & 0 & 0 & 2(1+\nu) & 0 & 0 \\ 0 & 0 & 0 & 0 & 2(1+\nu) & 0 \\ 0 & 0 & 0 & 0 & 0 & 2(1+\nu) \end{bmatrix} \quad (4.9)$$

Using the above relationships and the principle of virtual work, the finite element method can be derived. The principle of virtual work states that if a system in equilibrium, while under various external forces, is virtually displaced, the virtual work of the external loads is zero. It follows then that the static state equilibrium displacement field is that which both satisfies boundary conditions and minimizes the system's total potential energy.⁵ In order to derive the stress at any point of an FEA model consider the following definitions (simplified for purely translational responses):

$$u = \{u, v, w\} \quad (4.10)$$

$$q = \{q_i\} (i=1, 2, \dots, n) \quad (4.11)$$

$$q_i = \{q_{x_i}, q_{y_i}, q_{z_i}\} \quad (4.12)$$

where u is a vector of generic, non-nodal, translational displacements (m) in the three primary axes of the model. Translational nodal displacements, on the other hand, are denoted for each node by q_i and the total displacement (m) vector for the system is expressed as q . Generic and nodal displacements can be related by Eq. (4.13). Below, the rectangular matrix f contains expressions which make u dependent on q and are known as displacement shape factors. Displacement shape factors vary based on element dimensionality and boundary conditions.

$$u = fq \tag{4.13}$$

Next, consider the following strain-displacement relationship, alluded to in Eq. (4.14).

$$\varepsilon = du \tag{4.14}$$

In Eq. (4.14) d is a matrix of linear differential operators.

$$d = \begin{bmatrix} \frac{\partial}{\partial x} & 0 & 0 \\ 0 & \frac{\partial}{\partial y} & 0 \\ 0 & 0 & \frac{\partial}{\partial z} \\ \frac{\partial}{\partial y} & \frac{\partial}{\partial x} & 0 \\ 0 & \frac{\partial}{\partial z} & \frac{\partial}{\partial y} \\ \frac{\partial}{\partial z} & 0 & \frac{\partial}{\partial x} \end{bmatrix} \tag{4.15}$$

Combining Eq. (4.13) and Eq. (4.14) yields Eq. (4.16). Below, the matrix product of d and f gives generic strain values. Furthermore, this result can be applied to the inverse relationship of Eq. (4.8) to yield the following relationship for model stress.³

$$\sigma = A^{-1}dfq \tag{4.16}$$

The relationships expressed above are then utilized in FEA solvers to calculate stress gradients over the entirety of a geometric entity.

4.1.2 Free and Forced Vibration

Free vibration analyses are used to describe the natural frequency modes of a system. These natural frequencies are the resonating rates at which the structural dynamics of a system are most responsive. In satellite design specifically, these frequencies play a large role in evaluating hardware. Namely, it is important to stiffen structures beyond the known frequency peaks of the launch vehicle in order to avoid

dangerous coupling. To investigate such vehicle payload interactions completely, forced vibration is utilized to simulate structural responses under known loads.

To better understand FEA vibration analyses, consider the following system where k is a spring constant, c is a viscous damping coefficient and $x(t)$ is the displacement (m) of mass (kg), m , with time.

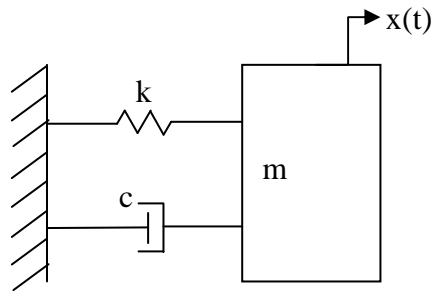


Figure 4.1. Spring/damper system

When the above system, Fig. 4.1, is allowed to freely vibrate, without damping or external forces, the following ordinary differential equation (ODE), Eq. (4.17), describes the mass's motion. By use of the quadratic formula, the roots of this ODE and thus the natural frequency of the system are easily obtained.⁸

$$m \ddot{x} + kx = 0 \tag{4.17}$$

The simplification of no damping is unrealistic for physical systems and causes natural frequencies computed in this fashion to be slightly too high. Moreover, if the system being analyzed is expanded from a single degree of freedom (DOF), presented above, to a higher DOF system, the following equation is utilized.

$$M \ddot{x} + C \dot{x} + Kx = F \tag{4.18}$$

Above, the x and F are displacement (m) and external force vectors (N), respectively. The variables M , C , and K , represent square mass (m), damping (kg/s), and stiffness matrices (N/m). Again, free vibration simulations utilized the $F=\bar{0}$ and $C=\bar{0}$ assumptions while forced vibration systems have prescribed loading, $F=f(t)$.

4.1.3 Steady State and Transient Heat Transfer

Of the three main forms of heat transfer, only two forms are applicable to space applications: conduction and radiation. Between these two types of heat transfer, a satellite's complete thermal profile can be defined. Fourier's law governs conduction, heat transfer through solid objects, and can be expressed in the following form.

$$q'' = -k\nabla T \quad (4.19)$$

In the above equation, k is the material's thermal conductivity (W/m*K), ∇ is the del operator, T is the scalar temperature field (°K), and q'' is the heat flux (W/m²).

Equation (4.19) can be applied along with an energy balance equation for an infinitely small control volume to obtain the equation for heat diffusion in the Cartesian coordinate system³⁷, Eq. (4.20). Below, \dot{q} is the rate of thermal energy generation per unit volume (W/m³), α is the thermal diffusivity (m²/s), and t is time (s).

$$\frac{\partial^2 T}{\partial x^2} + \frac{\partial^2 T}{\partial y^2} + \frac{\partial^2 T}{\partial z^2} + \frac{\dot{q}}{k} = \frac{1}{\alpha} \frac{\partial T}{\partial t} \quad (4.20)$$

The heat diffusion equation can be simplified for a variety of different situations. For example, in a powered-off satellite, thermal energy generation is generally

negligible. Likewise, orbits where the satellite experiences continually thermal inputs from the Sun and our Earth, the system is considered steady state and the right side of the equation is neglected. In the research presented here, one-dimensional heat transfer is utilized in the design of a thermal strap system. This assumption reduces the diffusion equation to the form shown in Eq. (4.21).

$$\frac{d}{dx} \left(k \frac{dT}{dx} \right) = 0 \quad (4.21)$$

Radiation, in contrast to conduction, does not require matter in order to transfer heat. Radiation is the direct effect of the oscillatory movement of electrons caused by an objects finite, internal temperature. These electron transitions are sustained by temperature and are emitted by all mater. Once the radiation reaches another body, three processes, absorption, reflection and transmission, play an important role in the resulting heat transfer. The following equation, known as the Stefan-Boltzmann Law, describes heat transfer from a blackbody, i.e. reflectivity=absorptivity=1.

$$q = \sigma T^4 A \quad (4.22)$$

Above, σ is the Stefan-Boltzmann constant ($5.6703 \times 10^{-8} \text{ W/m}^2 \cdot \text{K}^4$) and A is the area (m^2). This equation can be modified to describe heat transfer from a grey body with the inclusion of ϵ , which is the emissivity of a body. Emissivity is discussed further in Section 5. When radiation is considered for two or more objects, geometrical constraints are utilized to find view, or shape, factors. These shape factors, F , quantify the amount of departing energy incident on a secondary body. In such instances, where more than two bodies form an enclosure, the net radiation exchange is described by Eq. (4.23).³⁷

$$q_{12} = \frac{\sigma(T_1^4 - T_2^4)}{\frac{1 - \varepsilon_1}{\varepsilon_1 A_1} + \frac{1}{A_1 F_{12}} + \frac{1 - \varepsilon_2}{\varepsilon_2 A_2}} \quad (4.23)$$

4.2 Mesh Generation

The fundamental concept behind FEA in engineering applications is the notion that complex geometric entities can be subdivided into N finite regions (or elements), allowing the system's governing equations to be expressed as a set of N matrix equations. In practice, this subdivision of the space domain is called meshing and it plays a vital role in solution accuracy.

A mesh is a grid-like network spread over the geometric entity under investigation, in three-dimensional space. This grid is comprised of elements with finite sizes and points of intersection called nodes. Nodes can also exist on midpoints, or at equal spacing along the lengths, of an elemental unit. As shown in Fig. 4.2, elements can take a variety of shapes and sizes, resulting in a variety of nodal configurations. Both the sizes of elements and the number of nodes per element impact the accuracy of a simulation.





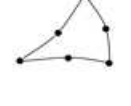
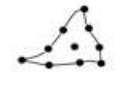
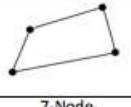
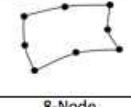
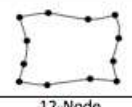
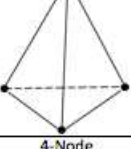
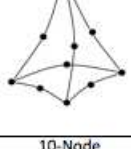
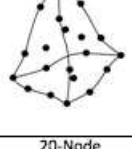
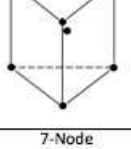
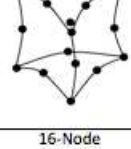
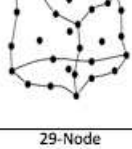
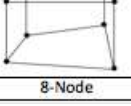
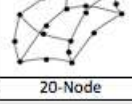
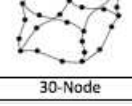
	Linear	Quadratic	Cubic	
				1-D Elements
	2-Node	3-Node	4-Node	
Triangular Elements				2-D Elements
Quadrilateral Elements				
	3-Node	6-Node	10-Node	
Tetrahedral Elements				3-D Elements
Prism Elements				
Hexahedral Elements				
	4-Node	10-Node	20-Node	
	7-Node	16-Node	29-Node	
	8-Node	20-Node	30-Node	

Figure 4.2. Elemental mesh types Modified from 38

The relationship between mesh quality and result accuracy arises from the basic principles of FEA. At its foundation there exists the notion that, rather than solving equilibrium state equations directly, integral forms of these equations can be solved for finite elements. To achieve this goal, FEA solvers transform the governing system of equations into integral equations and construct a matrix of such equations to be solved with boundary conditions at the nodal locations. The solution must then be interpolated from node locations over the area of the element. Limiting the area within an element

over which the solution must be interpolated increases the overall accuracy of the solution gradient for the domain.

Furthermore, the precision of an interpolated solution is based on an element's spatial approximation. Such approximations are based on node driven polynomials, where the number of elemental nodes can be related to the number of polynomial coefficients. Example polynomial interpolation equations are expressed below for two elemental types: linear and quadratic.⁵ These are the two classifications of elemental shapes utilized in the CAD tool for this research. Linear elements were used for initial investigations and called 'Draft Mesh' elements in the CAD software whereas all subsequent convergence data and results were obtained with 'Quality Mesh' quadratic elements.

$$T(x) = c_1 + c_2x \quad (4.24)$$

$$T(x, y) = c_1 + c_2x + c_3y \quad (4.25)$$

$$T(x, y, z) = c_1 + c_2x + c_3y + c_4z \quad (4.26)$$

$$T(x) = c_1 + c_2x + c_3x^2 \quad (4.27)$$

$$T(x, y) = c_1 + c_2x + c_3y + c_4x^2 + c_5xy + c_6y^2 \quad (4.28)$$

$$T(x, y, z) = c_1 + c_2x + c_3y + c_4z + c_5x^2 + c_6xy + c_7y^2 + c_8xz + c_9yz + c_{10}z^2 \quad (4.29)$$

Above $T(x)$, $T(x, y)$ and $T(x, y, z)$ are values to be interpolated in 1D, 2D, and 3D, respectively. The variables x, y , and z are the local element coordinates. Equations (4.24-4.26) are expressions for the spatial approximation of linear 1D, 2D (3-Node), and 3D (4-Node) elements. Conversely, Eqs. (4.27-4.29) are the spatial approximation for

quadratic 1D, 2D (6-Node), and 3D (10-Node) elements, respectively. Due to the semiautomatic mesh generation interface of the utilized CAD software, this research only utilized the following element types: 2D triangular quadratic, 3D tetrahedral linear, and 3D tetrahedral quadratic elements.

Spatial approximations in the form of the above polynomials highlight how elemental shapes also impact geometric errors in an FEA model. For example, curved surfaces that are approximated by linear elements will have increasingly inaccurate solutions as the distance between the nearest node and point of interest is increased. Conversely, polynomial interpolation ‘wiggle’ errors can cause inaccuracies in interpolated solutions for higher order polynomials. Solution accuracy can be improved by raising the nodal dimensionality, but there is a trade-off between simulation run time and result resolution. This design exchange should also be considered when investigating the benefits of decreased element size, as a similar trend is observed for increased mesh density and simulation run times, Fig. 4.3.

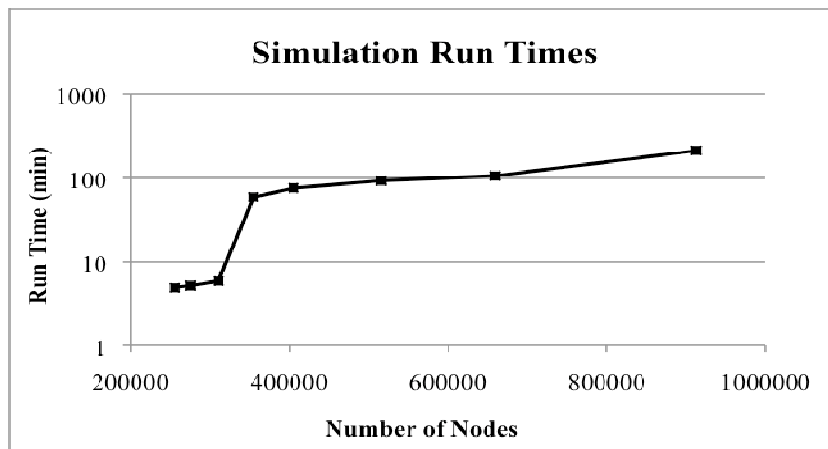


Figure 4.3. Run time trend for increased node counts

The figure above shows sample data for various mesh sizes from an early iteration of the AGS4 model. The large increase in simulation time after 300K nodes is undoubtedly misleading in illustrating this point. This clear jump was a result of achieving solution convergence, rather than the previously discussed relationship between mesh size and run time. After 350K nodes however, the solution converged and the trend continued to gradually increase over the remainder of the data set. The acceptance or rejection of variance between mesh sizes should be clearly defined by a program's validation metrics. Examples of such standards are discussed at length throughout this section. For this and all subsequent figures, data points were linearly connected with simple, straight lines. No information on point-to-point trend lines should be inferred from such representations.

4.3 Finite Element Analysis Solvers

The following sections highlight the major differences between direct and iterative solvers and discuss the options available with the utilized CAD package. As the name suggests, iterative solvers make initial guesses for solutions and then calculate the error associated with the assumed solution. All subsequent guesses are made in an effort to minimize errors and iterations continue until the overall error drops below a user specified threshold. Direct solvers on the other hand, solve the system of governing equations for each node simultaneously. Each method has relative benefits and pitfalls, both of which are discussed below.

4.3.1 Direct Methods

Perhaps the largest draw to using a direct solver method for moderately sized systems is the reduction in computation errors. This increased accuracy is achieved by the solver's use of numerical techniques to solve high order systems of equations. Such techniques e.g., Gauss-Jordan elimination, lower triangular and upper triangular (LU) decomposition, and general inverse matrix multiplication, require that the system's governing equations be made into a set of matrix equations.

In general, matrix inversion is frequently utilized to directly solve a system of equations. In matrix inversion, the inverse of a system's governing equation matrix is found by employing one, or several, row reduction techniques. Gauss-Jordan elimination, for example, utilizes matrix row manipulations to reduce the left hand side of the original set of system equations into the identity matrix, I . Through the use of row addition, row multiplication with a scalar, and row placement interchange, the Gauss-Jordan elimination technique simultaneously forms the solution matrix on the right hand side of the equation. LU decomposition, similarly, is the process through which a square matrix is decomposed into the product of a lower triangular and upper triangle matrix. Once the inverse matrix is found, multiplication is used to compute the system's solutions. As can be expected, an increase in the size of the system's matrix causes the solution times for such methods to grow exponentially. Additionally, the computational cost of solving high order FEA problems with direct methods is emphasized in the amount of random access memory required to carry out the calculations.

Within SolidWorks, the direct method utilized is known as the Direct Sparse solver. SolidWorks[†] suggests that the use of Direct Sparse be limited to problems where the number of DOFs is less than 100K due to the computational complexity of inverting large stiffness matrices. For this reason, the Direct Sparse solver was only utilized to investigate studies where unexpected model behavior was encountered.

4.3.2 Iterative Methods

Iterative solvers use guess and check methods in acquiring a system's solution. After each solution attempt, the iterative solver computes the solution difference between the current and previous step to determine if the solution process is convergent or divergent. Convergent solutions are stored and iteration on the solution parameters continues until accuracy within a specified tolerance is achieved. Perhaps the most notable benefits of iterative solvers, in comparison to the direct methods discussed above, is a decrease in computing time and higher accuracy for large systems. In the SolidWorks Simulation package, the iterative solver is the FFEPlus solver. In the interest of simulation run time and due to the high mesh densities generated for the research, the SolidWorks' FFEPlus solver was utilized exclusively throughout this work.

4.4 Simulated Loading

Another important factor to consider when discussing simulation accuracy are the loads applied within the CAD software. Depending on the study under investigation,

[†] SolidWorks Help. <http://help.solidworks.com/>

loads can vary from static forces, to pressure distributions, sinusoidal or random excitations, thermal environments, power sinks/sources, or torques, to name a few. Each of these load types plays an important role in creating realistic simulation environments. Additionally, because loads can be applied at specified physical interfaces, reaction forces can be utilized to simplify modeling. For example, power sources can replace geometrically cumbersome components in thermal simulations while base excitations can replace shaker tables, interface plates, and motors.

For this research, random vibration, uniform base excitations were utilized extensively. Base excitations are defined by curves known as power spectral density (PSD) or acceleration spectral density (ASD) inputs and are uniformly applied, within the CAD software, to all restrained features. Random PSD or ASD curves, as the names might suggest, define varying acceleration per frequency profile. Integration of the area under these curves yields the root mean squared (RMS) g-loading experienced by the integrated system. PSD and ASD profiles can be scaled to emulate a variety of launch and/or test scenarios. Many test plans, for example, specify 3dB (or double power) ASD curves to capture responses higher than those elicited by launch environments.

Throughout this research several different test levels were utilized. All test environments were considered the ‘worst case’ loading for a given payload. In some cases, programmatic diction specified ‘qualification’ test levels while others referenced ‘proto-qualification or proto-qual’ vibrations levels. From a simulation perspective, such nomenclature did not impact the FEA processes or how the results were interpreted. Rather, the naming discrepancy was solely utilized to indicate a particular payload’s

testing and flight history. In general, qualification test levels are more rigorous than proto-qual test levels and are utilized earlier in a payloads development to demonstrate design robustness. Proto-qual levels, on the other hand, are utilized to show manufacturing adherence of design specifications or when test units are expected to be repurposed for flight. Both qualification and proto-qual test levels are generally higher than acceptance testing levels which are meant only to highlight workmanship defects at the system integration level.[†]

4.5 General Processes for Finite Element Analysis

In addition to the mesh generation, model loading, and solver options discussed above, there are several other steps that must be completed in order to achieve reasonable results from CAD-based FEA solvers. Figure 4.4 highlights, in addition to meshing, the critical steps utilized for predicting the structural responses of the three satellites investigated throughout this research. While the research presented in this paper employed SolidWorks Simulation, the steps presented below are considered universal practices and can be applied to any FEA software.

[†] The Aerospace Corporation. “Test Requirements for Launch, Upper-Stage, and Space Vehicles.” https://aeroweb.aero.org/m_dir/maddl.nsf/

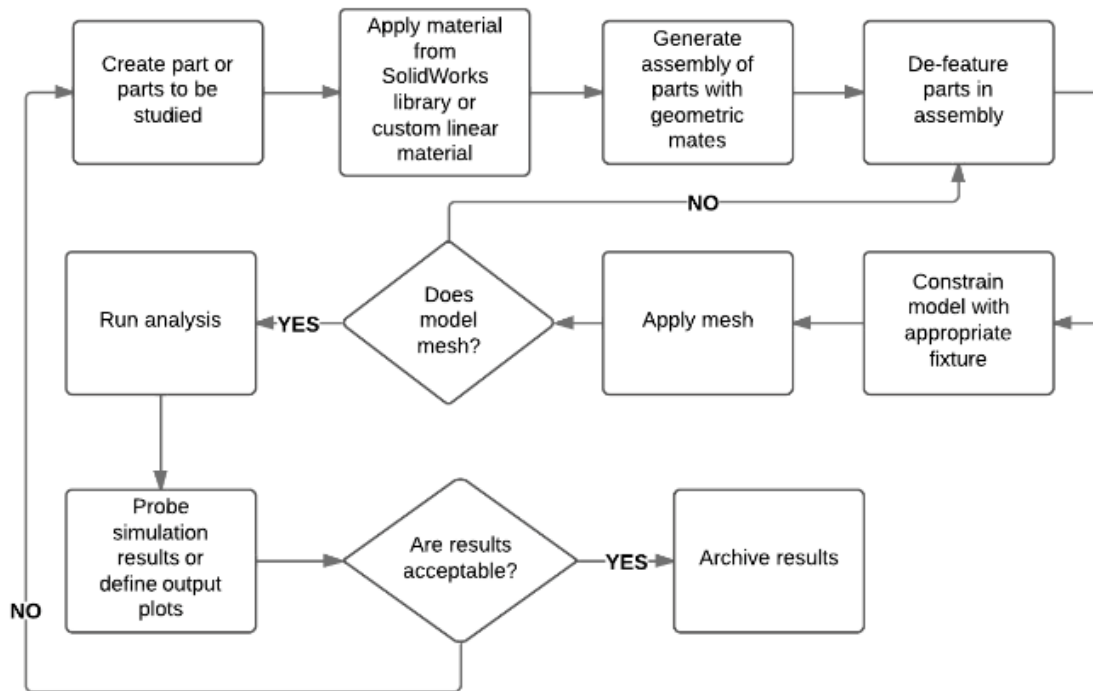


Figure 4.4. Progression of steps taken in SolidWorks from component design and modeling to analysis Generated from 5

4.5.1 Iterative Simulation Practices

When used correctly, the steps outlined above should be iterative and save both computational and financial resources. For example, performing structural analyses on individual parts prior to creating assembly level models can highlight problematic geometries, either from a mesh generation or stress concentration perspective. Mesh generation failures can almost always be traced to geometric complexities in the model. Fillets with tight radii, features with thickness less than the maximum element size and threading lined mounting holes are all examples of potential mesh complications. Component level analysis can also justify decisions made during the de-featuresing process, as holes and cutouts in low stress regions can justifiably be removed for

assembly integration. In situations where a component's geometric complexities are integral design features and cannot be suppressed, mesh controls become essential. Within the CAD software, a mesh control is a standalone grid system which when applied to a specific part or subset of parts is evaluated independently from the assembly level solution. Components specific controls can yield unrealistic results at grid interfaces however due to mesh incompatibilities at boundary nodes.

Simulations allow for model interference detection and simplified fastener selection processes. When considering a program's budget, virtual testing of assemblies can greatly reduce overhead if used to highlight integration limitations. Additionally, CAD assemblies can alleviate or eliminate the cost of expensive component and system level prototype iterations. For example, flight and test units can be used interchangeably within a program if a combination of proto-qual test levels, adequate simulation and analysis data are utilized.

4.6 Sources of Uncertainty

In order to effectively utilize the TML evaluation discussed above, detailed understanding of error in both experimental test data and simulated model results must be established. Error is defined as a discrepancy between the physical truth and a prediction. Without the following comprehensive survey of error sources, any comparison of predictions would undoubtedly be incomplete and all resulting conclusions regarding the data and/or CAD tool irrelevant.

4.6.1 Experimental Uncertainty

As alluded to in the preceding sections, testing, either experimentally or through virtual simulations, can produce nothing more than a structural forecast. Of course, as the differences between model and system are minimized, such predictions converge on reality. In cases where this is not possible however it is important to understand what factors influence the truthfulness of a prediction. In experimental testing, for example, the mass and stiffness of support equipment can greatly impact the dynamics of a system. Instrument noise and internal errors in measurement devices can muddle test data as well. It has also been suggested that base bending of accelerometers and cable noise can contribute to errors in experimental readings.¹² As analyst, modeling such errors or even quantifying the resulting impacts, may not be feasible. It is paramount therefore that considerations be made for such factors in validation metrics and tool evaluations.

4.6.2 Simulation Uncertainty

Similar to the errors that exist in experimental data, simulation models also have several sources of uncertainty. Some of these sources are quantifiable, such as numerical errors, while others are more difficult to diagnose, i.e. simulation errors. Numerical errors occur from the computational processes utilized in solving FEA problems. Such processes include mesh generation and convergence as well as significant figure truncation. Simulation errors, on the other hand, can more generally be describe as

geometry errors in which the mathematical model fails to accurately describe the physical system.

Some common simulation errors and the associated FEA stage in which these uncertainties occur are shown in Fig. 4.5. The five largest uncertainties arise from supports, contacts, load values, linear materials, and failure criteria. The largest of these, supports, highlights the importance of a system’s boundary conditions. Due to the fact that such conditions drive the solutions of the nodes to which they are applied, it is imperative that representative supports be utilized. One example of a frequently employed boundary condition is the fixed or fully constrained entity. This boundary condition imposes zero values for each of the six displacements elements for a given node. Due to the difficulty in obtaining such rigidity in a physical system, such constraints generally do not perfectly describe the system under investigation.

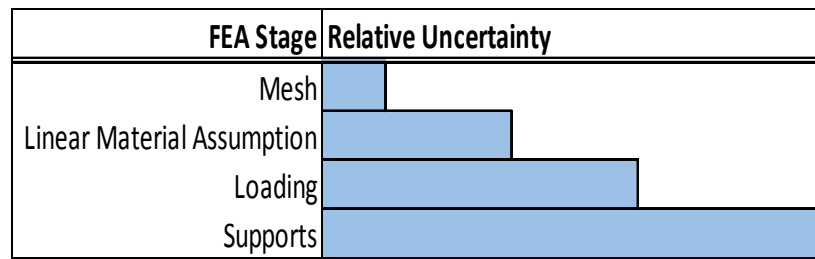


Figure 4.5. Relative uncertainty of FEA processes Modified from 5

In order to better understand the importance of boundary condition selection, a basic flat plate random vibration simulation was studied. For the study, a simple Aluminum 6061-T6 (Al 6061-T6) plate was subjected to both in-plane (X-Axis) and out-of-plane (Y-Axis) base excitations. For both simulations the plate was constrained with three unique sets of boundary conditions. Initially, the plate's bottom plane (-Y) was constrained with the above mentioned 'fixed geometry' boundary condition. Next, the simulations were carried out with a 'roller/slider' boundary condition on the bottom plane and 'fixed geometry' constraints applied at the large mounting holes (running along the Z-Axis). Lastly, the plate was constrained with 'roller/slider' conditions on the interior, cylindrical shafts of the mounting holes and 'fixed geometry' boundaries on the holes' circular bases. These three configurations and the accompanying boundary conditions represented a regression in rigidity due to a decrease in 'fixed geometry' surface area. The random vibration base excitation load and material assignment, for each axis' three boundary condition investigations, were identical. In other words, the simulations were utilized to isolate solution variance due to boundary condition rather than any of the aforementioned sources of uncertainty.

Figure 4.6 shows the results for the in-plane simulations. As was expected, the displacement of the plate gradually increased as the rigidity of the plate was decreased. For example, in the fully constrained bottom plane simulation, the relative displacement was roughly two orders of magnitude lower than that in the simulation where only the mounting holes were restrained. Additionally, in the first two boundary condition tests, where the bottom plane's Y-direction motion was restrained, only one peak frequency

was observed. The frequency peak occurred around 100Hz and significantly tapers off after approximately 200Hz. Conversely, in the final configuration, the plate exhibits two peak responses, one at 100Hz and another around 1500Hz.

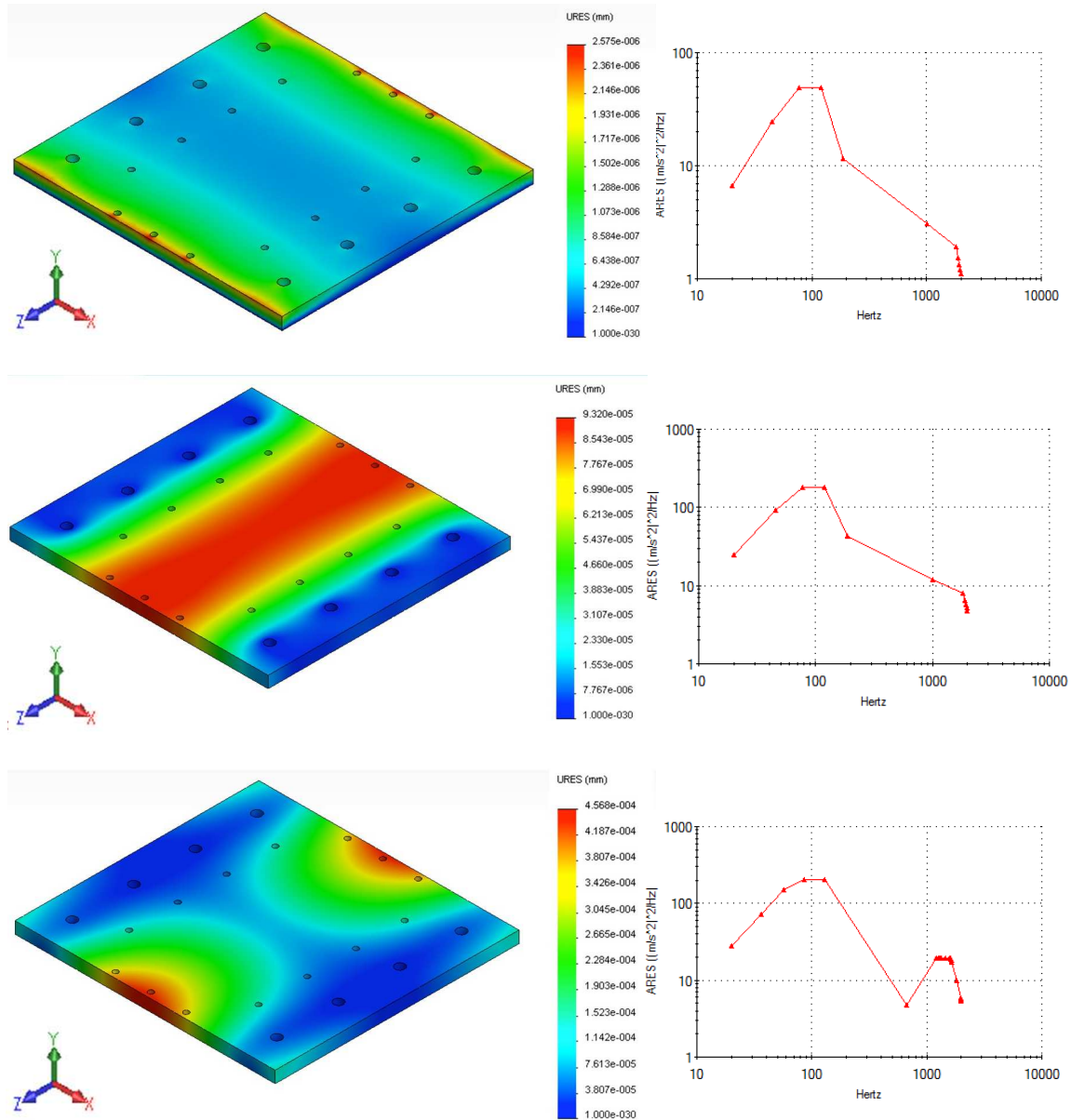


Figure 4.6. X-Axis results for three configurations: fully constrained bottom plane (top), roller/slider bottom plane and fixed holes (center), and fixed holes (bottom)

While the results on the in-plane simulations varied slightly between the three different boundary condition configurations, the out-of-plane simulations, Fig. 4.7, showed drastic disparities in frequency responses. This variation in results is understandable given the fact that the boundary conditions imposed on the bottom plane of the plate restrict displacements in the Y-direction. While in the first two plate configurations the bottom plane is modeled as a fixed geometry and roller/slider, respectively, the third configuration only restrains the plate's mounting holes. By allowing the plate to move relative to the holes, the results for the least rigid plate constraints highlight two distinct peak responses, with the maximum response occurring around 1500Hz. In the simulations where the plate's out-of-plane displacement was limited however, the frequency's maximum response occurred significantly lower, at approximately 50Hz.

Although the basic plate simulations were far more simplistic than the models investigated throughout this research, the general trends observed reveal important characteristics of boundary condition selection. Namely, the results of simulation where the system's motion is restrained normal to the axis of vibration are less sensitive to boundary condition selection than those in which the axis of vibration and boundary condition's reaction forces are parallel. This observation, while qualitative in nature, demonstrates how FEA results can vary depending on model supports.

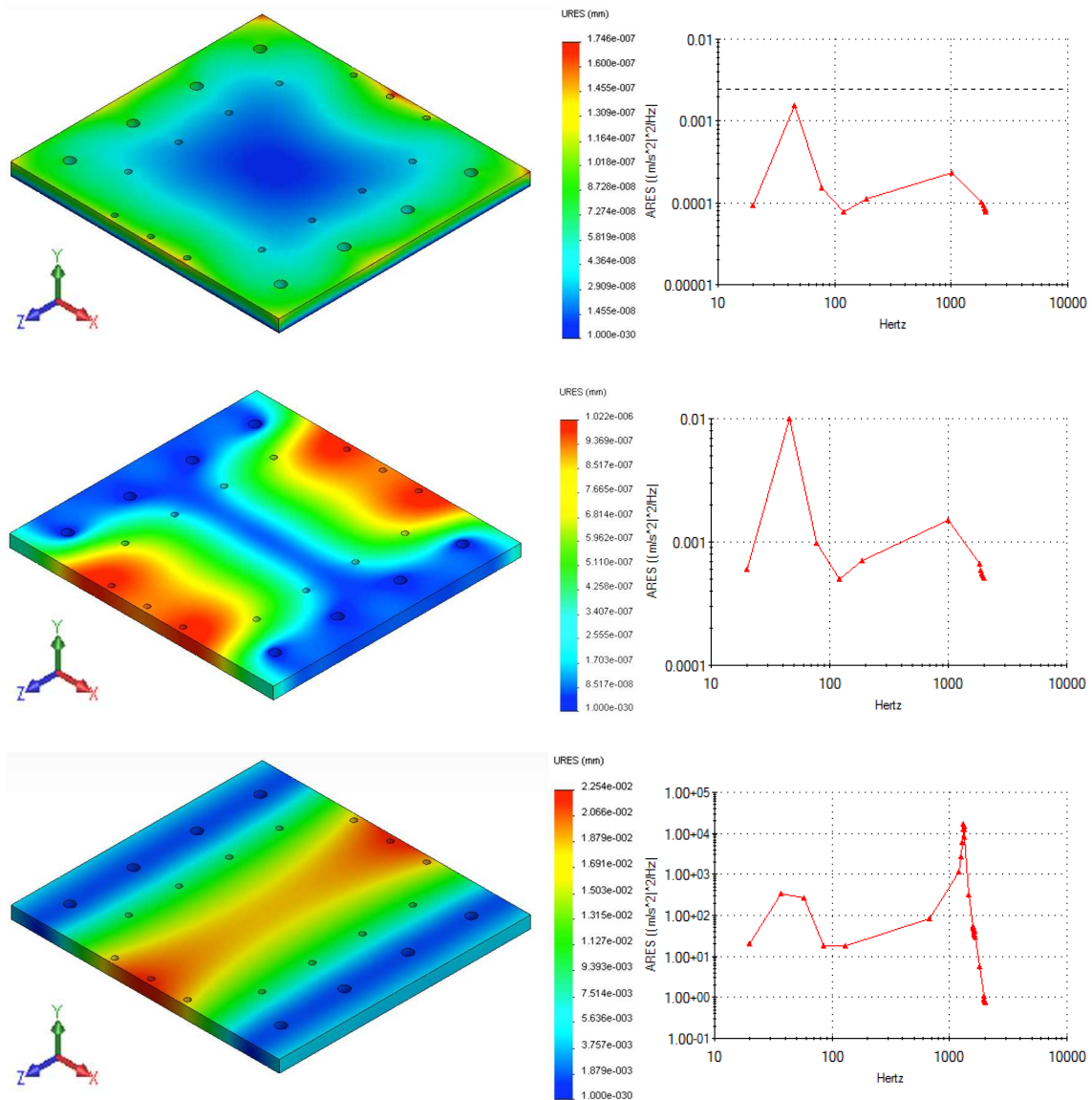


Figure 4.7. Y-Axis results for three configurations: fully constrained bottom plane (top), roller/slider bottom plane and fixed holes (center), and fixed holes (bottom)

Another large source of uncertainty arises from the material properties available in a CAD package's internal library. As is the case with most reported material properties, these values are not discrete points but rather representative averages of tested material distributions. Without taking a sample of each of the materials used in

manufacturing and performing a complete destructive testing regiment, a model's material properties are never completely known. Instead, analyst and test engineers alike must understand that tabulated material property values are averaged values of normal distribution bell curves and can vary greatly.

Irrespective of the uncertainty's source, it is especially important for CAD modelers to understand how errors accumulate, propagate and ultimately impact an FEA solution. To do this, sensitivity analyses can be conducted to study how various model changes impact the solution magnitudes as well as observed trends in results.

4.7 Validation Metrics and Post Processing

The above discussion highlights that while the steps summarized in Section 4.2 can help to ensure grid independent results, the processes outlined do not necessarily guarantee 'correct', 'accurate', or 'true' results. As discussed in Section 3, the validation of results is more involved than simply verifying the capability of software to accurately obtain pre-described benchmark solutions. Rather, validation involves employing the correct mathematical model, which is capable of fully and accurately describing a physical system of interest. In his paper, *Validation in Simulation: Various Positions in the Philosophy of Science*, George Kleindorfer from The Pennsylvania State University, highlights various metrics by which simulation validation is defined. Kleindorfer points out that validation approaches differ drastically among the various accepted doctrines. Kleindorfer states that measures of success range from professional acceptance (Kuhnianism), to proven derivation from empirical foundations (Rationalism), to

demonstration of useful predictive capabilities (Instrumentalism), and even include a general increase in the collective knowledge through participation or discourse (Hermeneutics).¹³ While there may be arguable worth to each approach, this work aims to blend ideas from two apparent extremes, objectivism and realism.

Objectivism is centered on the notion that a model is either valid or invalid, irrespective of the application or model user. This idea is facilitated by a binary, seemingly algorithmic, validation process which is based on empirical foundations. Objectivism makes no caveats for interpretation as the validation process is meant to transcend the user and rely solely on a common validation framework. Realism, on the other hand, suggests there is an undeniable relation between model and user. This ideology makes all models equally valid or invalid and the validation task an opinion driven process. Kleindorfer asserts both stances are plagued by a blatant disregard for discourse and that “in the former case, meaningful dialogue is stifled by an appeal to the foundation; in the latter, it is suppressed by asserting whatever the current opinion happens to be.”¹³ In order to blend these two apparently polar philosophies, the metrics utilized throughout this work will aim to evaluate models with objective reviews as well as through thoughtful discussions between model users and result stakeholders. Furthermore, each model will have program specific metrics with which a comparison of simulated and experimental results can be achieved.

5. COMPUTER AIDED DESIGN MODELS AND VALIDATION METRICS

In this research three independent programs were investigated. As briefly discussed earlier, each of these programs had unique goals and therefore required a varying range of information regarding the satellites' structural responses. In the subsequent sections, the processes used to generate useful models of each satellite are discussed. In some cases, more than one model was created to ensure computational resources were maximized. For example, simplified lumped mass models were deemed sufficient and thus utilized for vibration analyses while models with mixed materials were required for accurate thermal simulations. For each investigation the geometric CAD simplifications, material assignments, and mesh convergences for the models are presented. Also, the limiting assumptions, applied loads, and boundary conditions for each simulation are discussed. All structural response results and validation metric evaluations are summarized in Section 6.

5.1 The Space-based Telescopes for Actionable Refinement of Ephemeris Structural Payloads and Test Pod Models

As previously discussed, the STARE 3U CubeSat featured three independent modules: an optical payload/image processing segment, a centralized attitude control unit and a power storage compartment. This research looked at two different versions of the STARE payload module, Version 2 (V2) and Version 3 (V3). Due to the proprietary

nature of the STARE program, images depicting internal components of either payload were omitted from this report. These components primarily include optical lenses, baffles, mounting hardware (including inserts and screws), various spacers and printed circuit boards (PCB). The primary differences between the V2 and the V3 payload included simplifications made to a multi-piece optical baffle, utilized in V2, and a size increase in the lens assembly for the V3 iteration.

In order to ensure the design integrity of the optical lenses and PCBs, the V2 and V3 imager models were subjected to dynamic analyses. The dynamic analyses of these payloads feature an NPS designed test pod³⁹ model, identical to the physical experimental interface, in order to predict behavior during testing most accurately. While the test pod design was admittedly more rigid than the satellite bus structure, experimental and simulated testing aimed to predict payload, rather than system, responses.

5.1.1 Version 2 Computer Aided Design Model

In generating the 3D CAD model for V2, geometric simplifications were made exclusively within the lens assemblies. Simplifications included: modeling concave lens components as silica cylinders and eliminating thin polyimide parts to reduce mesh complexity. Perhaps the largest modification made to the modeled V2 parts was a simplification of an internal threaded ring used to connect the imager assembly to the lens assembly. The simplification of the ring to support a clearance fit between the two components reduced the computational complexity of the model without removing

significant inertia participation. As mentioned above, the simulation model also featured an aluminum test pod, which supported the optical payload and served as an interface with the slip table. The CAD of the test pod with the payload internally modeled and the physical test structure mounted to an interface plate are depicted in Fig. 5.1, below.

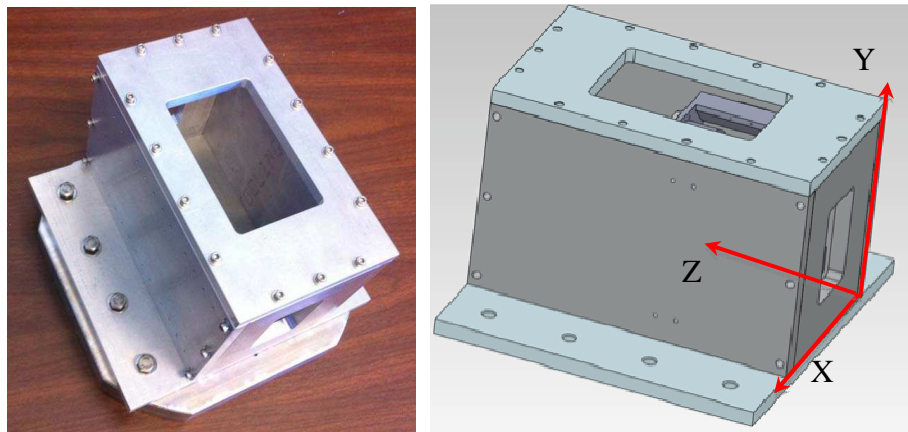


Figure 5.1. Physical test pod (left)³⁹ and modeled test pod with coordinate system (right)

5.1.2 Version 3 Computer Aided Design Model

In addition to the differences between the V2 and V3 payloads already discussed, the V3 imager model exclusively included a Viton® ring and a monolithic optics holder. As with the V2 model, in order for the model to consistently mesh without component-specific controls, some manufacturing features were suppressed. Such features included fillets along the base of the optics holder as well as all setscrews and epoxy holes. While the V3 lenses were significantly larger than those in the V2 payload, de-featuring was unavoidable resulting in the components being modeled as cylinders rather than concave

volumes. Similarly, the de-featuring utilized for the V2 internal threaded connector ring was maintained in the V3 simulation to minimize complexity.

Due to the similarity of the payloads, some component models remained unchanged between the initial and secondary design iteration. Table 5.1 shows the material properties used in the both the V2 and V3 model. Materials listed towards the bottom of the table, under the double line, were utilized in the V3 model only.

Table 5.1: STARE Payload Model Material Properties

<u>Material</u>	<u>Young's Modulus (MPa)</u>	<u>Mass Density (kg/m³)</u>	<u>Yield Strength (MPa)</u>
Invar 36 ⁴⁰	137000.0	8150.0	206.0*
Fused Silica [†]	73000.0	2200.0	50.0 [‡]
FR4/G10 [§]	18600.0	1820.0	241.0
Al 6061-T6	69000.0	2700.0	275.0
Viton ⁴¹	600.0	1931.0	9.0
A286 SS	201000.0	7920.0	275.0
SE4486 [¶]	9.1	2590.0	4.1
Polyimide [#]	2500.0	1430.0	69.0
Ceramic Porcelain	220000.0	2300.0	172.0

* "Eagle Applies Corporation," June 2013. <http://www.eaglealloys.com/c-7-invarsuper-invar.html>

† "Fused Silica, SiO₂ Material Properties," June 2013. <http://accuratus.com/fused.html>

‡ "Fused Silica (SiO₂) UV Grade," June 2013. http://www.internationalcrystal.net/optics_09.htm

§ "K-Mac Plastics," June 2013. <http://k-mac-plastics.net/>

¶ "Thermal Interface - Wet Dispensed SE4486 Thermally Conductive Adhesive," Ref No. 11-1890-0, Dow Corning, June 2013

"Summary of Properties for Kapton Polyimide Films," DuPont Datasheet, June 2013. http://www2.dupont.com/Kapton/en_US/assets/downloads/pdf/summaryofprop.pdf

Unless otherwise noted, the materials listed in the table were utilized directly from the SolidWorks material library. Tensile and flexural strengths for G10/FR4 epoxy were used in lieu of Young's Modulus and Yield Strength, respectively. While these estimates were higher than the Young's and Yield values replaced, the modeled components were not considered structural and were significantly smaller than the majority of parts in the assembly. The material properties listed in Table 5.1, as discussed in Section 4, play a large role in the accuracy of the solution obtained by the FEA solver.

5.1.3 Version 2 Boundary Conditions and Model Constraints

The V2 model was restrained along the bottom plate of the test pod. This plane was modeled as a 'fixed geometry' in the simulation, which imposed a null set for all three rotational and three translational degrees of freedom. This constraint was utilized to approximate the physical restraints on the test pod.

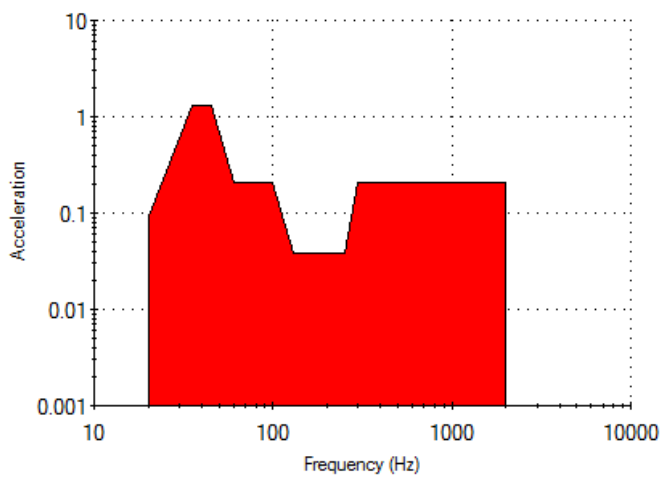
A damping ratio of 0.02 was applied to the V2 assembly. This value was a low estimate for damping in continuous metals (0.02-0.04) or metal structures with joints (0.03-0.07).⁴² Had a higher value for damping been utilized, the model dynamics would have been allowed to more closely approach a critically damped or over damped state. The damping ratio applied was therefore conservative in nature and lead to higher observed levels of vibration. Due to the fact that the V2 structural model was meant to capture trends observed during testing, this set of constraints was thought to closely capture the physical boundary conditions of the vibe table and elicit the desired results.

5.1.4 Version 2 Simulated Loading

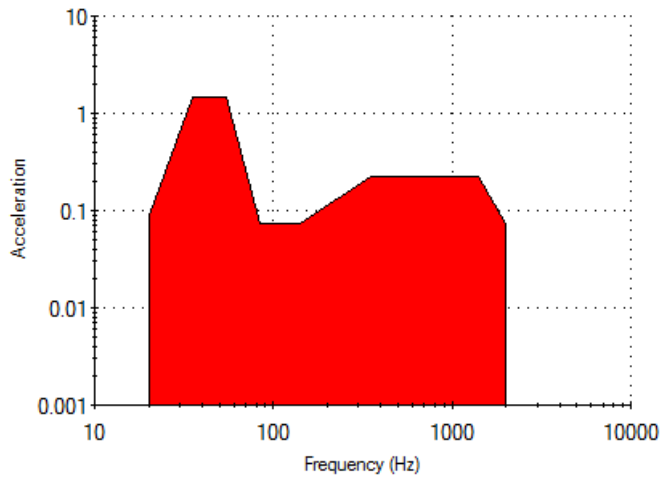
A natural frequency analysis was performed on the V2 model in order to determine the resonant frequencies of the imager assembly. The first five natural frequency modes were of principal importance due to potential for overlap with the launch vehicle environment. To further investigate possible coupling, a dynamic analysis simulation was conducted at representative test loads. Experimental test loads, rather than launch loads, were used to emphasize dangerous frequency coupling.

While early iterations of the V2 analysis utilized representative test levels, the data presented in Section 6 of this report corresponds to the OUTSat program's proto-qualification levels. The proto-qual vibration profiles shown in Fig. 5.2 match those loads experienced in P-Pod slots 7 and 8 of the NPSCul, where the STARE payload was manifested for launch. For the purposes of recreating experimental test data with the aforesaid simulation model, two of the test profiles (the X-Axis and Y-Axis) were scaled to $20g_{RMS}$ while the third (Z-Axis) was scaled to $19.87g_{RMS}$. The slightly lower value in the third axis was a result of hardware constraints during physical testing.³⁹ Results of the analyses subjected to the below environmental loads are presented in Section 6 as the primary TML evaluation standards.

P-POD #3 Test Levels (X-Axis)		
Frequency (Hz)	ASD (g^2/Hz)	
	Proto-Qual	Scaled to 20 G_{RMS}
20	0.060	0.0923
35	0.850	1.3000
45	0.850	1.3000
60	0.130	0.2060
100	0.130	0.2060
130	0.020	0.0376
250	0.020	0.0376
300	0.130	0.2060
2000	0.130	0.2060
G_{RMS}	16.13	20.00



P-POD #4 Test Levels (Y-Axis)		
Frequency (Hz)	ASD (g^2/Hz)	
	Proto-Qual	Scaled to 20 G_{RMS}
20	0.120	0.0895
35	2.000	1.4900
55	2.000	1.4900
85	0.100	0.0746
140	0.100	0.0746
350	0.300	0.2240
1400	0.300	0.2240
2000	0.100	0.0746
G_{RMS}	23.15	20.00



P-POD #4 Test Levels (Z-Axis) – Payload Test Levels		
Frequency (Hz)	ASD (g^2/Hz)	
	Proto-Qual	Scaled to 19.87 G_{RMS}
20	0.060	0.2220
70	0.440	1.6300
140	0.440	1.6300
220	0.050	0.1850
400	0.050	0.1850
600	0.010	0.0371
800	0.010	0.0371
1100	0.040	0.1480
1600	0.040	0.1480
2000	0.010	0.0371
G_{RMS}	10.29	19.87

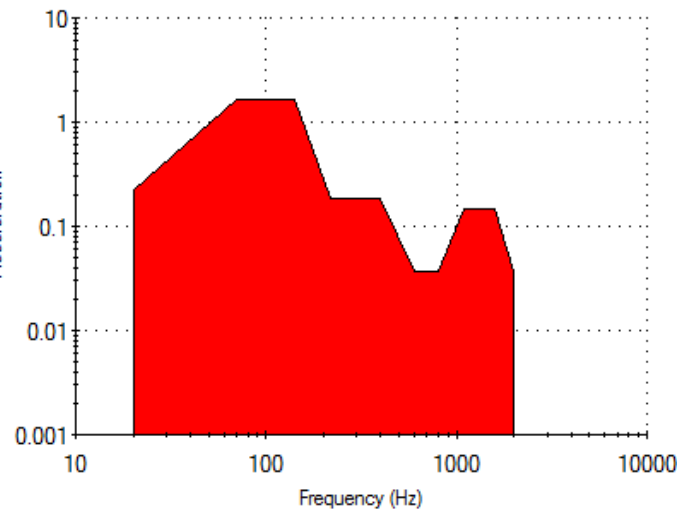


Figure 5.2. OUTSat test level profile as applied in SolidWorks

5.1.5 Version 2 Mesh Convergence

In order to ensure grid independent solutions, a mesh convergence study was conducted for the V2 payload prior to running final frequency simulations. The study of convergence using the first mode of natural frequency is shown in Fig. 5.3. The figure depicts the first modal frequency response of the V2 model at various nodal counts. Nodes in the mesh were increased from 200K to just fewer than 1.1M nodes. Despite a frequency drop of approximately 15Hz, the result begins to converge between 700K and 1.1M. Relative to the prior regression, a drop of this magnitude was deemed acceptable for this research. Ultimately, a maximum element size of 4mm was utilized for the frequency testing of the V2 payload. This element size generated a mesh with approximately 700K nodes.

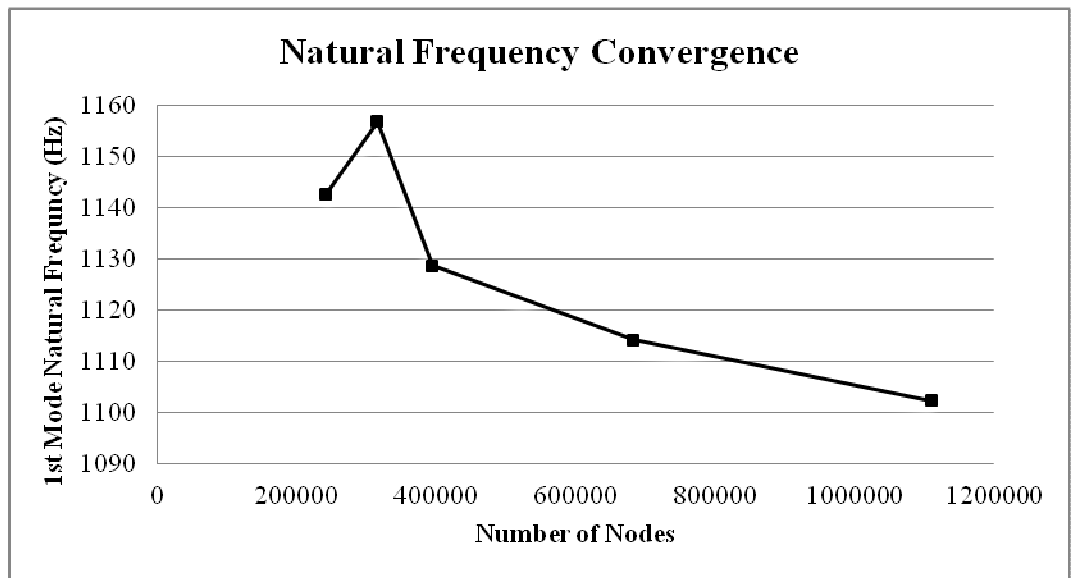


Figure 5.3. STARE V2 mesh convergence data

5.1.6 Version 2 Validation Metrics

As previously mentioned, the validation metrics used throughout this research were aimed at impartially reviewing simulation results on the merits of accuracy as well as critically evaluating the usefulness of said results for a program's needs. To do this, 'accuracy' and 'need' were defined thoroughly for each program (model) independently. "Accuracy is defined as the closeness of agreement between a simulation/experimental value and its true value."⁴³ From an engineering standpoint however, this truth is very often difficult to model exactly and can result in a complex validation process. Rather, "a statistically meaningful comparison of computational results with experimental measurements over the range of intended use may be sufficient"¹⁰ for model validation. Need, on the other hand will qualitatively define the purpose of the simulation from a mission success standpoint.

For V2, the first iteration of the STARE payload design was being investigated. Due to the exploratory nature of the mission and an elementary understanding of the solver's limitations, the 'need' for the V2 simulation was investigative, at best. All parties involved had a verbalized interest in the capabilities of the software. 'Accuracy' in the V2 study was therefore defined as the simulation's ability to capture experimental result trends and predict relative responses.

Strictly for the purposes of this research, the above metric was assigned a quantitative success criterion. This value, while seemingly arbitrary, represents frequency response variations between simulated and experimental values which would be reasonable provided a simplified model and imperfect boundary conditions were

implemented. To quantify these metrics, peaks in a component's simulated random vibration response within plus/minus half an order of magnitude of experimental were deemed successful. It is important to reiterate that because experimental data is not without error, these comparisons were not a validation to absolute truth but rather a metric by which to evaluate the simulation's ability to recreate 'real world' responses within certain error bounds.

5.1.7 Version 3 Boundary Conditions and Model Constraints

The V3 model was restrained at the bottom plate of the test pod, along the interface plane between the shaker table and structure. This constraint, identical to that utilized in the V2 simulation, was meant to mimic the no penetration condition imposed by the shaker table on the test pod. As mentioned in Section 4, the fixed geometry constraint/boundary condition, particularly when applied to an entire face, is generally overly restrictive in modeling the physical case. This is especially true in predicting higher frequency responses for axes which run parallel to the boundary conditions' reaction forces. Due to the fact that this structural model was meant to investigate payload responses, rather than the physical response of the entire experimental system (payload, test pod, vibration table), this constraint was deemed appropriate for the application. In other words, enforcing a fully fixed bottom test pod plate in this simulation isolated the response of the payload and allowed for the investigation to focus solely on internal interactions, stress concentrations, and relative component motion. While programmatically such internal interactions were important to both payload

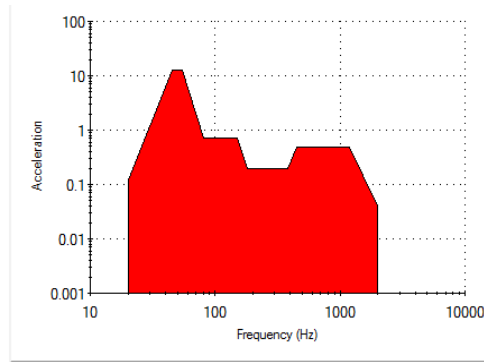
survivability and mission success, boundary condition limitations, as previously discussed, coupled with external test sensors imposed model validation difficulties. A more in-depth discussion on V3 metrics is presented below.

Similar to the V2 payload, the V3 model utilized a damping ration of 0.02. Again this value was on the low end of published values for metal structures with joints yet was believed to represent the worst case damping scenario. Higher damping ratio values could have artificially stiffened the CAD model and masked what might have otherwise been high frequency responses.

5.1.8 Version 3 Simulated Loading

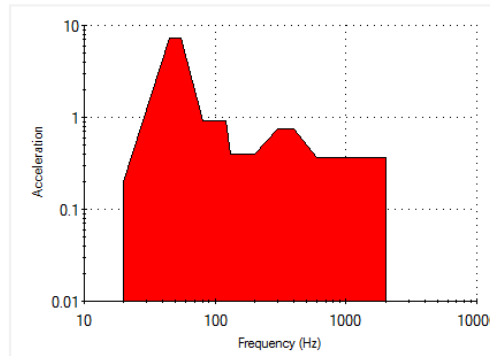
In the dynamic testing of the V3 payload, GEMSat random vibration test levels prescribed the base excitations utilized for each of the axes simulated. As with the V2 model, all three axes were simulated individually over a frequency range of 20-2000Hz. As previously discussed, qualification test levels, rather than acceptance or proto-qual levels, were used to represent worst-case payload environments. The overall RMS g-loading values applied to the X, Y and Z-axes, respectively were 30.3g_{RMS}, 31.8g_{RMS}, and 21.0g_{RMS}.⁴⁴ The profiles for each major axis, as applied in SolidWorks, are shown on the following page, Fig. 5.4.

X-Axis			
Freq, Hz	ASD, g ² /Hz		
	Acceptance	Protoqual	Qual
20	0.03	0.06	0.12
45	3.15	6.3	12.6
55	3.15	6.3	12.6
80	0.17	0.35	0.70
150	0.17	0.35	0.70
180	0.05	0.1	0.2
380	0.05	0.1	0.2
450	0.12	0.24	0.48
1200	0.12	0.24	0.48
2000	0.01	0.02	0.04
Overall Grms	15.1	21.4	30.3



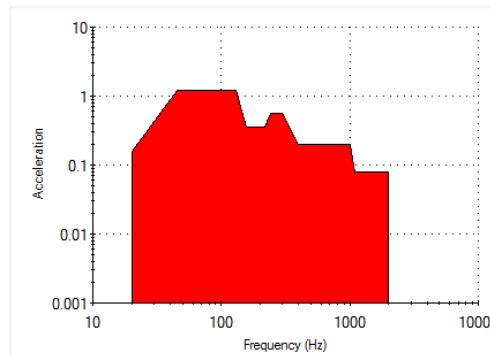
■ Acceleration (g)

Y-Axis			
Freq, Hz	ASD, g ² /Hz		
	GEMSat Acceptance	GEMSat Protoqual	Qual
20	0.05	0.10	0.20
45	1.80	3.60	7.20
55	1.80	3.60	7.20
80	0.23	0.46	0.92
120	0.23	0.46	0.92
130	0.10	0.20	0.40
200	0.10	0.20	0.40
300	0.19	0.37	0.75
400	0.19	0.37	0.75
600	0.09	0.18	0.36
2000	0.09	0.18	0.36
Overall Grms	15.9	22.5	31.8



■ Acceleration (g)

Z-Axis			
Freq, Hz	ASD, g ² /Hz		
	Acceptance	Protoqual	Qual
20	0.04	0.08	0.16
45	0.30	0.60	1.20
130	0.30	0.60	1.20
155	0.09	0.18	0.36
220	0.09	0.18	0.36
240	0.14	0.28	0.56
300	0.14	0.28	0.56
400	0.05	0.10	0.20
1000	0.05	0.10	0.20
1100	0.02	0.04	0.08
2000	0.02	0.04	0.08
Overall Grms	10.5	14.8	21.0



■ Acceleration (g)

Figure 5.4. GEMSat X-Axis, Y-Axis, and Z-Axis test level profile as applied in SolidWorks

5.1.9 Version 3 Mesh Convergence

As with the earlier V2 model, a convergence study was completed for the V3 payload of the STARE program. Figure 5.5, shows the first mode resonant frequency of the V3 structure at various node counts. Only the first mode is shown below because the model showed similar convergence curves for all five modes, as was expected. For V3 convergence simulations, the maximum number of nodes generated was 1.9M. This value was generated with a maximum element size of 2.3mm. While higher density meshes may have shown a more converged solution, performance limitations as well as run times limited the investigation.

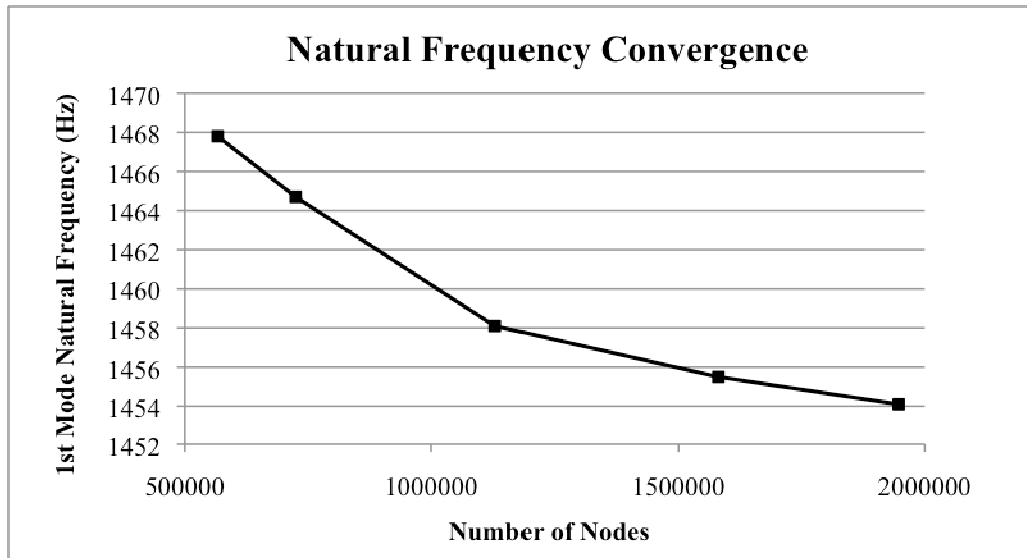


Figure 5.5. STARE V3 mesh convergence data

Due to fact that the last two points simulated (which differed by node counts of over 300K) only demonstrated a 2Hz drop in nodal frequency and based on the decreasing derivative of the trend line's slope, the natural frequency results in the following section were considered converged to within $\pm 5\text{Hz}$. This frequency range is not to be confused with the accuracy of the results; rather the 5Hz value represents the expected solution variance given an infinitely smaller maximum mesh element size. Any programmatic need for more precise simulation resolution would have required further de-featuring of payload components or more complex mesh controls.

5.1.10 Version 3 Validation Metrics

Both the aforementioned observations regarding boundary condition selection/result limitation and the lessons learned from the earlier V2 iteration were considered in developing V3 validation metrics. Due to the fact that experimental testing for the V3 is ongoing, the following metrics were not evaluated within this body of research. The below are presented therefore as suggestions for validation of the impending experimental predictions.

Due to the similarities between the V2 and V3 payloads and the V2/V3 test levels, the suggested validation metrics for V3 are comparable to those presented above. Slight differences between the two metric sets however, are needed to reflect a more mature payload design and higher success criterion for the V3 mission. The 'need' for model validity in the V3 simulation therefore represents a heightened expectation to meet more demanding standards. As in the V2 model, 'accuracy' in the V3 study should

be defined as the simulation's ability to capture experimental result trends and predict relative responses. This definition, while seemingly redundant to the V2 metric, served to foster confidence in the TML and V2 metric assessments. Without such metric repetition, any comment on simulation validity could have been confounded by specific model happenstance. Therefore, to quantify accuracy for the V3 model, peaks in random vibrate responses are again expected to be within plus/minus half an order of magnitude with respect to experimental values.

5.2 The Space-based Telescopes for Actionable Refinement of Ephemeris Thermal Models

As previously discussed, thermal analyses were also performed for the STARE program in an effort to characterize on-orbit thermal profiles for two different satellite flight configurations. Such profiles were needed to ensure that operational temperature ranges could be maintained throughout various stages of the mission. Specifically, the initial thermal analysis aimed at presenting feasible options for maintaining a V3 Complementary Metal-Oxide-Semiconductor (CMOS) digital image sensor within a safe temperature range while the latter focused more closely on software capability.

Stemming from the results of the first analysis, a thermal strap design capable of achieving the desired results for either of the flight configurations was suggested. The thermal management design included strap sizing, system pricing, and viable strap interface locations which were identified by probing simulated components within the model. The predicted temperature profiles and the recommended CMOS sensor

configuration for the Colony I (CI) and Colony II (CII) satellite flight configurations are discussed with further detail in the following sections.

Internally, the CI and CII models were identical; both featured a V3 payload and had comparable power loads applied. Neither simulation model featured components below the payload module; rather, representative loads were applied in appropriate locations. This simulation simplification, justified by the goal of payload specific design needs, saved computational resources and streamlined the CAD modeling process. Perhaps the largest drawback to excluding non-payload components was a notable decrease in viable heat transfer avenues. By limiting the possible paths for conduction, the results of the simulations may have been slight overestimate yet definitely represent the worst possible survivability environment.

Externally, the CII model featured a "flat" external panel/solar cell configuration while the CI solar panels were designed in a more traditional "shuttlecock" style. Figure 5.6 shows both configurations as modeled in SolidWorks.

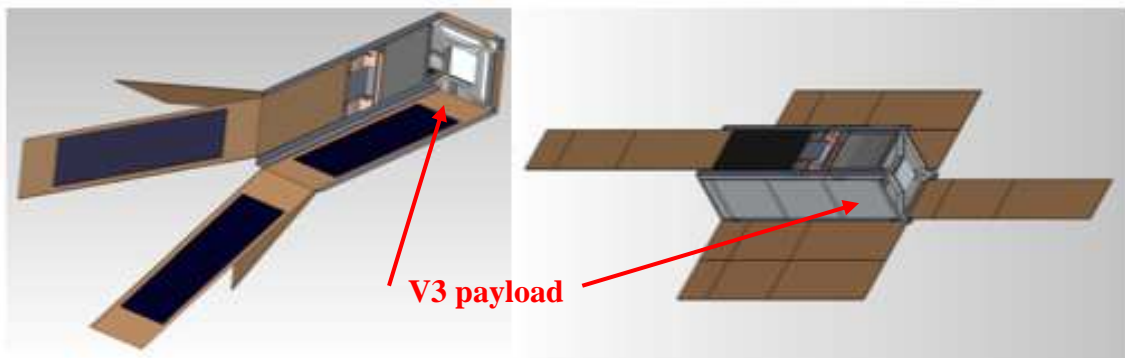


Figure 5.6. Simplified Colony I (left) and Colony II (right) models

5.2.1 Colony I and Colony II Thermal Simulations

The thermal analysis of the CI STARE configuration investigated two flight beta angles, β ; while the CII simulation focused on a single β . Beta angles are used in orbital mechanics to describe the orientation of an orbit plane with respect to the sun-satellite vector. At the time of these analyses, the exact β for the STARE mission was unknown. Therefore, representative values were utilized in an effort to bracket the thermal responses. In order to capture as many attitude specific heat loads as possible, two orbit extremes, $\beta=0^\circ$ and $\beta=90^\circ$, were investigated. The $\beta=0^\circ$ case, used only for the CI investigation, prescribed a transient heat transfer environment allowing the satellite to periodically enter into eclipse and then rise locally into sunlight again. Due to the satellite's motion in the $\beta=0^\circ$ case and the cyclic relief from direct sunlight it created, this simulation generated the lower temperature bounding environment. Conversely, the $\beta=90^\circ$ case, used for both the CI and CII configurations, represented a continual solar flux exposure orbit and was used as a steady state high temperature bounding simulation. For both β cases, the altitude of each satellite was maintained at 700km and the temperatures at the points of interest were measured after three orbits. Simulation durations of three orbits were chosen to represent quasi-steady states for the spacecraft.

The temperature profiles generated from these analyses were then used as inputs into a thermal resistance model. The thermal resistance draws on an analogous relationship between Ohm's law, Eq. (5.1), and the equation for one-dimensional, conductive heat transfer, with no internal energy generation, Eq. (5.2).

$$R_e = \frac{L}{A\sigma} = \frac{E_1 - E_2}{I} \quad (5.1)$$

$$R_i = \frac{x}{Ak} = \frac{T_1 - T_2}{q_x} \quad (5.2)$$

In Eq. (5.7), R_e is the electrical resistance of a component (Ω), L is the length traveled (m), A is the surface area (m^2), σ is electrical conductivity ($S \cdot m^{-1}$), E is the voltage (V), and I is the current (A). Likewise, in Eq. (5.8), R_i is the thermal resistance ($^{\circ}K/W$) of a given component, x is the length of the segment (m), A is the cross sectional area (m^2), k is a material property known as thermal conductivity ($W/^{\circ}K \cdot m$), T is temperature ($^{\circ}K$), and q is the heat transfer (W).⁴⁵ The thermal resistance model for each of the STARE program configurations, briefly discussed in Section 6, featured all internal components between a notional thermoelectric cooler and the spacecraft bus. Individual components had unique thermal resistances based on material properties and part geometries that created a network of resistances capable of being analyzed using standard summation rules of resistivity.

5.2.2 Thermal Computer Aided Design Models

In the interest of reserving computational power, simplified geometric models were utilized for the thermal simulations of both flight configurations. Primarily, such simplifications were employed in an effort to ease the computational burden of meshing along complex curves and to mitigate model interference errors. Throughout the de-featuring of the models great care was taken to preserve 'thermally influential' physical

properties. For example, each simplified component model maintained the originally specified material assignment (thermal conductivity), interface contact area (cross sectional area), and overall volume (thickness of heat transfer path). By maintaining the aforementioned traits, the one dimensional heat transfer through any part or collection of parts was preserved, thus justifying the use of Eq. (5.2) and drastically limiting the effects of such simplifications on thermal results.

In addition to the V3 payload materials already summarized in Table 5.1, the Colony I and Colony II thermal models also featured gallium arsenide (GaAs) solar cells. The material properties of GaAs are shown in Table 5.2.

Table 5.2: Exterior STARE Payload Material Properties

<u>Material</u>	<u>Young's Modulus</u> <u>(GPa)</u>	<u>Mass Density</u> <u>(kg/m³)</u>	<u>Yield Strength</u> <u>(MPa)</u>
GaAs	85.5 ⁴⁶	5320.0 ⁴⁶	2700.0 ⁴⁷

Furthermore, in the context of externally modeled thermal planes, two additional material properties were of particular interest for the net heat transfer of the satellite. These properties, reported on the following page in Table 5.3, are known as absorptivity and emissivity. Absorptivity, α , is defined as the percentage of incident energy on a surface, which is absorbed into the body. Emissivity, ϵ , on the other hand, is a value that represents a body's ability to radiate energy.⁴⁸ Emissivity is usually measured experimentally and reported relative to a black body's radiation potential, $\epsilon=1$.

Table 5.3: STARE Payload Thermal Material Properties

<u>Description</u>	<u>Emissivity</u> *	<u>Absorptivity</u> *
Deployable Panel (nadir faces) -Copper PCB surface [†]	0.03	0.32
Deployable Panel (space faces) -Copper PCB surface -GaAs Cells	0.03 0.85 [‡]	0.32 0.92
Body Mounted Panels -Clear anodized aluminum frame -Copper PCB surface -GaAs Cells	0.76 0.03 0.85	0.27 0.32 0.92
GPS Antenna Face -Clear anodized aluminum frame -Copper PCB surface	0.76 0.03	0.27 0.32
Telescope Aperture -Polished silver mirror surface -Clear anodized aluminum plate -Black anodized Invar 36 frames	0.02 0.76 0.87	0.04 0.27 0.67
Nadir Panel -Copper PCB surface -GaAs	0.03 0.85	0.32 0.92
Sun Facing Solar Panels and Body Panel -Clear anodized aluminum frames -Silver Teflon Taped Body PCB Surface -GaAs Cells	0.76 0.08 0.85	0.27 0.07 0.92
Radiator Panels -Silver Teflon Taped Body PCB Surface	0.08	0.07
Space Facing Panels and Body Facing Exterior -Clear anodized aluminum frame -“Black Plastic” coated PCB -“White Plastic” coated solar panel backing	0.76 0.85 0.13	0.27 0.96 0.81
Telescope Aperture -Polished silver mirror surface -Clear anodized aluminum plate -Black anodized Invar 36 frames	0.02 0.76 0.87	0.04 0.27 0.67
Nadir Panel -Silver Teflon Taped Body PCB Surface	0.08	0.07

* Unless otherwise noted, material properties obtained from Spacecraft Thermal Control Handbook⁴⁹

[†] The surfaces of the PCBs were approximated as copper. This is thought to be a conservative assumption, as on-orbit conditions will include a reflective, tinted surface layer, like Kapton, and should reflect additional heat flux.

[‡] "28.3% Ultra Triple Junction (UTJ) Solar Cells," Spectrolab Photovoltaic Products, Spectrolab, A Boeing Company, 2008.

Due to the fact that heat transfer in space is limited to conduction and radiation alone, the above values highly impact thermal simulation results. Emissivity and absorptivity values for CI are listed at the top of the table while CII data is presented in the bottom half of the table, below the double line.

5.2.3 Thermal Inputs and Boundary Conditions

As previously mentioned, two flight scenarios were investigated as part of the Colony I-STARE thermal analysis. For each of these simulations, power data was taken wherever possible from published program documentation and LLNL specified datasheets, Table 5.4. One exception to this was the power load utilized to represent an internal radio unit that had yet to be specified at the time of the simulation. Rather, a representative radio unit, capable of meeting mission requirements, was used for this power load.^{50, 51} The model utilized the specified 'idle' power for the transceiver as the spacecraft was expected to scan for ground signals long term, but not actively transmit during conjunction events.

Table 5.4: Itemized Spacecraft Heat Power Loads

<u>Imager/PEC</u>	
Maximum Peltier Load	7.6W ⁵²
Imager Load	0.3W ⁵³
<u>GPS Board</u>	1.2W ⁵⁴
<u>Antenna Power</u>	1.3W ⁵⁵
<u>ADACS Power</u>	1.5W ^{50, 56}
<u>Main Bus</u>	
Processor Module	0.7W ⁵⁰
C-II Transceiver (receive mode)	0.5W ⁵¹

Utilizing the total advertised power draw as raw thermal loads was admittedly conservative because some portion of these values is utilized in carrying out the desired functionality of a component. This overestimate of power input meant that simulation solutions would err on the hot side and serve as the worst-case thermal environment. Figure 5.7 below shows the internal panel naming convention utilized to discuss the external loads applied to both the CI and CII spacecraft.

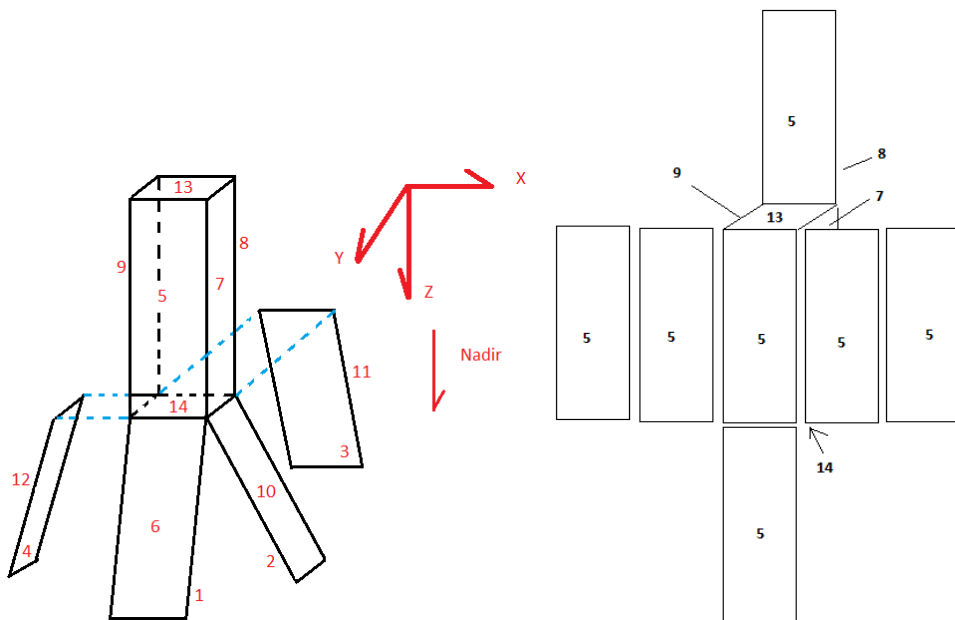


Figure 5.7. Panel nomenclature of Colony I and Colony II configurations

In both the CI and CII $\beta=90^\circ$ steady-state scenarios, loads were applied to simulate an orientation in which surface 8, the GPS antenna panel without solar cells, pointed away from the sun. This was achieved by maintaining a zero magnitude solar flux condition on surface 8 throughout the totality of the simulation. Conversely, a

continual solar flux load with a direct angle of incidence was imposed on surface(s) 5. Applied loads also were used to simulate a flight configuration in which the long axis of the satellite held a radial alignment on the orbit plane with the payload module pointing towards zenith, panel 13. This orientation provided constant Earth albedo and IR loads on the bottom panels, surfaces 1-4 and 14. All non-Earth facing surfaces were allowed to fully radiate to cold space. The small angular size of the Sun, relative to the rest of the sky, justified applying full view factors for cold space radiation on sun facing surfaces as well. Figure 5.8 depicts the physical orbits, for both the Colony I and Colony II configuration, which were represented by the simulated external loads discussed above.

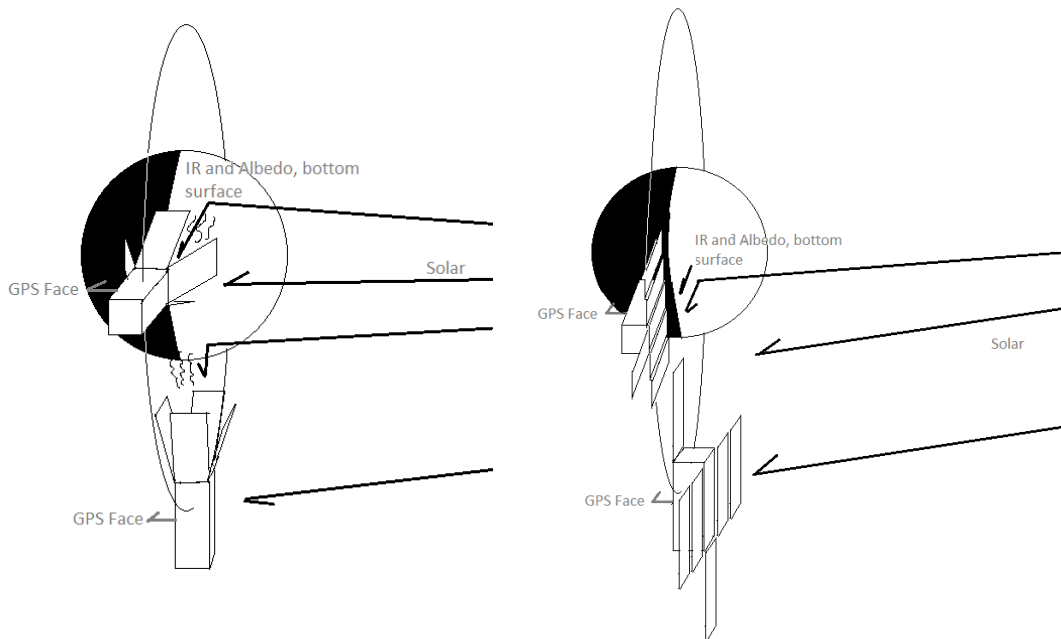


Figure 5.8. $\beta=90^\circ$, steady-state scenario and spacecraft orientations

In addition to the steady-state model, described above, a transient $\beta=0^\circ$ case was also simulated for the Colony I configuration. The transient model was used as a means of bounding the problem and to analyze how the spacecraft's thermal environment would vary if the orbit featured periods of eclipse. For this simulation, loads were utilized to impose the configuration shown in Fig. 5.9. As depicted, the spacecraft was oriented such that surface 8 pointed along the velocity vector of the spacecraft's orbit. Sun inputs were generated individually for each off-velocity, sun-facing surface. These time varying curves simulated the hemispherical tracks of the sun physically rising, traversing, and setting on each panel. Albedo was also varied on the bottom surfaces but discretely, either 0% or 100%, depending on if the spacecraft was in eclipse or sunlight, respectively. Both time dependent loads, as applied in SolidWorks, as well as the MATLAB script utilized to generate these scaling curves, are given in the Appendix. As in the steady-state case, all surfaces were modeled as continually radiating to cold space except for those facing Earth, which radiate to the planet's surface.

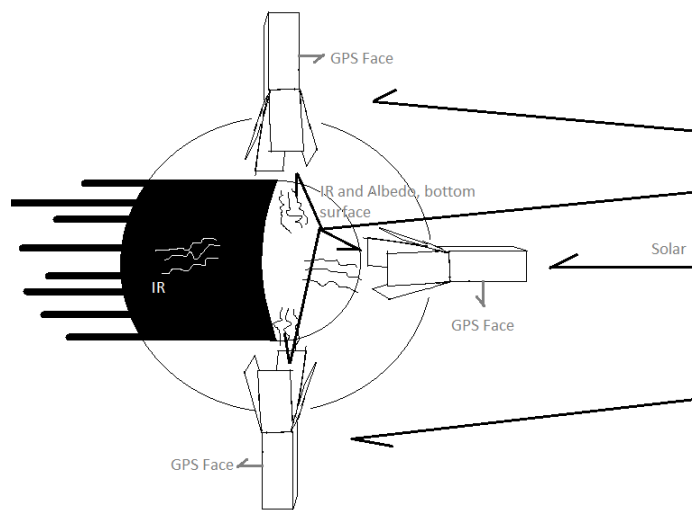


Figure 5.9. Colony I $\beta=0^\circ$, transient scenario and spacecraft orientation

The assumed value for solar flux utilized for all simulations was $1367\text{W}/\text{m}^2$.⁵⁷ This value was multiplied by the absorptivity of each incident surface as well as the cosine curves if applicable. Earth infrared (IR) loads were computed with shape factors interpolated from Space Mission Analysis and Design (SMAD).⁵⁸ The peak IR flux value used was $237\text{W}/\text{m}^2$.⁴⁹ The Albedo flux utilized was $629\text{W}/\text{m}^2$. This value represented the product of solar flux, percent albedo⁴⁹, and shape factors determined from Tables 11-45A, D-7 and D-8 in SMAD.⁵⁷ The shape factors used for various simulated scenarios are summarized below in Table 5.5. Spacecraft to ground radiation utilized the appropriate material emissivity and shape factors. Additionally, a background Earth temperature of 290°K ⁵⁹ was utilized. Radiation to space on all other faces operated under a 2.7°K background temperature and used assigned shape factors of 1 due to the previously discussed assumption that relevant faces had ‘full sky’ views.⁶⁰

Table 5.5: Simulation Shape Factors Used

<u>Description</u>	<u>Shape Factor, F</u>
IR Factor, nadir facing surface	0.820
IR Factor, bottom deployable surfaces	0.400
Spacecraft to Earth Factor, bottom deployable surfaces	0.800^{59}
Spacecraft to Earth Factor, nadir facing surface	1.000
Albedo Factor, nadir facing surface	1.000
Albedo Factor, minus Y deployable bottom surface	0.033
Albedo Factor, plus Y deployable bottom surface	0.001
Albedo Factor, plus and minus X deployable bottom surfaces	0.013

5.2.4 Thermal Validation Metrics

Due to the goal oriented nature of the thermal simulation and direct objective to devise a system capable of maintaining the V3 CMOS within a safe temperature range, the ‘needs’ for the STARE CI thermal model were clearly defined. Explicitly stated, the thermal simulation was employed to design a system capable of maintaining an approximate temperature of 5°C at the imager interface by generating a ~20°C temperature change across a Thermoelectric Cooler (TEC). ‘Accuracy,’ while imperative to both imager and mission success, was difficult to define in terms of the STARE thermal model. In contrast to the STARE structural models which investigated payload responses at laboratory test levels, the thermal model utilized on-orbit loads and environments. Due to the nature of the simulations and an inability to recreate space thermal factors in a test facility, thermal outputs were considered exclusively predictive. Auxiliary to this research, ‘accuracy’ could be achieved if thermistors located at the imager interface indicate on-orbit profiles within the same order of magnitude of those reported in Section 6.

The CII thermal model was utilized to provide a first impression of 3U CubeSat thermal distributions at the extreme $\beta=90^\circ$. These overall results were ‘needed’ for general estimation of internal loads and distributions of temperatures in bus architectures of this form. Again, model ‘accuracy’ could be validated irrespective of the conclusions drawn in this work, if integrated payload thermistors are implemented. It is recommended that accuracy be awarded if the measured minimum and maximum

temperatures for a representative quasi-steady state orbit fall within the predicted simulation range.

5.3 The Low Earth Orbiting Navigation Experiment for Spacecraft Testing

Autonomous Rendezvous and Docking AggieSat4 Structural Model

The AGS4 structural model was largely used to validate the structural integrity of the AGS4 design. The tests performed include static analyses under maximum loading, identification of system natural frequencies, and random vibration simulations at both flight and test levels.

5.3.1 AggieSat4 Computer Aided Design Model

The exterior of the AGS4 structural model was comprised of six machined sheets of Al 6061-T6. The overall dimensions of the model were consistent with the physical AGS4 measurements of 24x24x11 inches in the X, Y, and Z-axes, respectively. The +X, -X, +Y, and -Y panels each featured large cutouts to reduce mass in low stress areas. Four Al 6061-T6 handles were attached to the +Y and -Y simulation panels. These handles were designed for both ground handling as well as on-station ISS maneuverability having been analyzed for both configurations. Two Al 6061-T6 I-beam supports spanned 12in sections along the X-Axis of the bus to increase the overall rigidity of the structure. Both I-beams ran perpendicular to the front (-X) face and were equally spaced from the parallel sidewalls (-Y and +Y). Figure 5.10, below, shows the exteriors of both the AGS4 model and AGS4 simulation model.

In order to reduce the computational complexity required for an accurate solution, several components in the assembly were simplified. The majority of these simplifications alleviated cumbersome component geometries while some simply removed superfluous features. Where simplifications were utilized, components were modeled as simple mass representations to preserve the inertia participation of the component in the assembly. Precautions were taken to uphold bulk material properties throughout the model. Additionally, in cases where high fidelity modeling was required for in-depth studies of troublesome areas, one-to-one models were exported from the as-built AGS4 CAD. Examples of such components included: the Electrical and Power System (EPS) circuit board stack as well as the Computer and Data Handling (CDH) boards.

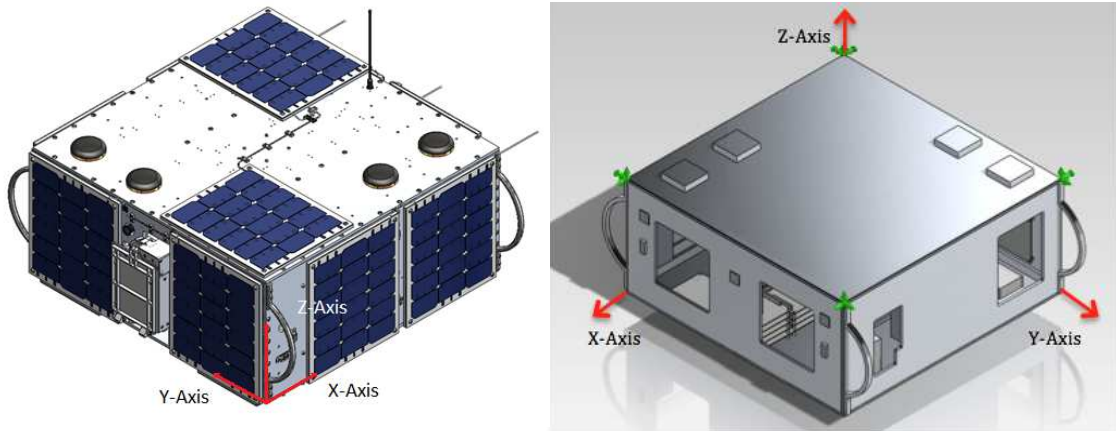


Figure 5.10. Isometric view of AGS4 structure before (left) and after (right) de-featuring with +Z constraints shown

As alluded to above, small non-load bearing components of AGS4 were omitted from the analysis model. These components included: brackets, screws, inhibit switches, harnessing, etc. In order to ensure internal restraints within the satellite, without modeling brackets, SolidWorks mates were applied. Mates imposed a bonded relationship with a no penetration condition at each interface. This modeling constraint allowed adjacent parts to remain physically attached and share nodal points during the meshing process without the additional complexity of bracket geometries.

5.3.2 AggieSat4 Boundary Conditions and Model Constraints

Throughout the AGS4 satellite design and testing processes, the exact flight configuration was still under review by NASA. Still, there was an effort to model AGS4 with boundary conditions that would serve as representative flight restraints. At minimum, the packing configuration was known to include a foam-mold packaging insert and a soft stow duffle bag. Due to material property and linear behavior limitations, the foam packing mold could not be included in the simulation. The effects of the foam were accounted for however with the simulated loading, discussed in the following section.

Because the exact orientation of AGS4 with respect to a launch vehicle reference frame was unknown, an assumption was made that utilized the below AGS4 specific reference frame for the totality of frequency simulations. This assumption meant that in designing the flight packing mold, AGS4 engineers would have sufficient information to orient the spacecraft in the most advantageous, safe, possible configuration. Additional

constraints that need to be considered in the packing mold design are the external features of the AGS4 structure. For example, attached to the outside face of the -Z panel are four Al 6061-T6 feet. The layout is shown in Fig. 5.11. These feet were designed to offset the satellite and its solar cells from the deployment plane of the Cyclops device, a NASA developed launch mechanism.⁶¹ Located at the center of the four-foot configuration is a Cyclops knob offset, to which the Cyclops knob attaches.

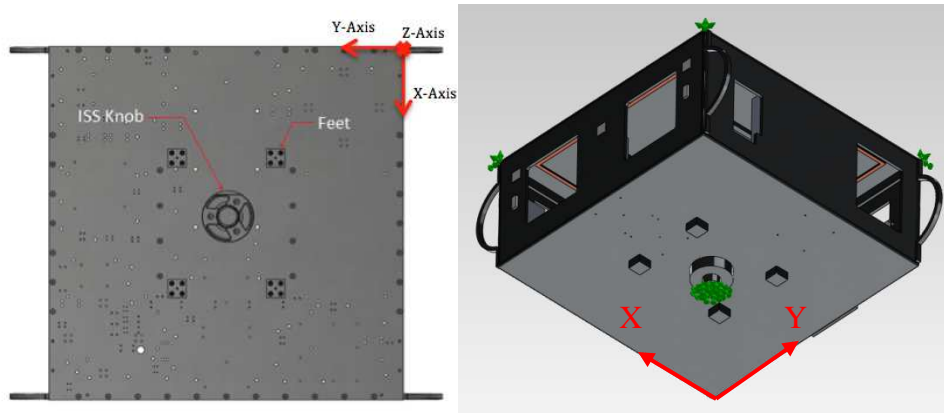


Figure 5.11. Bottom (-Z) panel showing AGS4 feet and Cyclops (ISS) knob (left) and model constraints (right)

The AGS4 analysis model was constrained on the four outer corners of the upper (Z+) panel as well as Cyclops knob, shown above. After elaborate discussion with the AGS4 design team, it was determined that this set of contact locations was the minimum set of contact point necessary to accurately model the foam interface, restrain the bus' motion, and allow enough flexibility to accurately understand the dynamic responses of internal payload components. These portions of the bus were modeled as fixed geometry regions in SolidWorks' simulation package. As previously discussed, for a solid mesh

model, this fixed geometric constraint sets all three translational and all three rotational degrees of freedom to zero. While the fixed geometry surface area was significantly smaller than the anticipated foam/spacecraft interface, these boundary conditions were considered sufficient because of the inherent lack of rigidity such materials were anticipated to impart on the integrated AGS4 bus.

5.3.3 AggieSat4 Simulated Loading

Static testing for the AGS4 model was completed at $\pm 11.6g$ independently in all three axes. This value came from NASA document SSP 50835⁶², which stated that payloads capable of meeting $\pm 11.6g$ loads were deemed safe for flight on the currently supported launch vehicles. According to correspondence with NASA structures subsystem manager, Dr. James Smith, payloads meeting this requirement would additionally be cleared for flight to the ISS.

Due to the effects of the foam-mold packing insert, the random vibration testing environments, prescribed by SpaceX for the Dragon launch vehicle, were attenuated for the simulation. As previously stated, the foam could not be included in the model due to the nonlinear behavior the insert was expected to exhibit. The attenuated PSD values, Fig. 5.12, therefore were meant to capture the damping induced by the foam-mold packing. In order to produce these curves, the pressure per surface area for each of AGS4's six sides was calculated. The pressure exerted on the foam by the weight of AGS4, measured in pounds per square (PSI), drastically impacted the nonlinear behavior

of the foam. In other words, the compression of the foam dictated the packing mold's ability to dampen input PSD values.

After the surface pressure for each face was calculated, tables of scaling factors, based on foam type and compression, were utilized from SSP 50835 to create the attenuated loads the satellite would experience. As can be seen below, both attenuated loads had significantly lower ASD magnitudes at higher frequencies than the Dragon unattenuated profile. The two attenuated loads correspond to a 0.7psi and 0.2psi weight to area ratios of the satellite. Due to the geometry of the AGS4 satellite, the 0.7psi attenuated curve was used for the Z-axis excitations while the 0.2psi curve was used for both the X and Y-axes. Additionally, Fig. 5.12 highlights the foam's physical behavior in that the higher-pressure attenuated curve was less efficient at damping lower frequency excitations than the lower-pressure profile.

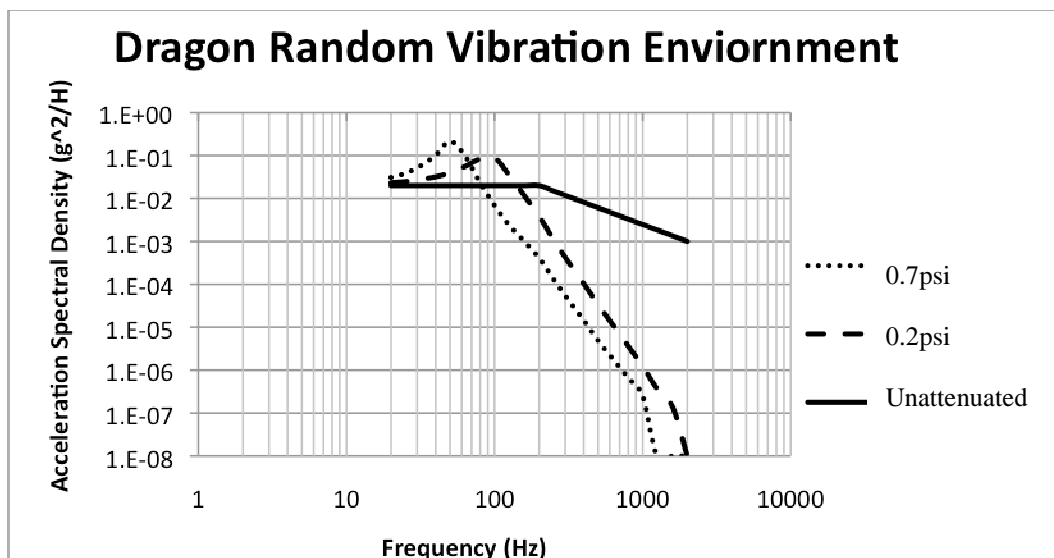


Figure 5.12. Dragon PSD test levels and attenuated profiles as applied in SolidWorks

5.3.4 AggieSat4 Mesh Convergence

After de-featuring the AGS4 model and applying the aforementioned constraints, a convergence check was completed. In order to determine the proper mesh size for the AGS4 structural model, several natural frequency simulations were completed. As a baseline, low mesh densities with fewer nodes were initially run and gradually increased until convergence was determined. Figure 5.13, below, is a plot of the 1st mode natural frequency for the AGS4 model at various node-counts in the mesh.

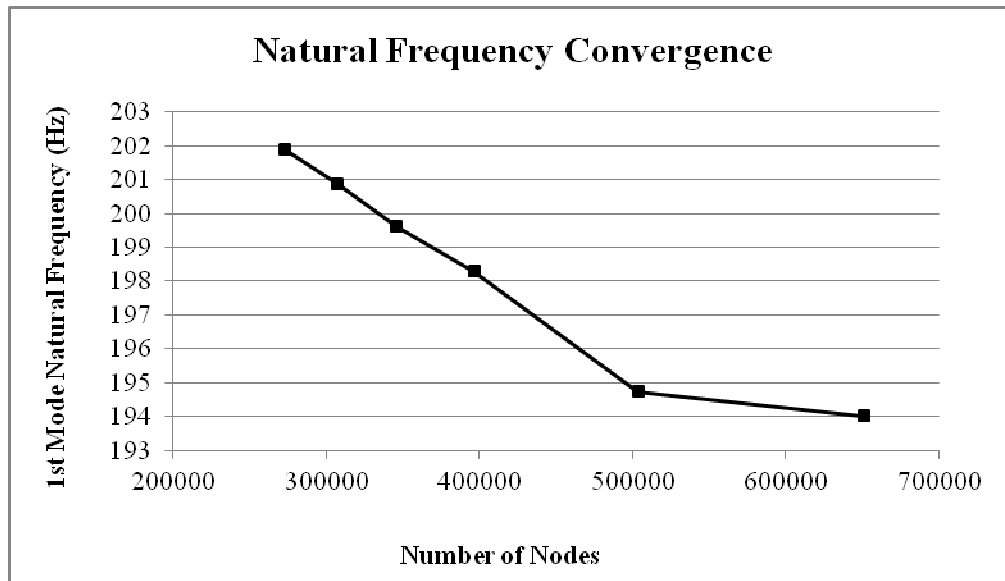


Figure 5.13. AGS4 mesh convergence data

The almost horizontal line in the graph, between the last two node-counts, indicates mesh densities where the solution converged. As can be seen, this convergence began around 500K nodes. For values above 500K, an increase in the number of nodes did not significantly change the results thus a higher mesh density imposed unwarranted

computational complexity. Ultimately, the maximum mesh size chosen was 1.5cm and natural frequency results were assumed accurate to within 1-10Hz.

5.3.5 AggieSat4 Validation Metrics

As briefly addressed in the introduction, payloads of the LONESTAR campaign must adhere to strict manned mission safety standards and have FS. For this reason, the ‘need’ established for the AGS4 simulation model was twofold. Internally, within AGSL, the model was used to predict problematic or unsafe responses of the structure which could potentially lead to mission failure. Externally, NASA had strong interest in ensuring external components would not endanger crew health or safety. For this reason, heightened fidelity simulations were used to evaluate of AGS4 handles and solar cell assemblies.

Due to the fact that, at the time of this research, AGS4 was still in the process of being manufactured, simulation performance will be evaluated following the completion of this work. As a result of an effort to maintain component-level fidelity throughout the AGS4 model, internal simulation results should be held to high ‘accuracy’ standards. Unfortunately, due to the fact that the flight and test configurations of AGS4 include external foam packing material and a NASA issued M0-1 soft stowage bag, results from the simulation may be difficult to correlate with experimental data. Even if accelerometer placements can be secured within the M0-1 bag, external to the foam-packing mold, the simulations’ loads still represent a huge source of uncertainty. Ultimately, the ‘accuracy’ of the AGS4 simulation is largely dependent on how accurate

attenuated loads can capture the physical behavior of foam packing. Without a clear understanding of this uncertainty any proposed validation metric would be arbitrary and irresponsible from a safety perspective. Rather, sensitivity tests with the AGS4 CAD model, following experimental testing, might better help understand which factors most heavily influenced the simulations' results.

5.4 The Low Earth Orbiting Navigation Experiment for Spacecraft Testing

Autonomous Rendezvous and Docking AggieSat2 Model

The model and simulation of AGS2 is presented in this research as historical data. The design, testing, and flight of AGS2 were completed prior to this research. The flight configuration of AGS2 featured a DOD developed deployer, called the Space Shuttle Picosat Launcher (SSPL), which was flown in the cargo bay of the Space Shuttle. Within the SSPL, AGS2 and Bevo-1, a 5x5x5in satellite designed by UT Austin, were secured on an internal rail system between a spring loaded pusher plate and hinged deployer door. The model discussed below did not aid in design decisions or material selections. Rather, the AGS2 model was utilized to assist in the V&V process of laboratory CAD tools.

The complete simulation included two AGS2 models (one was meant to represent the UT spacecraft, Bevo-1) as well as a representative SSPL model. This integrated system was known as DragonSat. Results in Section 6 feature both solo AGS2 structural responses and integrated SSPL responses. The former is presented for research

consistency and comparison with system behavior while the latter was used in the final evaluation of AGS2 validation metrics.

5.4.1 AggieSat2 Computer Aided Design Model

The AGS2 satellite was a 5x5x5in structure with modular, PCB oriented, functional units. The external structure featured six Al 6061-T6 walls. The walls' internal designs included a system of rails that supported two large steel plates. These structural members supported standoffs, ballast blocks, and PCBs from which components were mounted. The steel plates spanned the entire satellite and added mass as well as structural integrity to the otherwise unsupported satellite shell. Figure 5.14 shows the AGS2 flight unit, the as-built CAD mock-up, and the basic structural model.

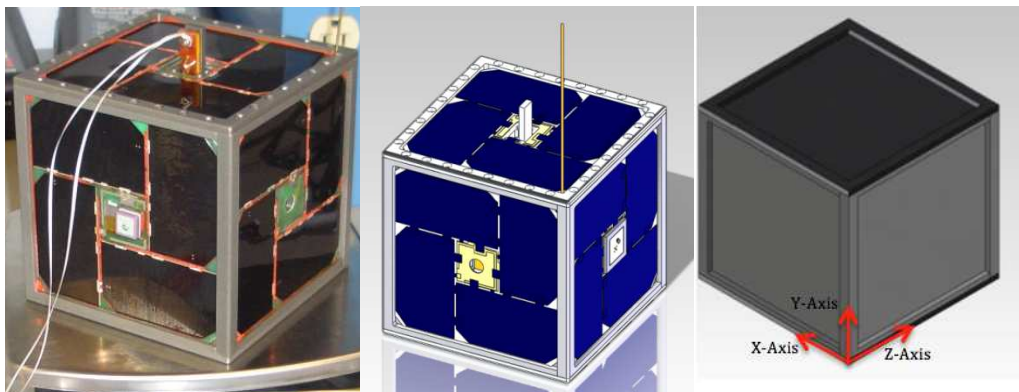


Figure 5.14. AGS2 flight unit (left), full detail CAD model (center), and structural model, de-featured internally and externally (right)

Due to the relatively small size of the AGS2 satellite and thus the inherent decrease in total nodes and computer memory from previously discussed model, de-

featuring was not as heavily required in the creation of this model. For this reason, the flight hardware and simulation model share a remarkable semblance and comparisons between the two differ only in harnessing and small board components. Figure 5.15 shows an interior view of the flight unit along with a screen shot of the simulation model.

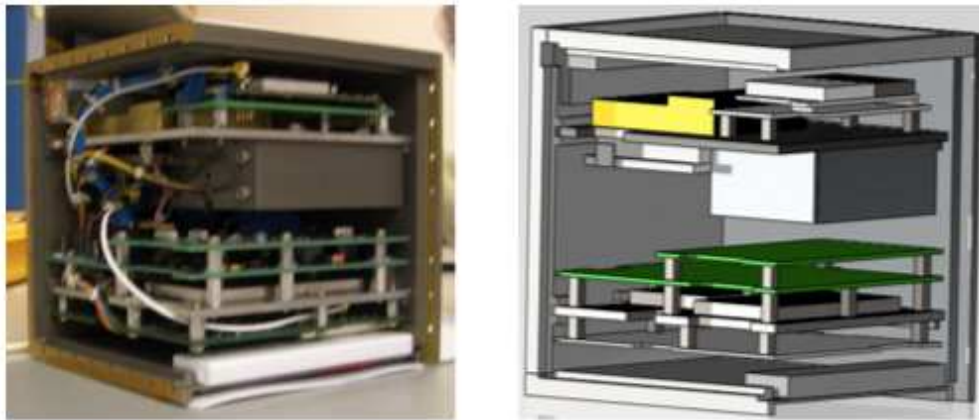


Figure 5.15. Interior of AGS2 flight unit (left) and CAD model (right)

Unfortunately, due to the amount of time that had elapsed between the LONESTAR AGS2 mission and the completion of this research, information on the SSPL design was difficult to obtain. Rather than neglect the launcher and attempt to recreate structural behavior with constraints, as was done in other simulations, a model of the SSPL, albeit crude, was included in the simulation. Unlike the high fidelity of the AGS2 simulation model, the SSPL model was constructed from an Engineering Design Unit (EDU) reverse engineered in-house at AGSL. One of the largest driving factors motivating the inclusion of this model was the available experimental data from the 2009 laboratory testing of DragonSat by NASA JSC. PSD responses from the archived results

were limited to accelerometers placed externally on the SSPL and were impossible to isolate for the AGS2 spacecraft. The SSPL model, which featured five Al 6061-T6 and four internal aluminum tracks, was therefore included in order to provide representative node locations and accurately evaluate the CAD tool. Figure 5.16 shows the in-house SSPL EDU, used to create the simulation CAD, as well as the model itself.

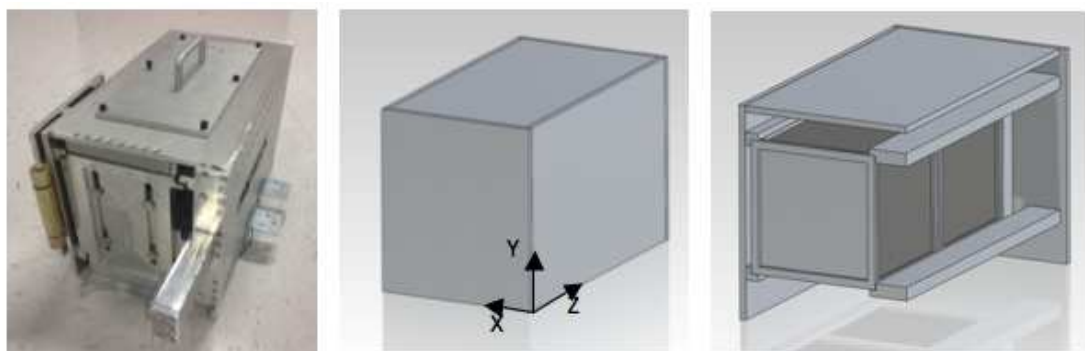


Figure 5.16. SSPL EDU (left) and SSPL CAD model (center, right)

5.4.2 AggieSat2 Boundary Conditions and Model Constraints

As previously mentioned, two separate natural frequency analyses were completed for the AGS2 mission. The first of these analyses was an investigation of the satellites' behavior. For the AGS2 natural frequency simulation, the AGS2 model was constrained with roller slider boundary conditions along the $-X$, $+X$, $-Y$ and $+Y$ faces. These constraints were utilized to allow translational motion of the satellite along the Z -Axis of the SSPL yet restrict motion in the XY plane. For this reason, the first natural frequency mode was purely translational and provided nonsensical values.

In the simulation of the SSPL natural frequency, the model was restrained with a fixed geometry condition along the bottom planes of each of the four SSPL sidewalls. These constraints mimicked the interface of the SSPL model with the shaker table. Additionally, a 700lbf load was applied to the +Z face of the pusher plate to simulate the system's rigidity had the physical pre-loaded deployment spring been included.

5.4.3 AggieSat2 Simulated Loading

The loads utilized in the AGS2 simulation were the exact PSD curves inputted into the NASA shaker table in 2009. As can be seen, the X-Axis was subjected to a load of 6.775_{gRMS}, the Y-axis a load of 8.560_{gRMS}, and the Z-Axis a 7.752_{gRMS} load. These values represent the maximum expected load for the DragonSat payload onboard the Space Shuttle Endeavour. The loads as applied in SolidWorks are shown below in Fig. 5.17.

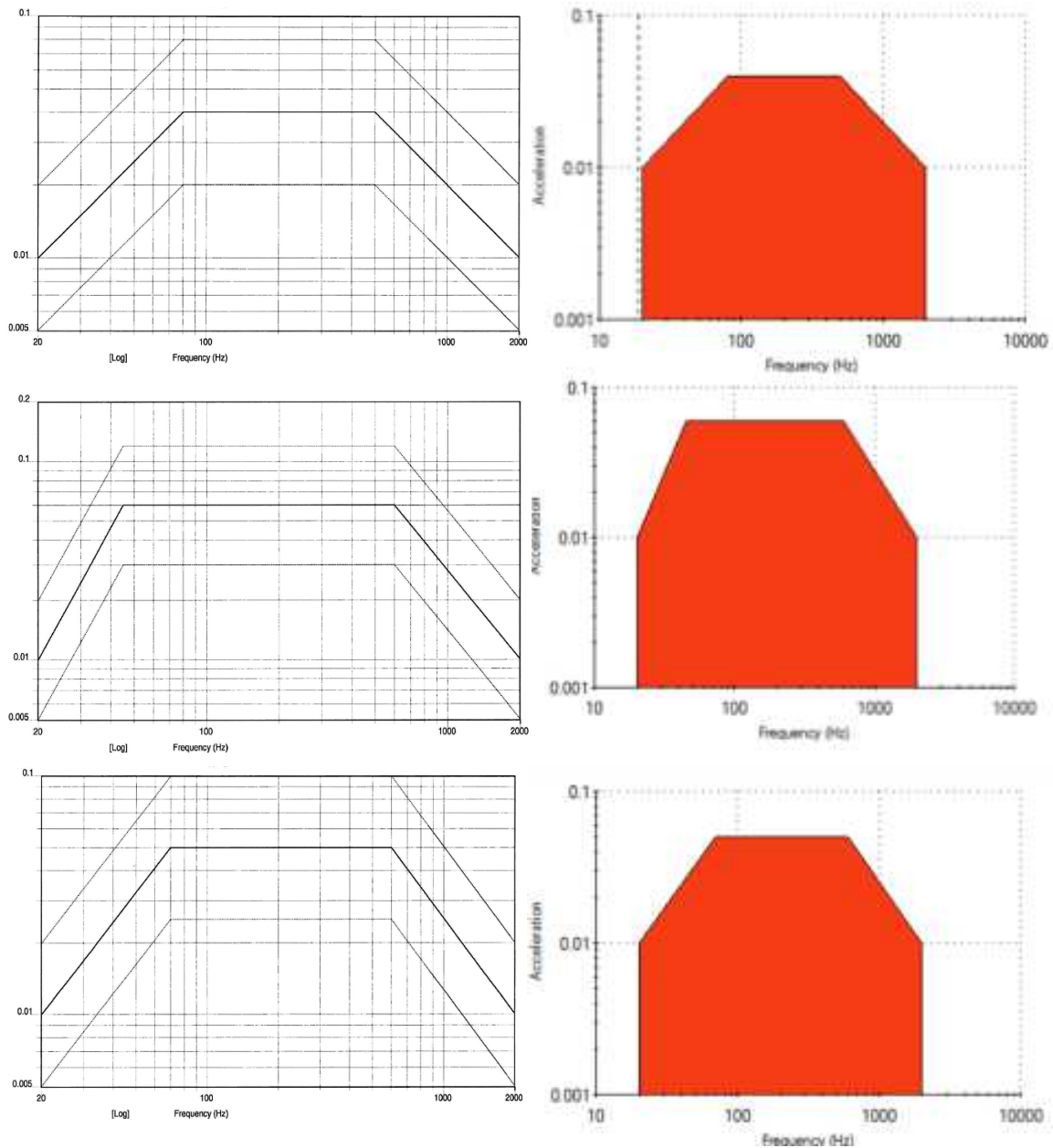


Figure 5.17. DragonSat X-Axis (top), Y-Axis (center), and Z-Axis (bottom) test level profile as applied in SolidWorks

5.4.4 AggieSat2 Mesh Convergence

As in the previously discussed simulations, convergence for the AGS2 mission was completed in order to determine an adequate mesh density for the model. The

results presented in this section highlight the convergence studies of both the integrated DragonSat system, Fig. 5.18, as well as the individual AGS2 model, Fig. 5.19.

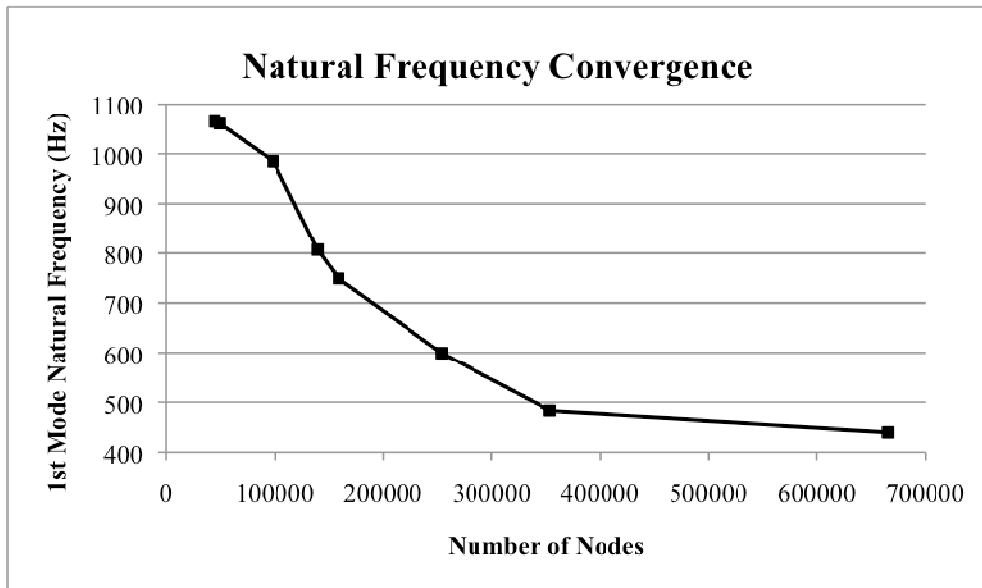


Figure 5.18. DragonSat mesh convergence data

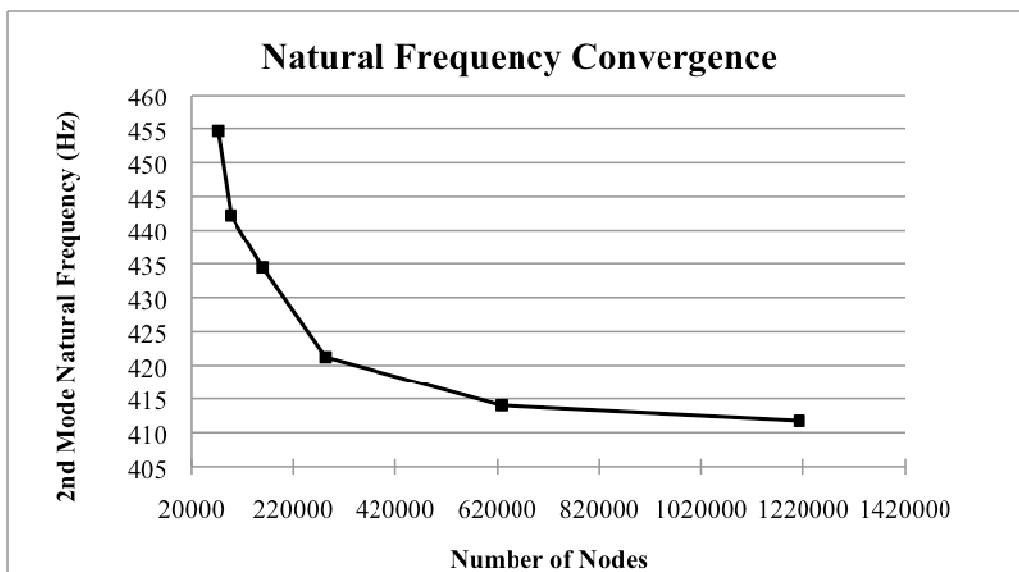


Figure 5.19. AGS2 mesh convergence data

When comparing the two models' convergences it is interesting to note that both converge around 400Hz. This suggests that the structural response of the AGS2 model strongly influenced the frequencies at which the SSPL model resonated. Such behavior is to be expected especially when the first five modes of each model showed internal board displacements.

The SSPL model showed convergence around 670K nodes. Simulations utilized a 0.5mm maximum element size and had approximately 400K elements. Higher mesh densities may have produced slightly more converged results but given the crude nature of the SSPL model this would not have contributed to the overall accuracy of the result. The independent AGS2 simulation converged to within 1% at approximately 630K nodes. This mesh was created using a maximum element size of 2.5mm. As previously stated, the first mode natural frequency response demonstrated pure translation. The second mode however was found to be around 410Hz. This value is vastly different than the 1900Hz natural frequency originally reported for the 2009 AGS2 simulation model. The historic model however featured only the two internal steel plates and six exterior Al 6061-T6 walls. Moreover, due to both computational and hardware limitations, the 2009 analysis only featured 140K nodes.

5.4.5 AggieSat2 Validation Metrics

The decision to use an SSPL model was based off a program-specific simulation need: to replicate, with as much accuracy as possible, historical experimental data. Due to the fact that the simulation of AGS2 for this research followed the completion of the

mission, the work was regarded as completely investigative. For this reason ‘accuracy’ standards were made purposefully rigorous to push the limits of the CAD tool. The following metrics therefore reflect the expectation that the AGS2 model was easily the most complete model investigated. For the DragonSat model, simulation accuracy was defined as resonant frequencies within $\pm 100\text{Hz}$ of experimental data.

6. RESULTS

All results presented in this section were achieved through the use of the converged mesh sized previously described for each of the respective models. Experimental data were included in these results, where available. All experimental payload testing was completed externally to this research and results borrowed from third party investigators. In the interest of conciseness, only one of the first five natural frequency modes is pictured below. When available, additional mode shapes are displayed in the Appendix.

6.1 Version 2 Structural Results

These analyses utilized the converged maximum mesh size of 4mm, discussed above, to achieve the following results.

6.1.1 Version 2 Natural Frequency

Table 6.1 summarizes the results of the LLNL V2 natural frequency investigation.

Table 6.1: LLNL V2 Natural Frequency of First Five Modes

Mode No.	Frequency (Hz)
1	1114.1
2	1141.2
3	1157.9
4	1286.6
5	1376.7

For the LLNL V2 payload, the fourth mode was the one resonance that occurred showing both external, as well as internal, deformations. All other mode shapes were purely internal. For this reason, and due to the previously discussed proprietary nature of the research, only a figure of the fourth mode shape, for the LLNL V2 payload, is presented with these finding.

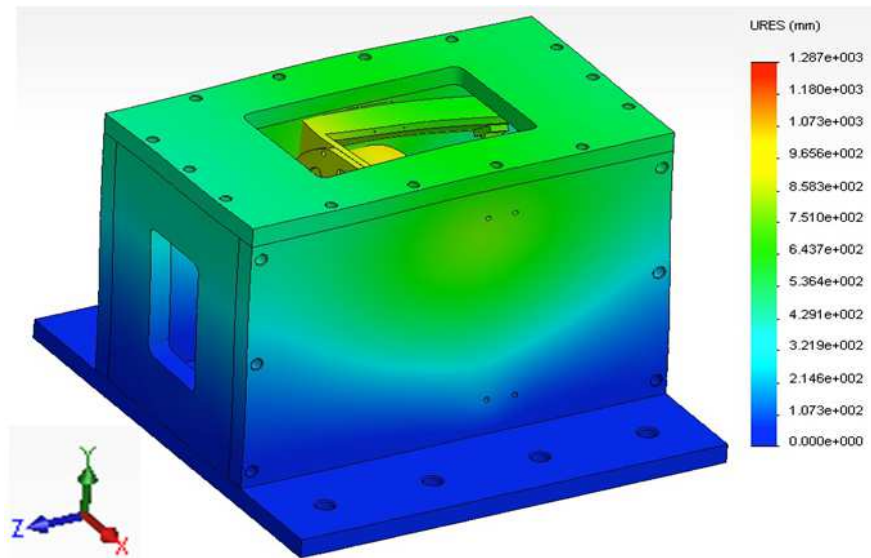


Figure 6.1. LLNL V2 4th mode natural frequency

The following descriptions attempt to capture the additional four modal responses of the LLNL V2 payload in the absence of visual data. The first natural frequency mode corresponded to deformation of the primary payload base plate in the Z-Axis. The second and third natural frequency mode showed rotation of the entire payload module about the Y-Axis and X-Axis, respectively. For each of these modes, the rotation pivoted about the aforementioned base plate where the payload was anchored. The fourth mode, shown in Fig. 6.1, demonstrated payload frame rotation about the X-Axis, payload rotation about the Y-Axis and test pod vibration in the X-Axis. Lastly, the fifth mode of the LLNL V2 natural frequency showed support frame rotation about the X-Axis with the highest observed displacements occurring in the secondary mirror assembly.

6.1.2 Version 2 Random Vibration (X-Axis)

The results from the random vibration simulations and experimental testing for the X-Axis of the LLNL V2 payload are shown below. The PSD curves presented in Section 5 were inputted as shown and represented a 0dB case. The below result graphs, Fig. 6.4, highlight the frequencies that most contribute to the bus' peak accelerations. Additionally, Figs. 6.2 and 6.3 show accelerometer placements on the V2 payload as well as the corresponding simulation probe locations. Table 6.2 below correlates the probed response locations from the model to the accelerometer locations of the physical test.

Table 6.2: LLNL V2 Probed Locations for X-Axis PSD Response

Node	Accelerometer
366168	A
349643	B
291129	C
291209	D

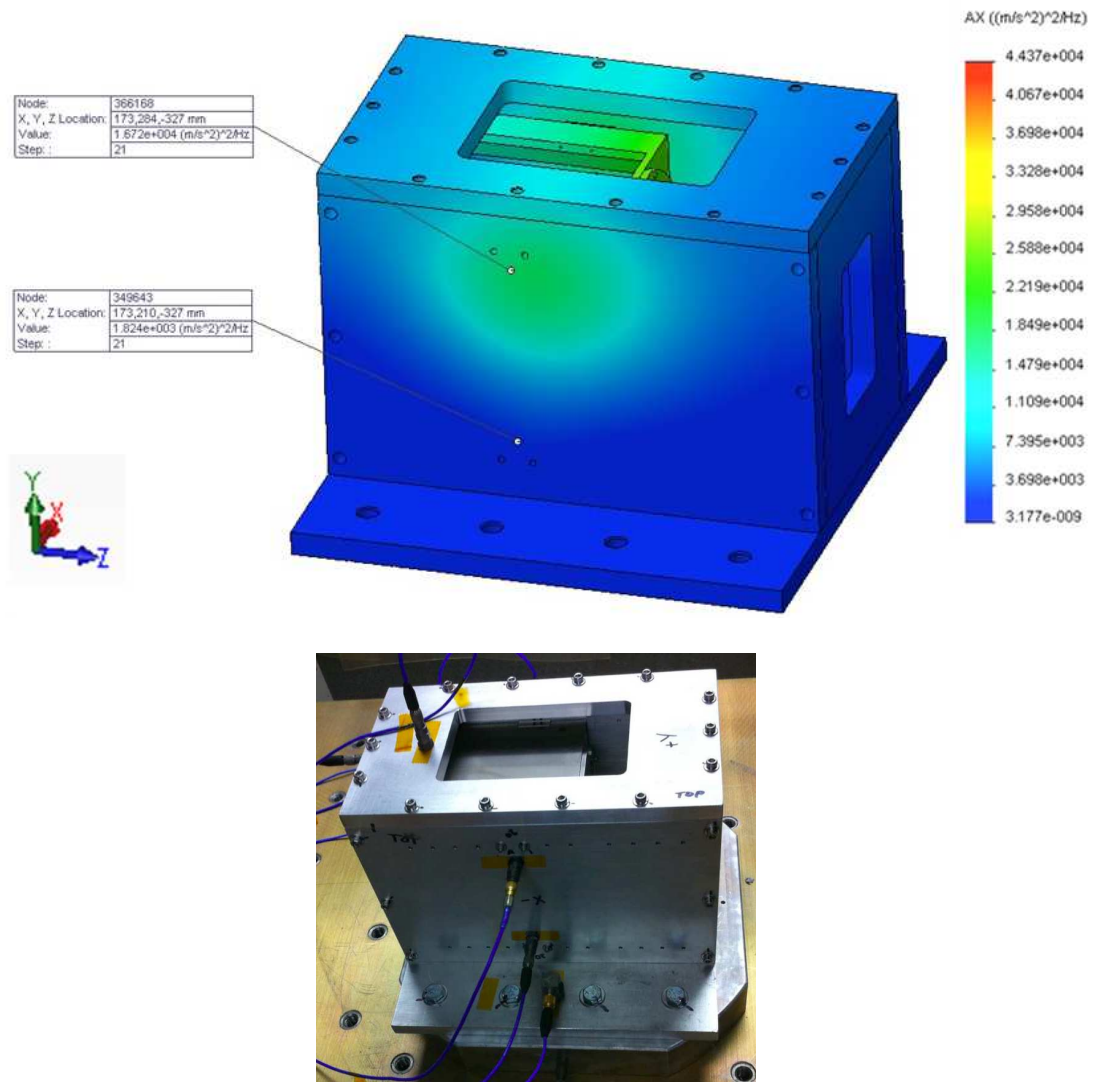


Figure 6.2. LLNL V2 -X Face: PSD probe locations (top) and physical test pod model with accelerometers (bottom)

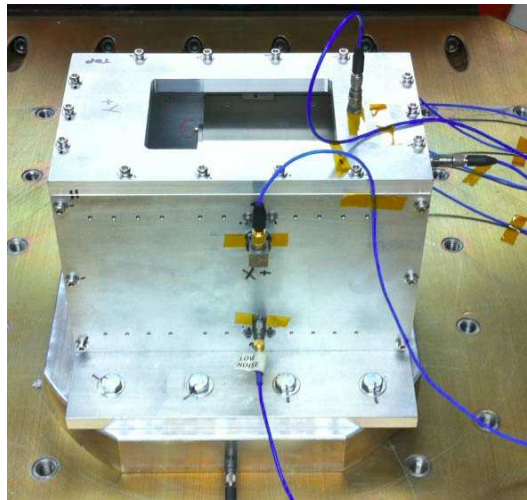
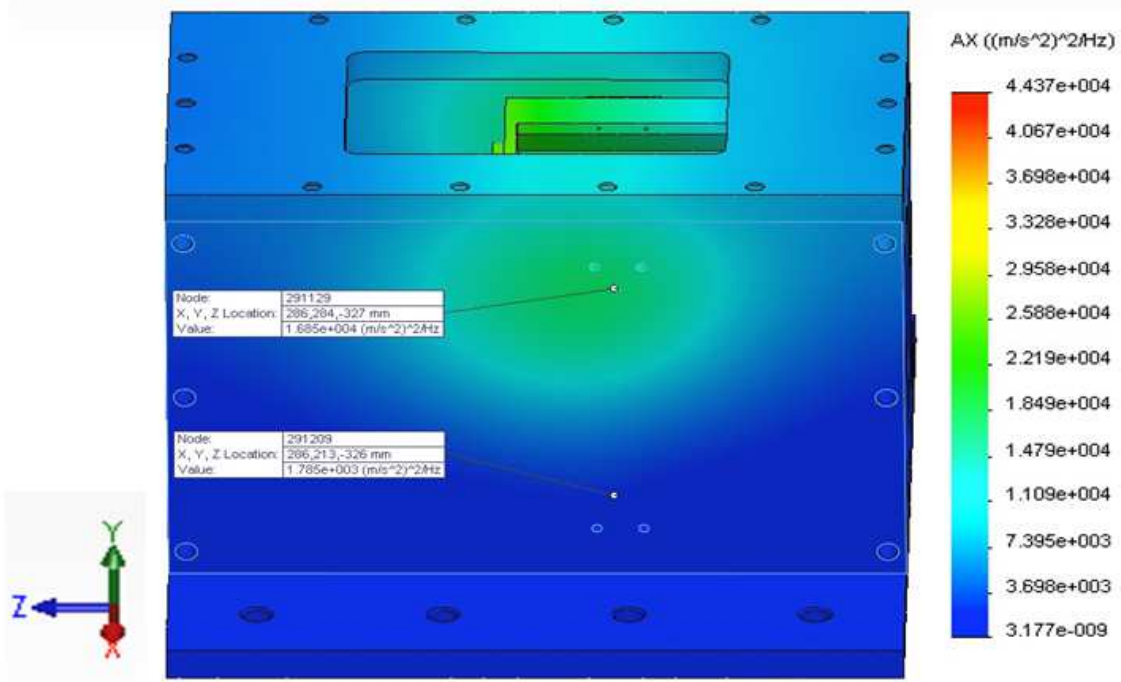


Figure 6.3. LLNL V2 +X Face: PSD probe locations (top) and physical test pod model with accelerometers (bottom)

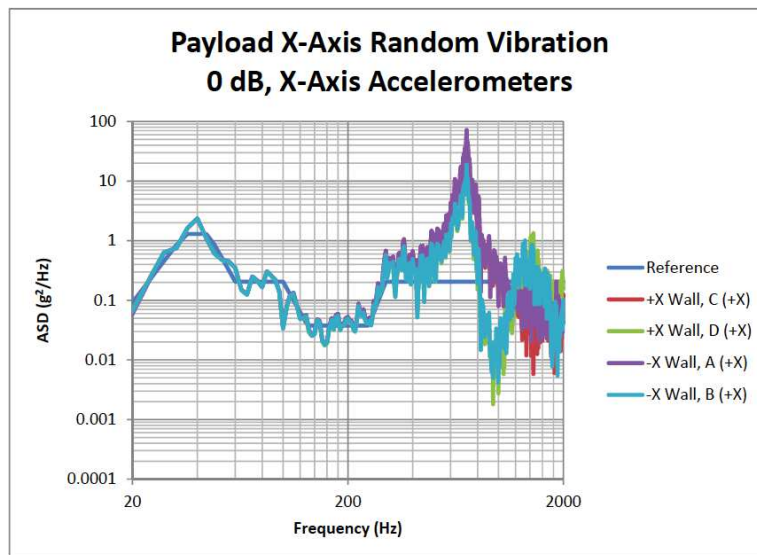
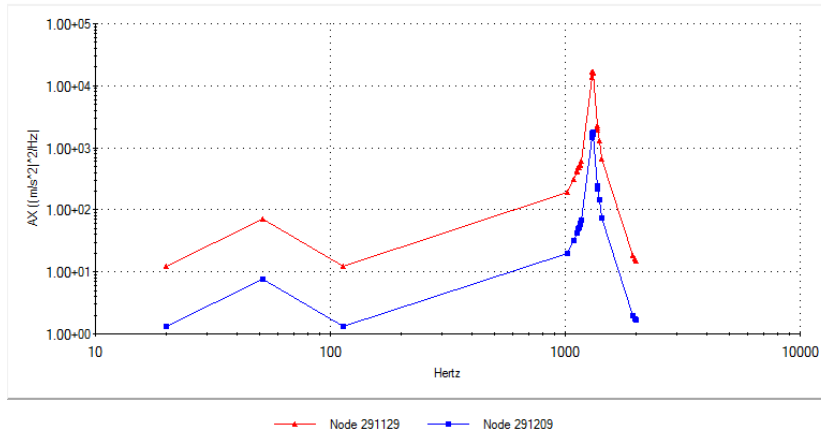
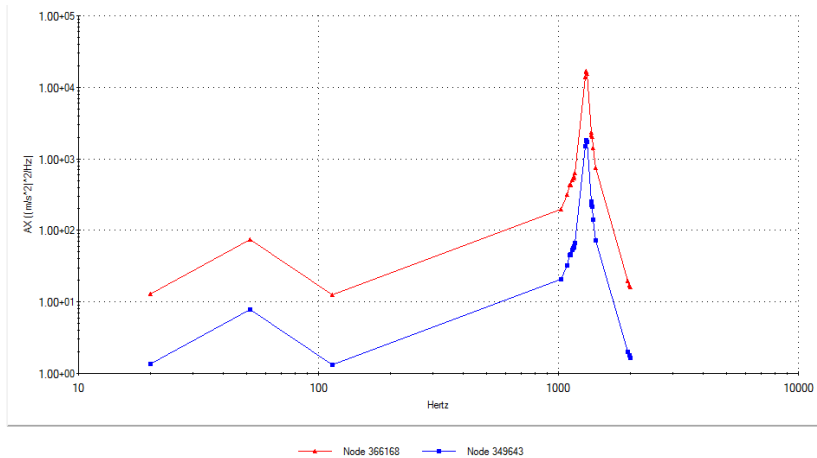


Figure 6.4. LLNL V2 PSD response for X-Axis excitation

6.1.3 Version 2 Random Vibration (Y-Axis)

The results from the random vibration simulations and experimental testing, with probe locations and accelerometer placements shown in Fig. 6.5, for the Y-Axis of the LLNL V2 payload are shown below in Fig. 6.6. As in the X-Axis simulation, the PSD curves presented in Section 5 were inputted as shown and represented a 0dB case.

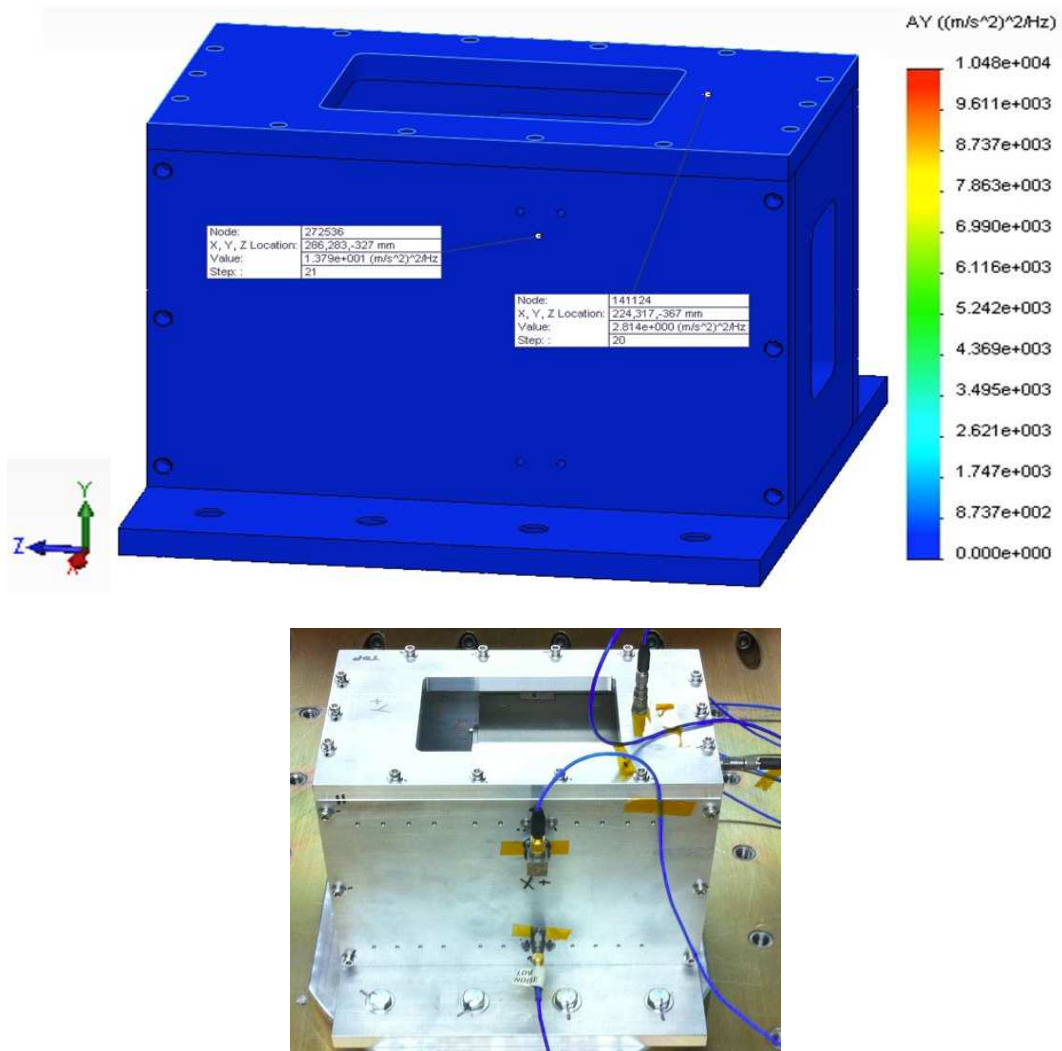


Figure 6.5. LLNL V2 PSD probe locations (top) and physical test pod model with accelerometers (bottom)

Table 6.3: LLNL V2 Probed Locations for Y-Axis PSD Response

Node	Accelerometer
272536	+X Wall
141124	+Y Wall

Table 6.3 above correlates the probed response locations from the model to the accelerometer locations of the physical test. Results of both are shown below.

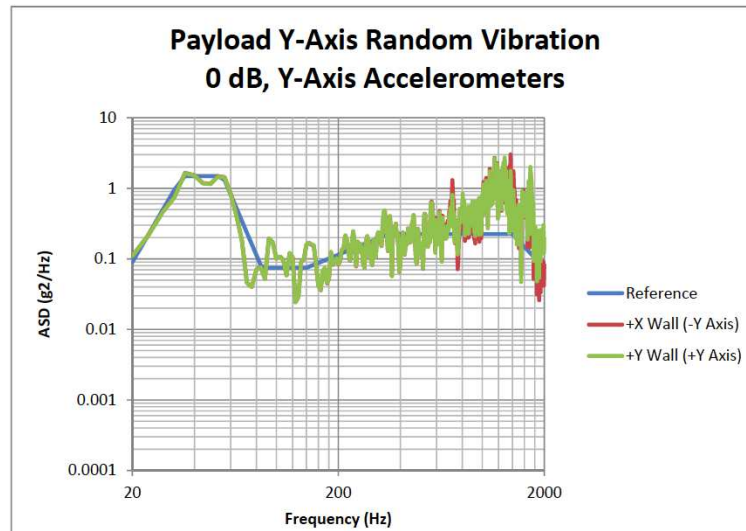
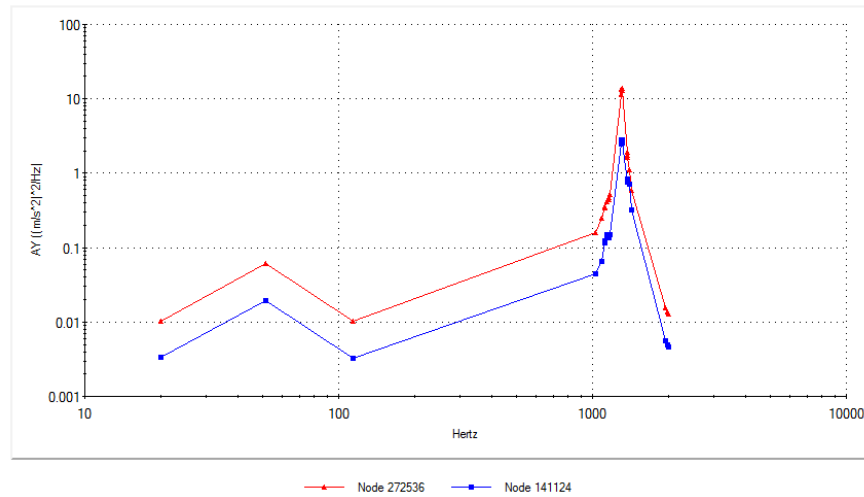


Figure 6.6. LLNL V2 PSD response for Y-Axis excitation

6.1.4 Version 2 Random Vibration (Z-Axis)

The results from the random vibration simulations and experimental testing for the Z-Axis of the LLNL V2 payload are shown below. As in the previous two simulations, the PSD curves presented in Section 5 were inputted as shown and represented a 0dB case. Figure 6.7 shows the nodes probed for this analysis.

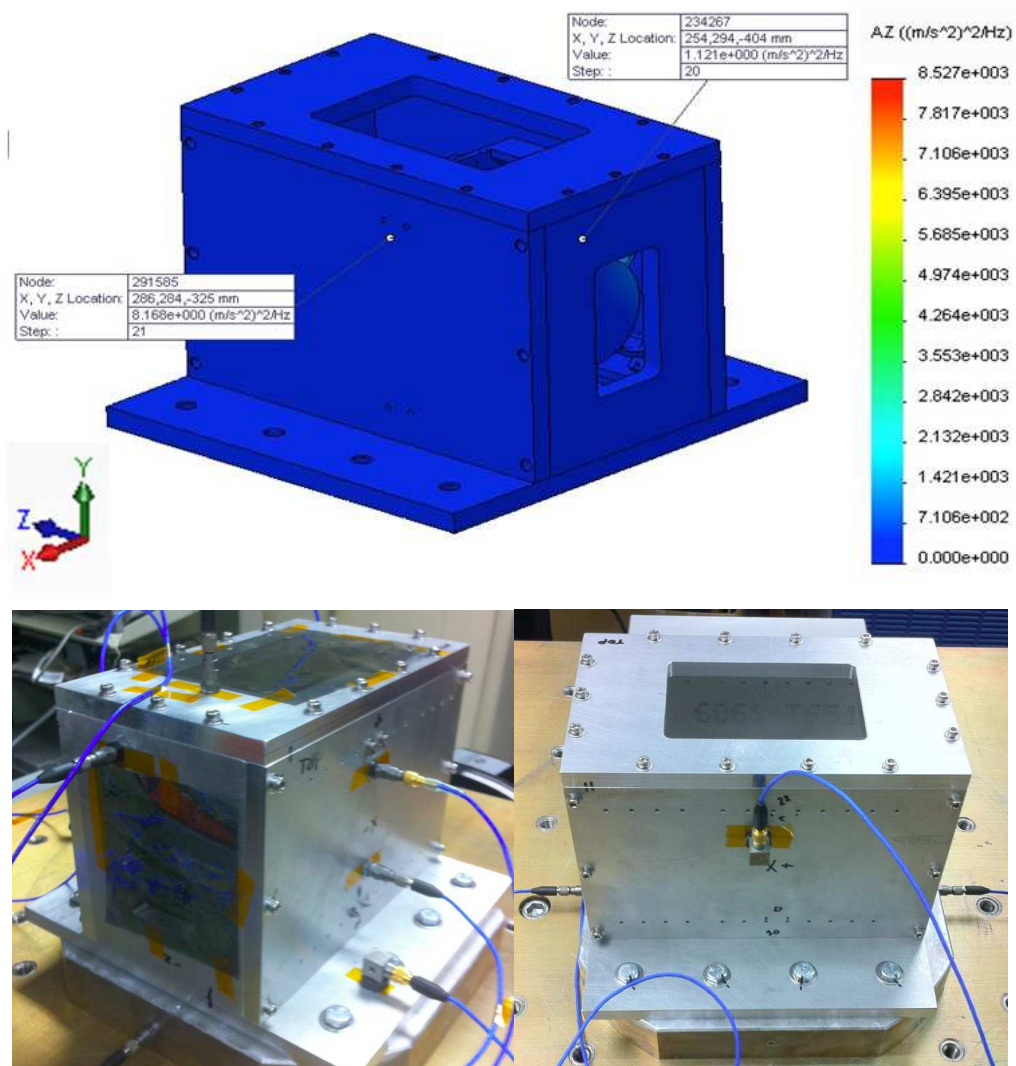


Figure 6.7. LLNL V2 PSD probe locations (top) and +X/-Z faces of the physical test pod model with accelerometers (bottom)

Table 6.4: LLNL V2 Probed Locations for Z-Axis PSD Response

Node	Accelerometer
234267	+X Wall
291585	-Z Wall

Table 6.4 correlates the probed response locations from the model to the accelerometer locations of the physical test. Results of both are shown below, see Fig. 6.8.

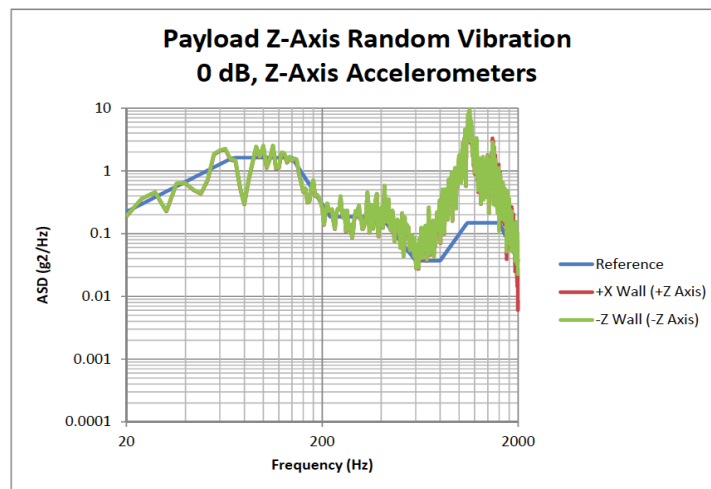
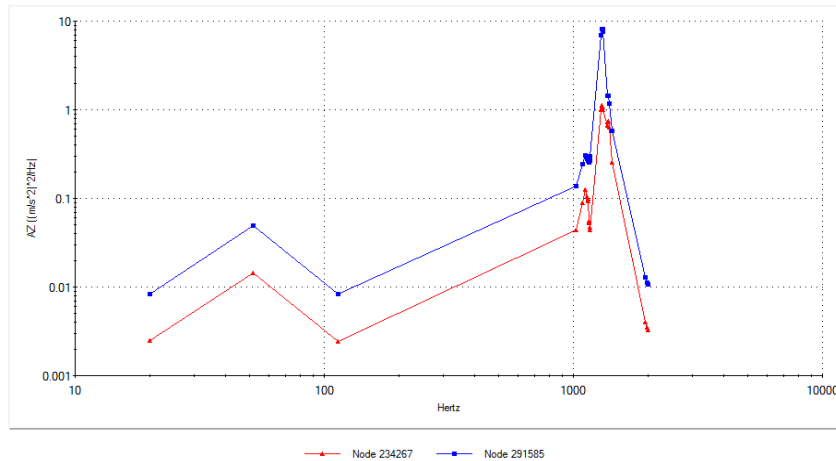


Figure 6.8. LLNL V2 PSD response for Z-Axis excitation

6.2 Version 3 Structural Results

These LLNL V3 analyses utilized the converged maximum mesh size of 2.3mm. As previously discussed, the entire bottom plate of the test pod was restrained, which isolated the payload responses.

6.2.1 Version 3 Natural Frequency

Below, Table 6.5 highlights the first five frequencies at which the LLNL V3 payload resonates. Based on the natural frequency results, the imager was predicted to experience resonant responses between 1440Hz and 1940Hz.

Table 6.5: LLNL V3 Natural Frequency of First Five Modes

Mode No.	Frequency (Hz)
1	1454.1
2	1553.5
3	1724.3
4	1791.1
5	1930.3

As was the case for the LLNL V2 payload, only one of the five natural frequency modes exhibited both external and internal deformations. This mode was the first natural frequency resonance and is displayed in Fig. 6.9. By observation, the other five modes exhibited the following behaviors: the second and fifth modes showed primary displacements in the Z-Axis direction, the third mode in the X-Axis direction, and the fourth mode in the Y-Axis direction. More specifically, the third mode showed the primary payload plate flexing in the Z-Axis direction. The third mode also demonstrated

rotation of the imager board assembly about the Y-Axis, while the fourth mode demonstrated rotation about the X-Axis. Lastly, the fifth natural frequency mode shape highlighted the response of the about the entire payload in rotation X-Axis.

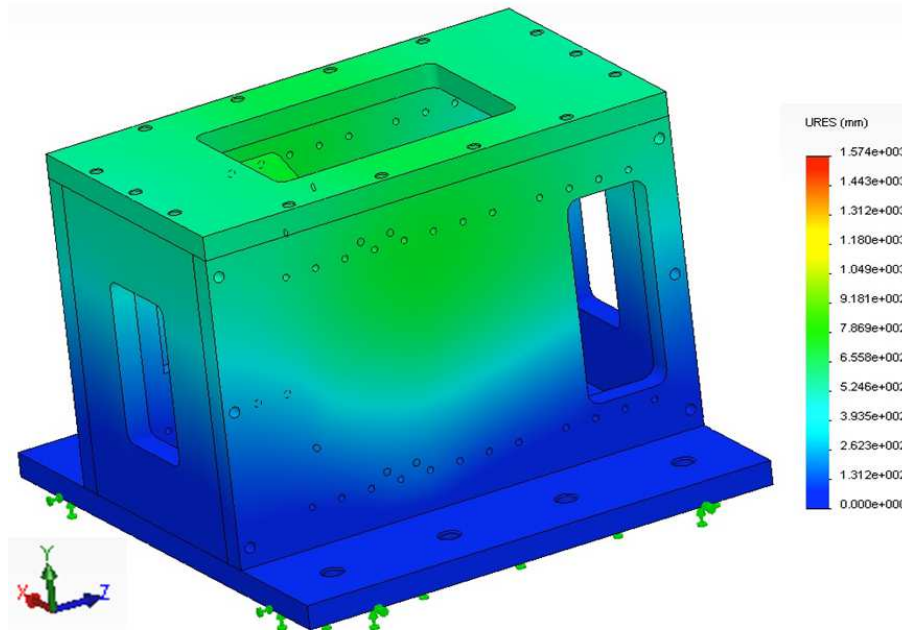


Figure 6.9. LLNL V3 1st mode natural frequency

Dynamic frequency results were conducted with the same mesh density as the natural frequency analysis. Dynamic frequency results were all measured at the locations shown in Fig. 6.10 to capture representative accelerometer locations. The responses reported below are resultant acceleration values, rather than axis specific accelerations, as were utilized in the V2 analysis. The decision to probe for total acceleration as well as the PSD probe locations chosen were both driven by a lack of information regarding accelerometer placement location at the time of the simulation.

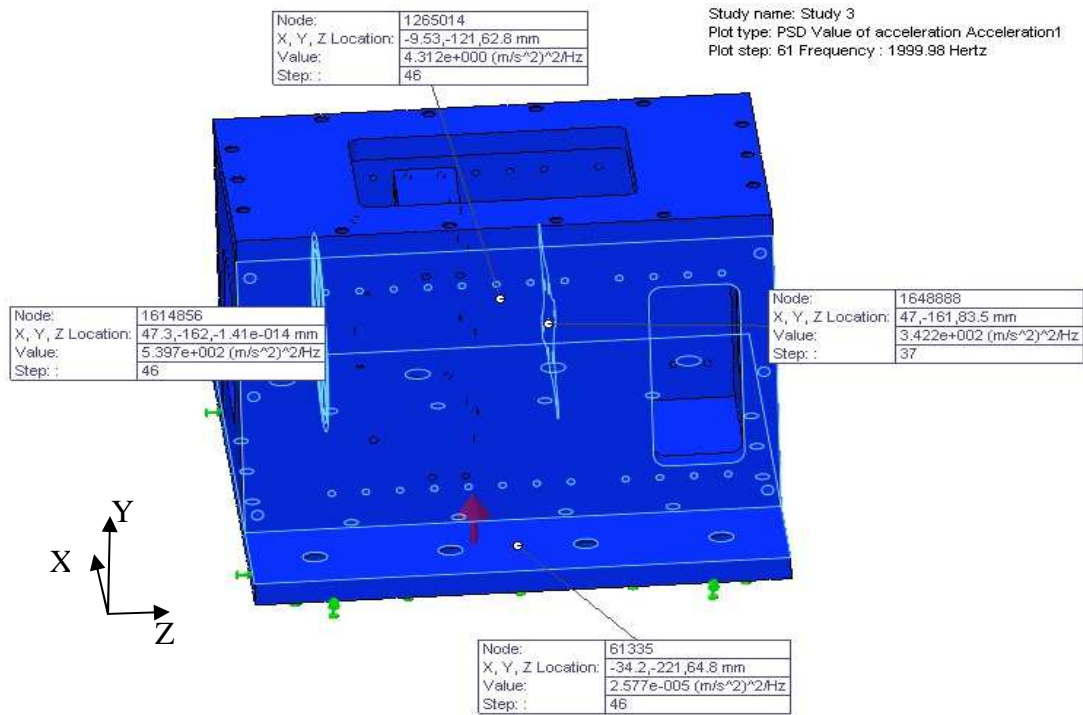


Figure 6.10. LLNL V3 PSD probe locations

6.2.2 Version 3 Random Vibration (X-Axis)

In addition to the PSD curves reported for the V2 analysis, the V3 analysis also includes RMS values for probed locations. The RMS values reported are the results of SolidWorks' efforts to fit the structural responses of the bus to a uniform bell distribution. By default, the software reports the 1σ response. From probability theory, it is expected that accelerations for these locations will fall between $\pm 1\sigma$, 66% of the time.

The X-axis response, Fig. 6.11, peaks just above 1200Hz over a bandwidth peak of 800-1600Hz. This response did not directly correspond to any of the above modes in particular, but would encompass Modes 1 and 2. Mode 1, specifically, featured high imager plate deformations in the X-Axis direction. The peak RMS value for the above

set of sampled points was 63g. This value was observed on an internal payload baffle set. The imager plate and wall reached RMS values of 53g and 45g, respectively.

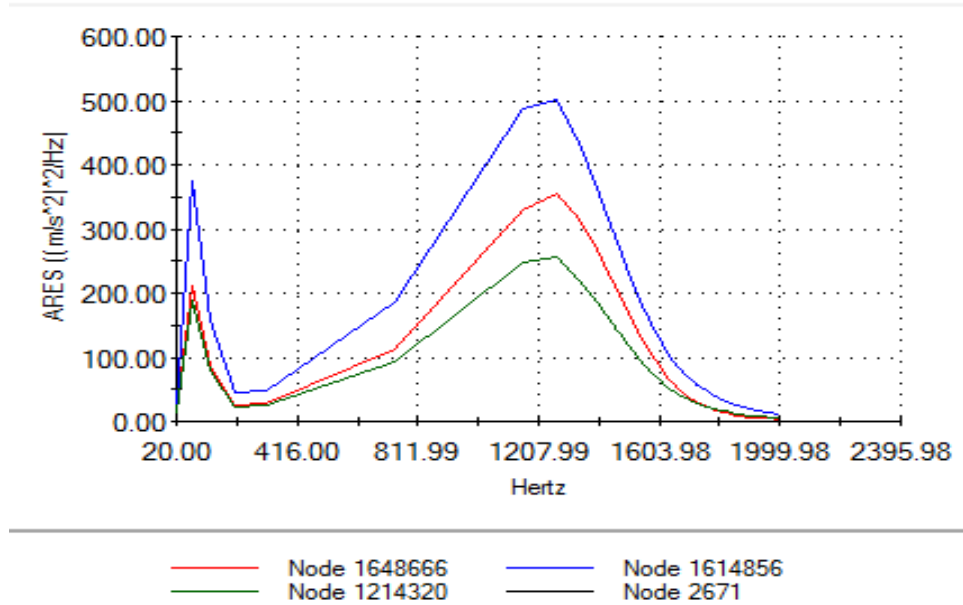


Figure 6.11. LLNL V3 PSD response for X-Axis excitation

The responses shown above can be related to physical locations within the payload on the exterior of the test pod with the information presented in Table 6.6.

Table 6.6: LLNL V3 Probed Locations for X-Axis PSD Response

Location	Node
Baffle Center	1644856
Imager Plate	1648666
X Wall	1214320
Base Plate	2671

6.2.3 Version 3 Random Vibration (Y-Axis)

The random vibration responses for the Y-Axis excitation are overviewed below. As can be seen in the Y-Axis random vibration response, Fig. 6.12, there was a PSD response peak at roughly 1800Hz. Both the magnitude and payload components which exhibit high deformation mirror responses seen in Modes 4 and 5. Peak RMS g-loading among the sampled points was 68g at the baffle set location. The imager plate and wall reached RMS values of 56g and 5g, respectively. Again, the default RMS value reported in SolidWorks corresponds to 1σ values and is therefore a good indicator of average payload behavior.

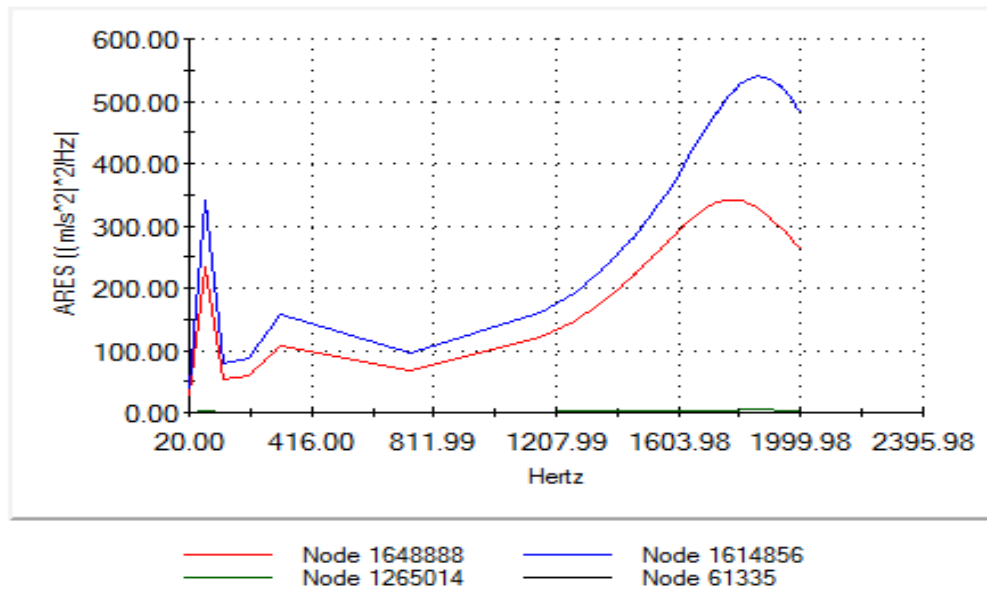


Figure 6.12. LLNL V3 PSD response for Y-Axis excitation

The node locations shown in Fig. 6.12 correspond to simulation locations listed in Table 6.7.

Table 6.7: LLNL V3 Probed Locations for Y-Axis PSD Response

Location	Node
Baffle Center	1614856
Imager Plate	1648888
X Wall	1265014
Base Plate	61335

6.2.4 Version 3 Random Vibration (Z-Axis)

Finally, the Z axis response shown in Fig. 6.13, peaked near 1500Hz. The largest physical response was seen at the imager plate, and corresponded well to the behavior observed in Mode 2. Both the second mode and the Z-Axis random vibration responses featured large Z axis movement of the imager plate at ~1500Hz. Peak RMS values for the sampled points was 61g at the imager plate. The baffle set and wall locations reached RMS values of 13g and 3g, respectively.

Table 6.8: LLNL V3 Probed Locations for Z-Axis PSD Response

Location	Node
Baffle Center	1615154
Imager Plate	1648547
X Wall	464305
Base Plate	69868

Table 6.8 lists nodal locations for the following responses.

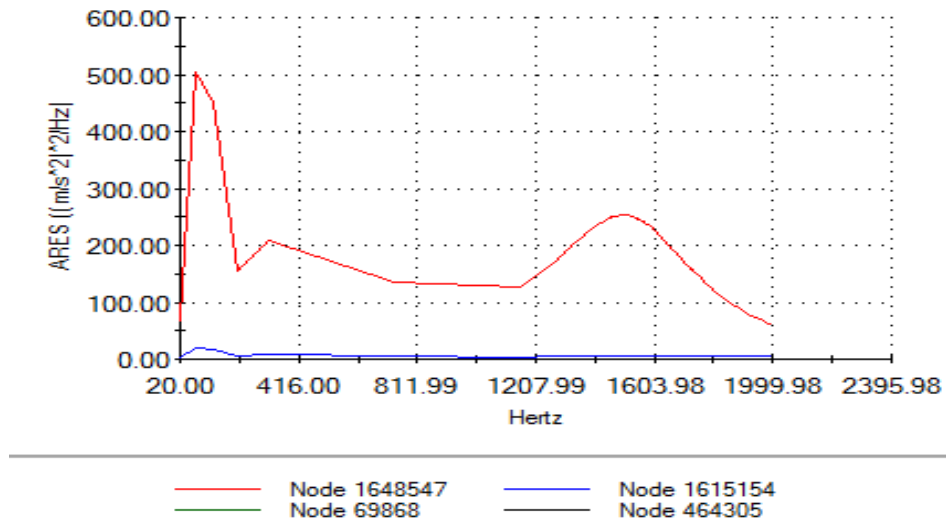


Figure 6.13. LLNL V3 PSD response for Z-Axis excitation

6.3 Colony I Thermal Results

This section highlights noteworthy results of the LLNL CI thermal investigation. Both the transient and steady state thermal investigations aimed at locating candidate thermal strap locations. For each of these simulations the locations considered are shown in Fig. 6.14.

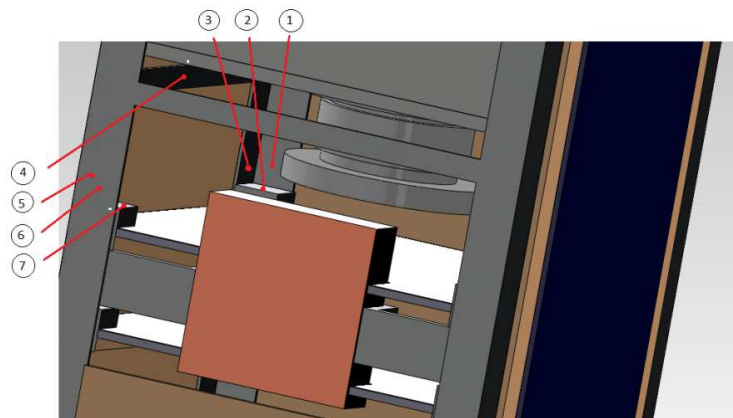


Figure 6.14. Heat strap potential mounting locations

6.3.1 Colony I $\beta=0^\circ$ Case

The results of the transient simulation are shown in Fig. 6.15 and tabulated temperature averages are displayed in Table 6.9. As can be seen, the electronics board reached approximately 25°C. Also, the gradient on the antenna side PCB had magnitudes ranging from 5°C to 220°C. Based on the programmatic design specifications, this was deemed an infeasible location for thermal strap interfaces. The two side panels (Faces 7 and 9) however have minimums as low as -5°C. These temperatures are ideal for sinking heat away from the proposed thermal straps and likewise the heat positive side of the PEC.

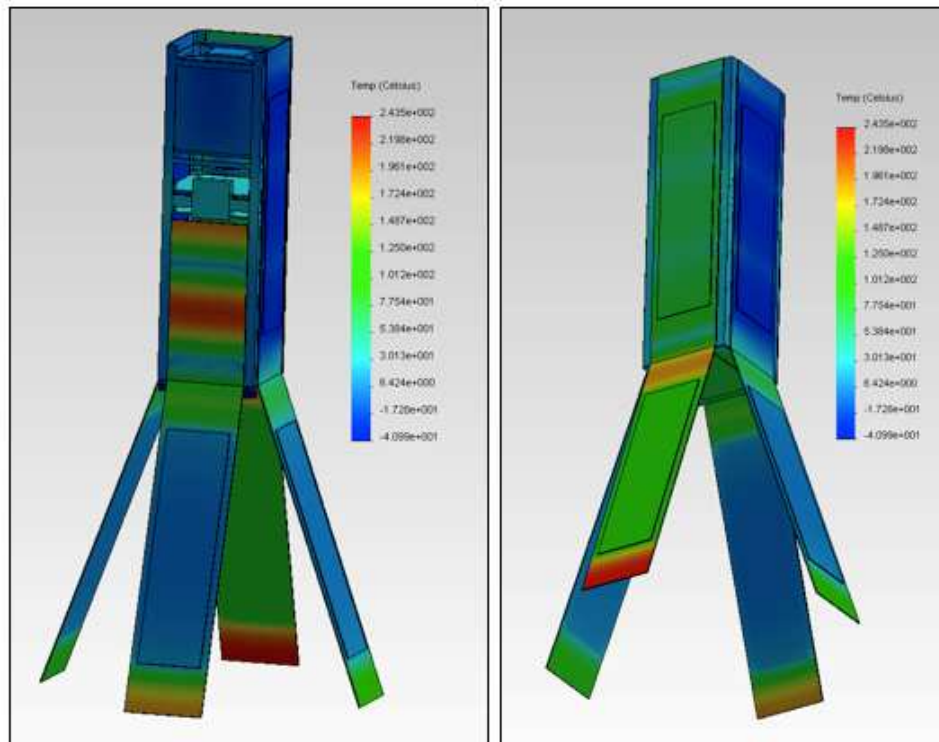


Figure 6.15. LLNL CI Transient thermal results

Table 6.9 LLNL CI Transient Average Temperatures

Location	Node	Description	Average Temperature
1	14885	+Y frame corner	25.0°C
2	16433	+Y electronics mount	25.0°C
3	14118	+YX frame corner	25.0°C
4	9644	X wall frame	-10.0°C
5	14365	-YX frame corner	25.0°C
6	10628	-Y frame corner	25.0°C
7	16487	-Y electronics mount	25.0°C

Below, Fig. 6.16 shows the transient response of interface location possibilities over the duration of three orbits. As can be seen, the satellite temperature results begin to converge in the last orbit, yet does not actually reach steady states during the time allotted for this investigation. Had either the mesh size of the thermal model or the length of the time step been increased, additional computation resources may have been available for a more refined solution.

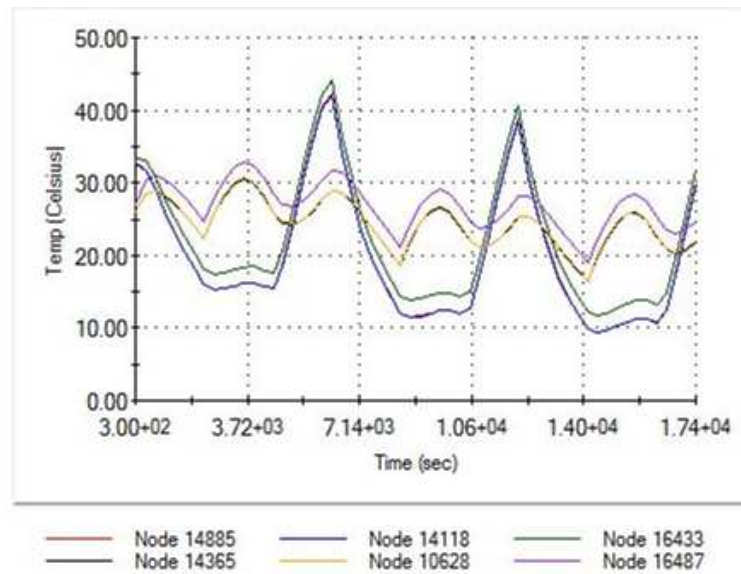


Figure 6.16. LLNL CI Transient response of primary interface locations

It is also important to note that while all the temperatures with the exception of location 4, Fig. 6.17, average about 25°C during this period, only locations 5-7 are particularly stable. These locations only oscillate approximately +/-5°C, while locations 1-3 oscillate as much as +/-15°C. In addition to the transient response of location 4, Fig. 6.17 also depicts the response of four supplementary X face and frame locations. Node 9728 and 9484 are near the corners of the frame/wall, while node 9644 is in the center. In this transient analysis, the X walls are perpendicular to the sun for the given orientations. The center of the wall, at Node 9644, therefore has the maximum heat rejecting capacity of all probed locations.

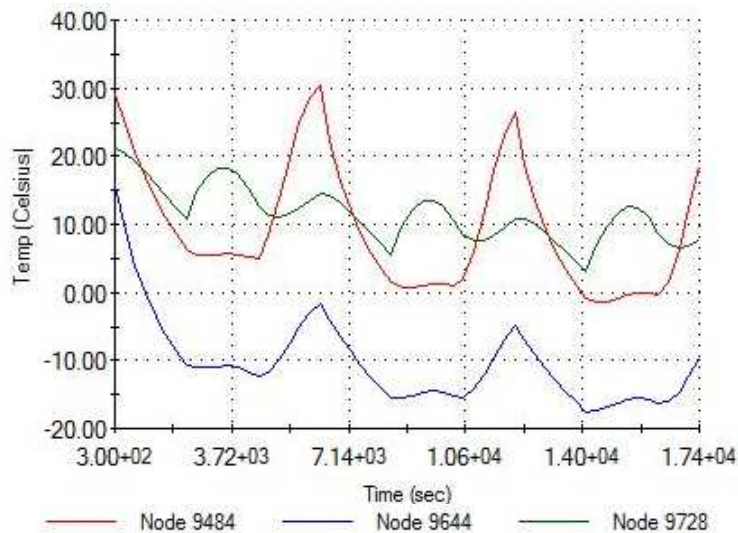


Figure 6.17. LLNL CI Transient response of the X facing frame/wall

6.3.2 Colony I $\beta=90^\circ$ Case

Due to the fact that the orientation of the spacecraft never changed with respect to the Earth and/or the Sun the steady state thermal case was not required to propagate

over several orbits. Rather, the FEA solver converged on a steady state temperature distribution and this solution was determined to be representative of the entire mission.

As is highlighted in Table 6.10, the lower electronics boards, where the PEC was planned to interface, reached about 50°C. The sun facing side, shown on the right of Fig. 6.18, reaches a steady state temperature of 54°C. The bottom face reached a maximum temperature of 125°C. Steady state temperatures in this range were clearly not considered as thermal strap connection locations. The remainder of the bus however maintained temperatures around 30°C and could potentially serve as thermal strap outlets if radiators were incorporated into the design.

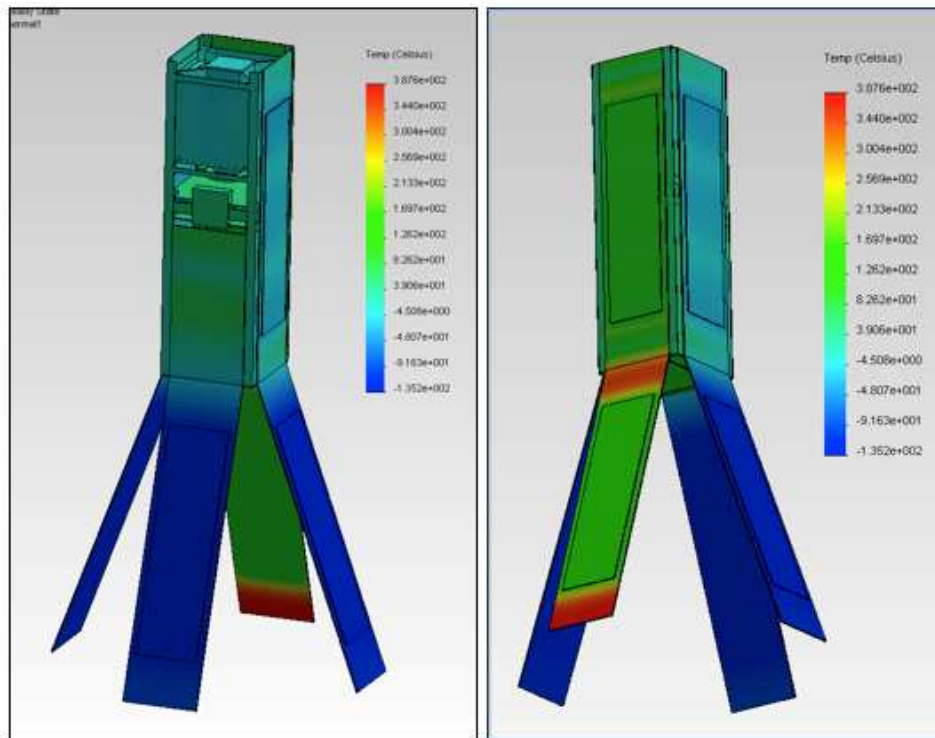


Figure 6.18. LLNL CI Steady state thermal results

Table 6.10 LLNL CI Steady State Temperatures

<u>Location</u>	<u>Node</u>	<u>Description</u>	<u>Temperature</u>
1	16117	+Y frame corner	53.5°C
2	16273	+Y electronics mount	54.7°C
3	14048	+YX frame corner	52.6°C
4	9676	X wall frame	5.7 °C
5	14288	-YX frame corner	38.4°C
6	10624	-Y frame corner	38.5°C
7	16327	-Y electronics mount	41.4°C

The table above tabulates the primary spacecraft locations considered as thermal strap interfaces. The probed locations range from approximately 38°C to 54°C.

6.3.3 Colony I Comparison of $\beta=0^\circ$ and $\beta=90^\circ$

On average, the external temperatures of the 90° beta angle case were on average two times as large as the 0° simulation. This undoubtedly occurred as a result of the short periods of 'true' eclipse present in the 0° beta case which allowed the satellite to cool significantly. If, rather than looking at external gradients, the models are compared based on internal temperatures, the 'worst case' thermal model environment is produced by 90° beta angle. In this steady state analysis, the payload reaches a temperature of 24°C whereas the transient temperature of the payload oscillates slightly around 0°C, after three orbits. Ultimately, the steady state case was used in the thermal strap design process in order to ensure worst-case hot temperatures

6.3.4 Proposed Thermal Management System

As mentioned above, the X frame/wall was identified as the most advantageous heat sink location because of exhibited low temperatures in the steady state case. Figure 6.19 shows the steady state temperature distribution along an X crossbar running behind the optimum X wall location, Node 9676.

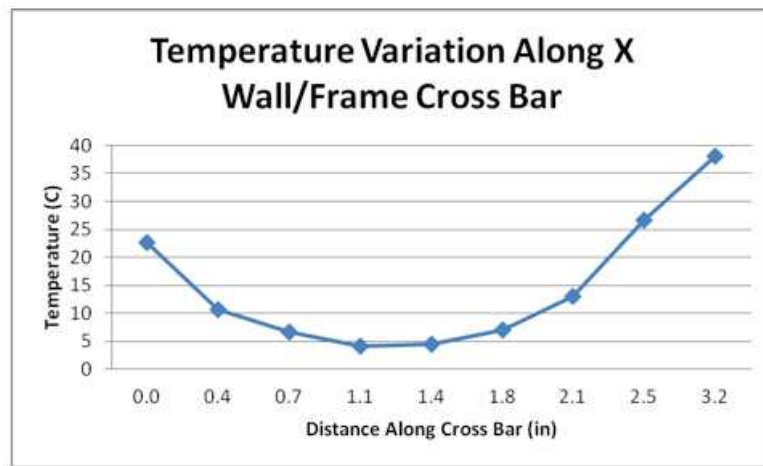


Figure 6.19. LLNL CI Temperature variation along the X frame/wall cross bar

The analysis showed that there was a 1.7in segment of the cross bar that remained below 10°C in the steady state case. Having identified an interface location and using the below resistance model, two thermal management configurations were examined, Fig. 6.20.

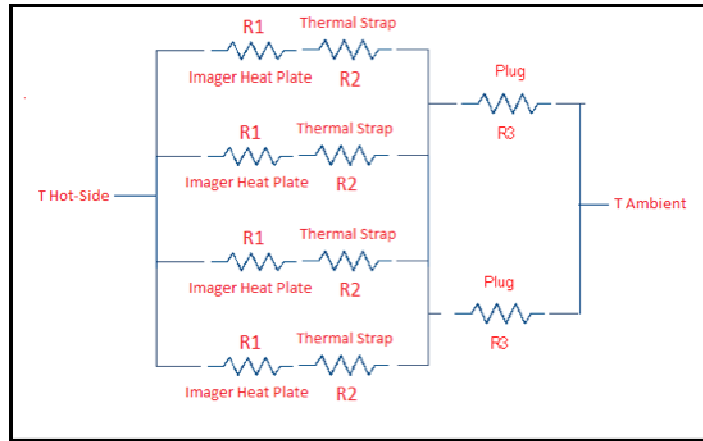
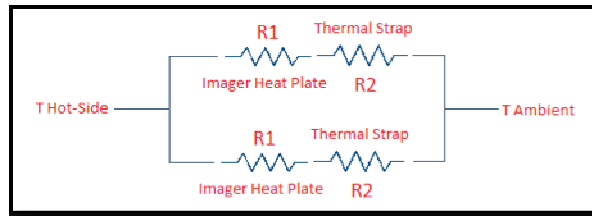


Figure 6.20. Resistance models for Configuration I (top) and Configuration II (bottom)

Both designs, Fig. 6.21, featured copper heat straps that connected directly to the imager board and bus frame. The first of these configurations, Configuration I, features two wide copper straps reaching from the long edges of the pinwheel plate to the frame. The second configuration, Configuration II featured four straps mounted directly from the pinwheel arms to the X frame/wall. The thermal resistance models for each of the proposed thermal strap designs are shown below. The $T_{\text{Hot-Side}}$ temperature was obtained from the simulation, as described above, and the total system was evaluated using the theory outlined in Section 5.

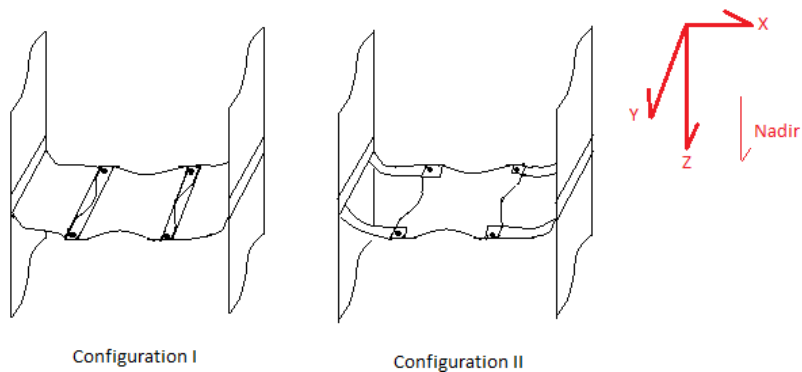


Figure 6.21. Thermal strap configurations

Ultimately, the Configuration I result featured two copper straps with widths of 1.7in and thicknesses of 0.005in. The lengths of each strap were specified as 1.4in and attached to the cross beams of the bus' (-X) and (+X) frames. The weight of the design, without fasteners, was estimated to be approximately 3.5g and would take minimal time to manufacture.

Conversely, the Configuration II result featured four copper straps with widths of 0.5in and thicknesses of 0.0525in. The lengths of each strap were specified as 1.4in and attached to the (-Y) and (+Y) regions of the cross beams on the (-X) and (+X) frames. The weight of this design, again without fasteners included, was 5.4g. Ultimately, both configurations were deemed viable options. The decision to utilize Configuration II was motivated dually by the additional space it allowed for through harnesses as well as the added maneuverability of smaller straps.

6.4 Colony II Thermal Results

Presented in this section are the results of the LLNL CII thermal simulation. Based on the results of CI, that the $\beta=90^\circ$ orbit case represented the worst case thermal environment, CII was exclusively subjected to steady state loads.

6.4.1 Colony II $\beta=90^\circ$ Case

As was to be expected due to an increase normal surface area to the Sun, the overall bus temperature of the Colony II configuration was slightly higher than the temperatures observed in the Colony I simulation. These values, which were approximately 50°C on the deployable, sun facing arrays, were on average 10°C warmer than the CI configuration. Figure 6.22, below, shows the exact magnitudes of these CII results.

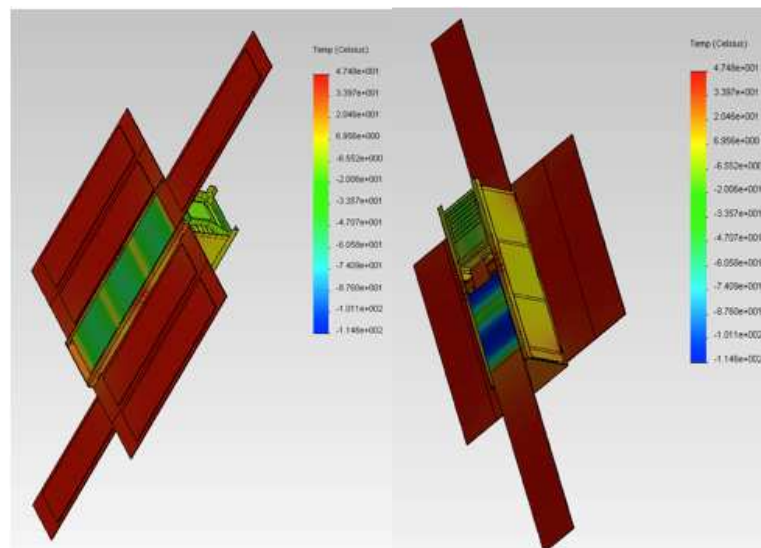


Figure 6.22. LLNL CII Steady state thermal results

Furthermore, the above simulated profiles provided a visual basis for several of the potential strap locations investigated during the analysis. Areas of consideration are highlighted in Table 6.11. From the table, it is clear that the space facing locations proved most efficient for heat removal. As was the case in the CI analysis, the temperatures present in Table 6.11 were utilized to re-evaluate the aforementioned Configuration II thermal resistance model.

The result of this analysis suggested that the originally proposed strap design was robust enough to sufficiently remove heat from the imager board in the CII configuration.

Table 6.11 LLNL CII Potential Strap Locations

<u>Location</u>	<u>Average Temperature</u>
Center Solar Panel GaAs Surface	45.0°C
Center Solar Panel Backing	45.0°C
Center Sun Side Body Silvered FR4 Panel	-5.0°C
Center Space Side Body Black FR4 Panel	-11.0°C
GPS board	32.0°C
Primary Mirror Surface	10.0°C
Center Telescope Space Side Wall	-14.0°C
Center Nadir Body Silvered FR4 Panel Surface	25.0°C
Center Radiator Surface	5.0°C

6.5 AggieSat4 Structural Results

The following section is an overview of the predicted structural behavior of the AGS4 satellite. At the time of this research, AGS4 was still in the design phase, so experimental testing had not been performed. Testing of AGS4 is slated for late 2014 by NASA.

6.5.1 AggieSat4 Natural Frequency

Using the aforementioned mesh density for a converged solution, 1.5cm, the natural frequency of AGS4 was calculated, Table 6.12. Analyzing the PSD curve for the Dragon Flight Environment highlighted dangerous vehicle specific frequencies in the 20-160Hz range. In the results presented below, the first mode frequency for AGS4 was well above 160Hz, Fig. 6.23. This indicates that the structure is less likely to experience resonance and fail under the vibration loads experienced on the Dragon launch vehicle.

Table 6.12: AGS4 Natural Frequency of First Five Modes

Mode No.	Frequency (Hz)
1	194.7
2	226.0
3	230.8
4	256.0
5	305.9

Shown in the Appendix, the second and third modes of the AGS4 natural frequency analysis were saturated by board movement and reveal little regarding the overall bus displacements. Furthermore, the displacements shown in the frequency figures are exaggerated and represent relative motion rather than absolute values. For this reason, only trends in component motion can be inferred. The figure below, exaggerated for viewing purposes, show that the ISIPOD deployer, developed by Innovative Solution in Space, experiences the highest response to the first mode frequency of 195Hz.

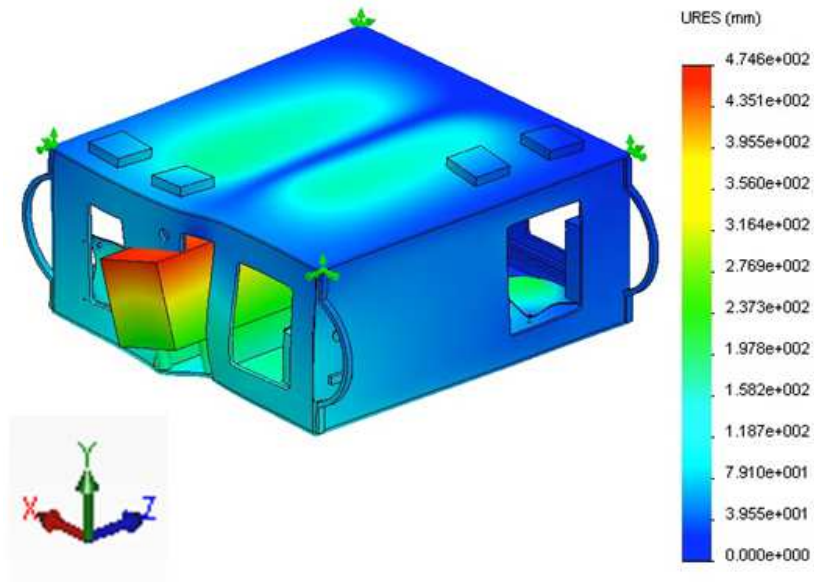


Figure 6.23. AGS4 1st mode natural frequency

6.5.2 AggieSat4 Random Vibration (X-Axis)

The following three sections present the results of the attenuated foam load excitations, presented in Section 5, scaled to 3dB. Scaling the base excitation curves to a 3dB values, both doubles the predicted loads and ensure the satellite can withstand a maximum test load environment. Table 6.13 shows 1σ RMS acceleration and stress values for various locations on the AGS4 satellite.

The X-direction excitation revealed a maximum acceleration of 28.6g and a maximum stress of 19.3MPa. The maximum acceleration occurred at an internally named 'alpha' CDH board while the maximum stress was experienced by the +Z wall of the structure. Comparison of this stress with the yield strength of Al 6061-T6 affirms that the structure is sound.

Table 6.12: AGS4 RMS Values for X-Axis Excitation (3dB)

Location	Acceleration (g)	Stress (Pa)
X- Panel	5.2	1.8E+06
X+ Panel	6.5	1.1E+06
Y- Panel	2.5	2.9E+06
Y+ Panel	3.2	2.3E+06
Z- Panel	3.6	2.6E+06
Z+ Panel	3.4	1.9E+07
EPS Bottom Board	3.4	1.6E+06
EPS Alpha W	3.5	9.1E+05
EPS Beta W	4.6	6.4E+05
EPS Gamma W	5.7	7.3E+05
EPS Delta W	6.9	7.0E+05
EPS Alpha I	3.8	4.0E+05
EPS Beta I	4.5	3.9E+05
EPS Gamma I	5.0	3.6E+05
CDH Alpha	28.6	1.4E+06
CDH Beta	4.3	6.6E+05
CDH Gamma	4.9	5.0E+05
CDH Delta	5.2	1.7E+05
Battery Board (Facing EPS)	4.0	2.6E+04
Battery Board (Facing ISIPOD)	5.6	1.5E+04
DRAGON Board EPS	3.6	1.7E+05
DRAGON Board CDH	10.3	1.2E+06
I Beam (+y)	4.1	1.4E+07
I Beam (-y)	3.2	6.2E+06
Model MAX	28.6	1.9E+07

Below, Fig. 6.24 shows the locations probed for PSD response investigations.

These locations captured representative features of the AGS4 bus such as Al 6061-T6 walls, PCB stacks, and battery box assemblies.



Figure 6.24. AGS4 PSD X-Axis probe locations

Table 6.14 correlates the probed response locations from the model to the nodal name indicated in Fig. 6.25.

Table 6.13: AGS4 Probed Locations for X-Axis PSD Response

Node	Location	Color
CDH Alpha	92074	Red
DRAGON Board CDH	107687	Blue
X+ Panel	238374	Black
EPS Delta W	66816	Green

Below are the PSD responses for the X-Axis excitation of the AGS4 model. As was expected, based on RMS results, the CDH 'alpha' boards demonstrated the largest acceleration. This peak of 20g occurs between 40-60Hz.

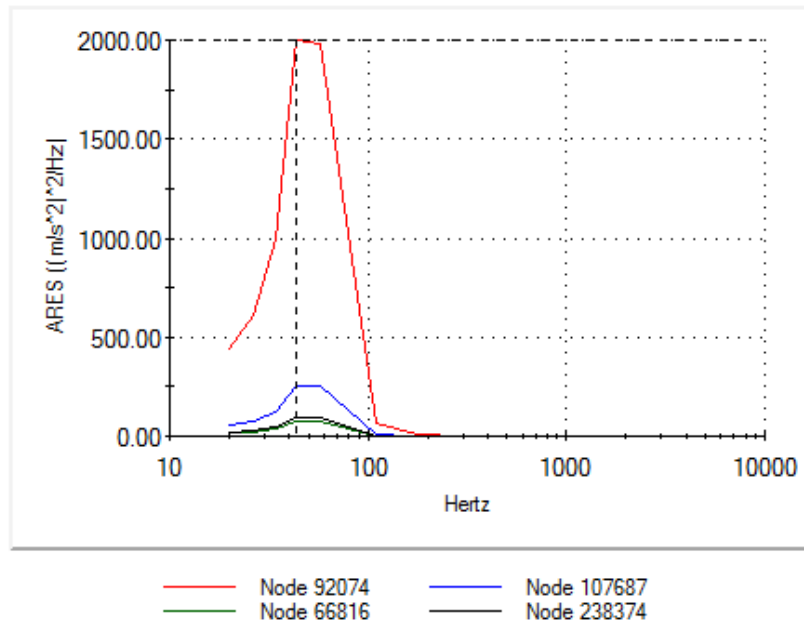


Figure 6.25. AGS4 PSD response for X-Axis excitation

6.5.3 AggieSat4 Random Vibration (Y-Axis)

The values probed for RMS responses for the Y-Axis random vibration analysis were identical to those probed in the X-Axis simulation. These values are shown below in Table 6.15. The Y-direction excitation revealed a maximum acceleration of 6.5g at the location probed on the -Y wall and a max stress of 20.3MPa on the -X panel.

Table 6.15: AGS4 RMS Values for Y-Axis Excitation (3dB)

Location	Acceleration (g)	Stress (Pa)
X- Panel	2.1	2.0E+07
X+ Panel	1.7	2.9E+06
Y- Panel	6.5	5.4E+06
Y+ Panel	5.0	5.6E+06
Z- Panel	2.5	6.4E+06
Z+ Panel	3.4	1.6E+07
EPS Bottom Board	2.1	1.0E+06
EPS Alpha W	2.4	4.9E+05
EPS Beta W	3.1	2.8E+05
EPS Gamma W	3.8	3.2E+05
EPS Delta W	4.6	2.3E+05
EPS Alpha I	2.5	2.2E+05
EPS Beta I	2.9	1.6E+05
EPS Gamma I	3.4	9.5E+04
CDH Alpha	6.0	1.4E+06
CDH Beta	3.6	4.6E+05
CDH Gamma	4.4	5.8E+05
CDH Delta	5.9	5.2E+05
Battery Board (Facing EPS)	2.3	3.9E+04
Battery Board (Facing ISIPOD)	1.7	1.1E+04
DRAGON Board EPS	2.0	1.8E+05
DRAGON Board CDH	4.2	4.9E+05
I Beam (+y)	1.9	1.1E+06
I Beam (-y)	1.7	1.0E+07
Model MAX	6.5	2.0E+07

Figure 6.26 shows the location, along with Table 6.16, probed for PSD response curves. Unlike the RMS outputs, the PSD probe locations were not maintained between axes. Rather, each axis was probed in locations of interest or concern. For the Y-Axis, the ISIPOD was of particular interest due to the observed first mode natural frequency behavior. Additionally, the -Y panel was investigated to ensure reasonable and safe responses due to the high acceleration observed during the RMS survey.

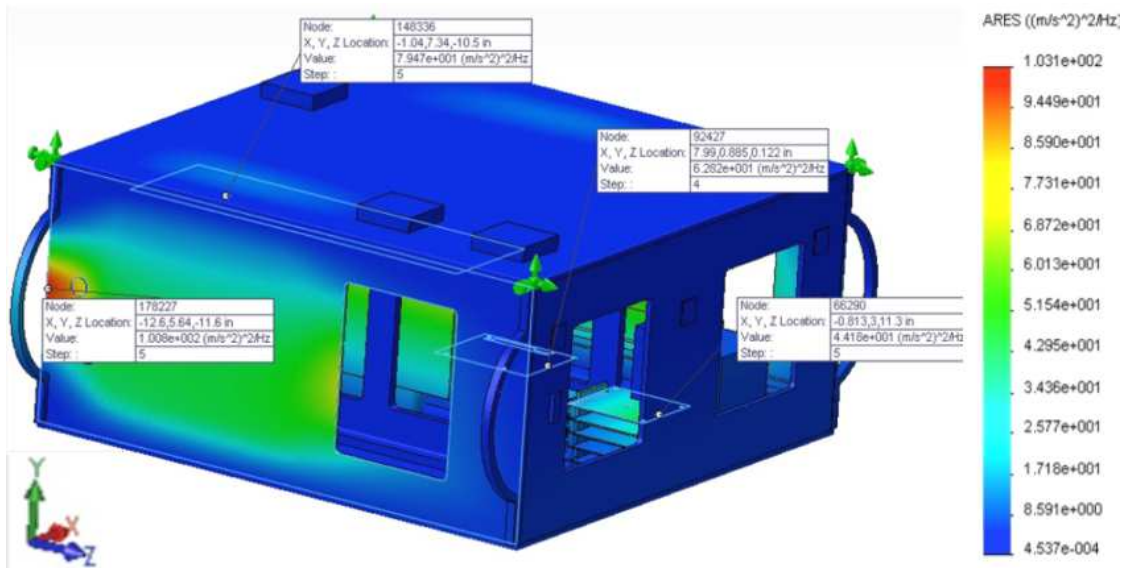


Figure 6.26. AGS4 PSD Y-Axis probe locations

Table 6.16: AGS4 Probed Locations for Y-Axis PSD Response

Node	Location	Color
Y- Panel	178227	Red
CDH Alpha	92427	Green
EPS Delta W	66290	Blue
ISIPOD	148336	Black

Figure 6.27 shows the PSD responses for four probed location of the AGS4 structure. The maximum peak shown corresponds to the -Y panel and is approximately 1g in magnitude. All four nodes show similar modes shapes with a peak frequency of approximately 60Hz.

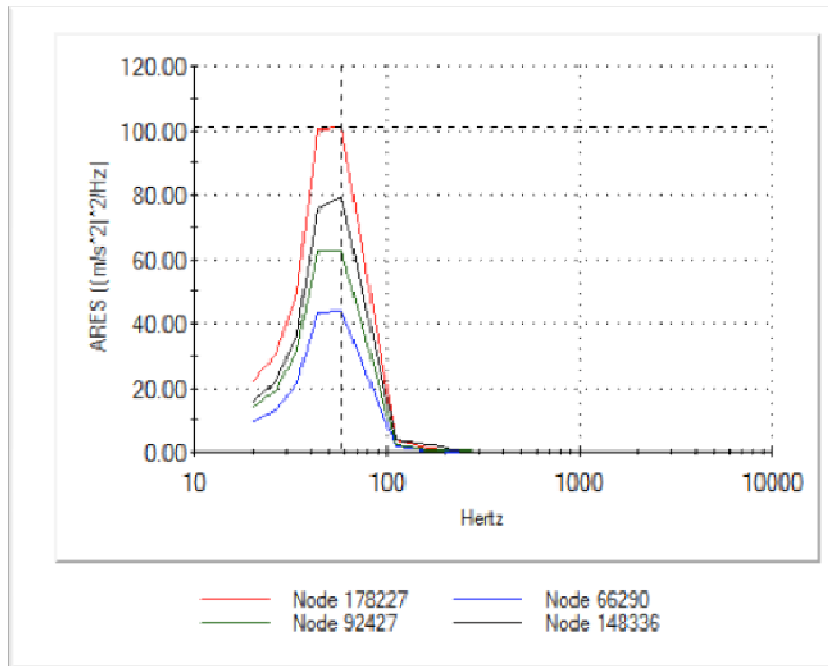


Figure 6.27. AGS4 PSD response for Y-Axis excitation

6.5.4 AggieSat4 Random Vibration (Z-Axis)

Lastly, the Z-direction excitation revealed a maximum acceleration of 21.9g and a max stress of 68.8MPa. As with the previous two analyses, the alpha CDH board experienced the highest accelerations while an internal I-Beam was the component with the maximum stress. Again, a comparison of this stress value and the material's yield strength, 275MPa, shows that there is almost a FS of four for the I-Beam. NASA standards require most flight parts to meet FS of at least two. Additionally, the excitations utilized for the above three simulations were completed at test loads, and are consequently higher than anticipated flight environments by a factor of two.

Table 6.17: AGS4 RMS Values for Z-Axis Excitation (3dB)

Location	Acceleration (g)	Stress (Pa)
X- Panel	2.9	4.3E+06
X+ Panel	1.7	4.1E+06
Y- Panel	2.5	9.4E+06
Y+ Panel	2.9	1.2E+07
Z- Panel	6.3	5.0E+06
Z+ Panel	5.7	3.3E+07
EPS Bottom Board	6.6	8.0E+05
EPS Alpha W	6.5	4.2E+05
EPS Beta W	6.6	5.0E+05
EPS Gamma W	6.7	5.4E+05
EPS Delta W	6.8	4.1E+05
EPS Alpha I	6.7	3.3E+05
EPS Beta I	7.0	3.6E+05
EPS Gamma I	7.0	2.8E+05
CDH Alpha	21.9	1.1E+06
CDH Beta	6.8	5.7E+05
CDH Gamma	6.9	4.4E+05
CDH Delta	7.0	3.3E+05
Battery Board (Facing EPS)	6.1	3.1E+04
Battery Board (Facing ISIPOD)	6.7	4.8E+04
DRAGON Board EPS	7.4	1.4E+06
DRAGON Board CDH	12.9	9.7E+05
I Beam (+y)	5.6	6.9E+06
I Beam (-y)	5.5	6.9E+07
Model MAX	21.9	6.9E+07

Table 6.17 summarizes the RMS values measured at each of the probed locations. Below, Fig. 6.28 showed the PSD locations utilized for the Z-Axis analysis. Of particular interest for this analysis was the -Z panel which, as shown above, had the highest RMS response of all six structural walls. This was not unexpected as the -Z panel houses the majority of AGS4's components and because the excitation acted through the panel's center of gravity.

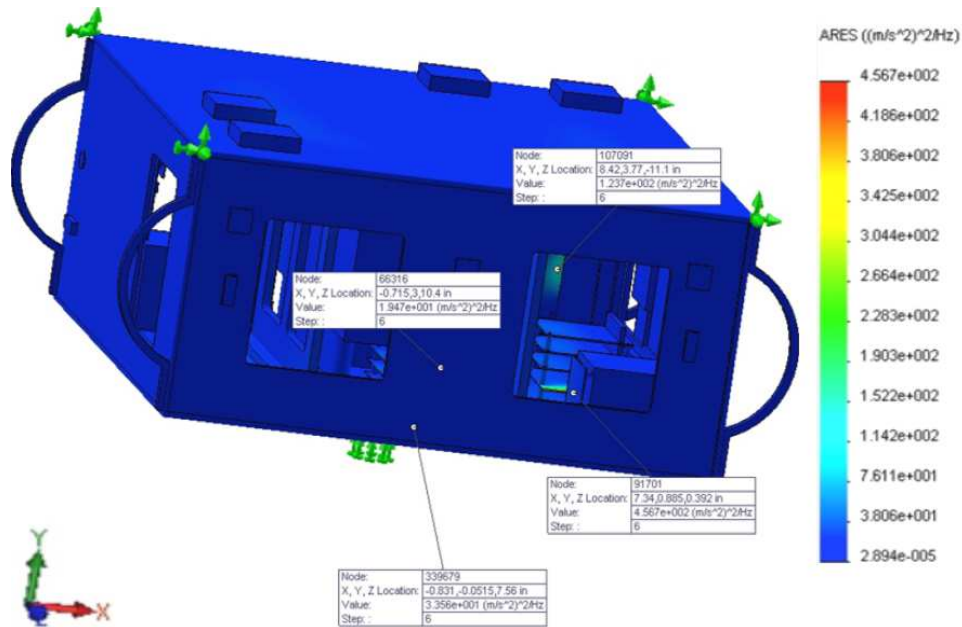


Figure 6.28. AGS4 PSD Z-Axis probe locations

Table 6.18, below, correlates the probed response locations from the model to the nodal name indicated in Fig. 6.28.

Table 6.18 AGS4 Probed Locations for Z-Axis PSD Response

Node	Location	Color
CDH Alpha	91701	Red
Dragon CDH	107091	Green
EPS Delta W	66316	Blue
Z- Panel	339679	Black

As can be seen in Fig. 6.29, the Z-Axis excitation elicited the highest frequency response. This single peak at approximately 100Hz was expected given the geometry of the AGS4 satellite. Namely, the Z panel of the satellite was double the size, and thus mass, of the side panels.

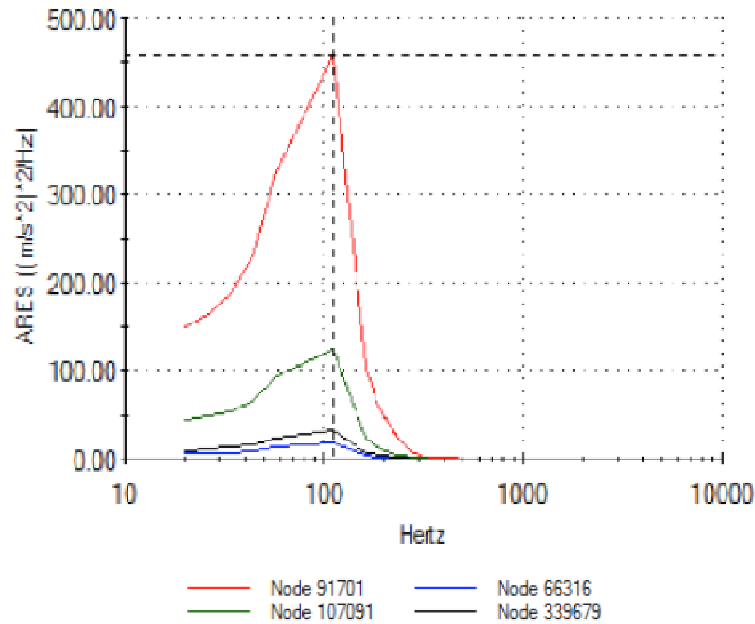


Figure 6.29. AGS4 PSD response for Z-Axis excitation

6.6 AggieSat2 and DragonSat Structural Results

The final section summarizes the results of the historical investigation of AGS2. Results for an integrated DragonSat system are presented for comparison with experimental testing and natural frequency data for the AGS2 independent model.

6.6.1 AggieSat2 and DragonSat Natural Frequency

The following natural frequency results were obtained at a converged maximum mesh size of 2.5mm. Table 6.19 summarizes the first five natural frequency modes for the AGS2 model.

Table 6.19: AGS2 Natural Frequency of First Five Modes

Mode No.	Frequency (Hz)
1	0
2	411.7
3	466.0
4	699.0
5	701.5

Due to the constraints on the model, translational motion was unconstrained along the axis running parallel to the SSPL deployment vector. For this reason, the first reported mode of the AGS2 model did not correspond to a frequency response but rather described complete translational motion. The second mode reported for the AGS2 model was approximately 410Hz. This value is significantly higher than those reported for AGS4 which is to be expected considering the relative size of the two satellites.

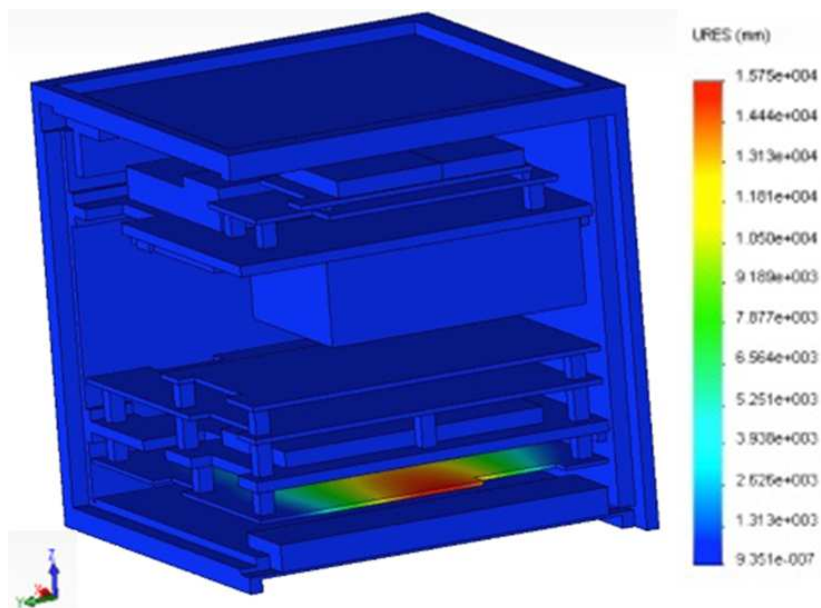


Figure 6.30. AGS2 2nd mode natural frequency

Figure 6.30, shows the second modal shape of the AGS2 satellite. The second mode's motion is completely isolated to the vibration of the bottom PCB board. All subsequent modes can be found in the Appendix.

Table 6.20, below, shows the natural frequency of the integrated DragonSat system and SSPL launcher. These solutions were obtained with the mesh characteristics described in Section 5. The converged mesh used therefore featured a maximum element size of 0.5mm and had approximately 670K nodes.

Table 6.20: DragonSat Natural Frequency of First Five Modes

Mode No.	Frequency (Hz)
1	483.3
2	486.4
3	524.9
4	525.1
5	812.5

Below, Fig. 6.31 shows the first modal shape of the DragonSat and SSPL system. Not surprisingly, the first mode features the same PCB's motion, which characterized the AGS2 natural frequency response. Moreover, the second mode, shown in the Appendix, highlights the second AGS2 model's top +Z PCB deformation.

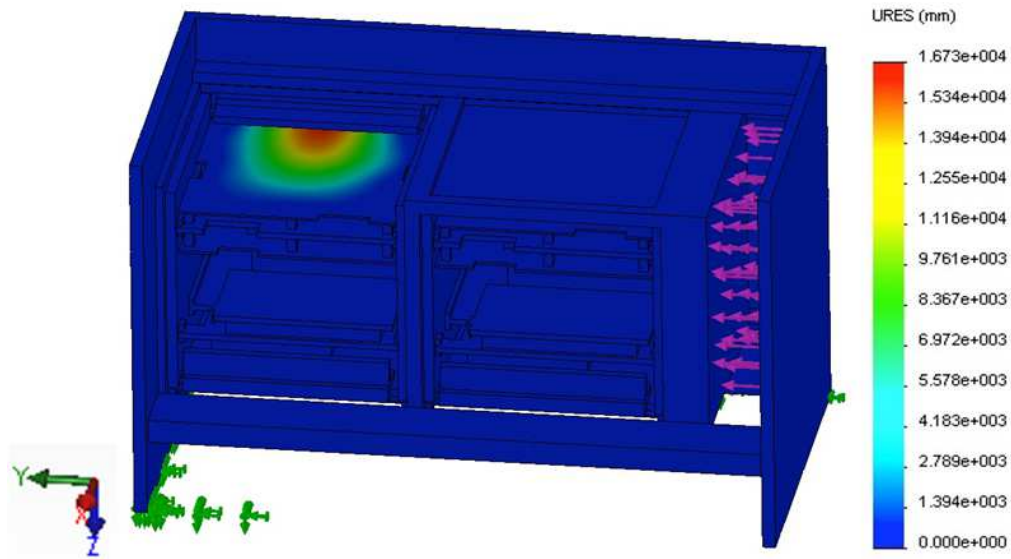


Figure 6.31. DragonSat and SSPL 1st mode natural frequency

6.6.2 DragonSat Random Vibration (X-Axis)

The results from the random vibration simulations and experimental testing for the X-Axis of the AggieSat/DragonSat payload are shown below. The PSD curves presented in Section 5 were inputted as shown and represented a 0dB case. The output PSD curves presented below are utilized in Section 7 to evaluate the CAD tool. Figure 6.32 shows where accelerometers were located on the exterior rear of the SSPL during experimental testing as well as a representative probe location for each measurement location. Likewise, Fig. 6.33 shows X and Y-Axis accelerometers and representative probe locations. While the exact node was not utilized to measure responses in all three axes, efforts were made to choose appropriate placement for each of the nine PSD probe instances.

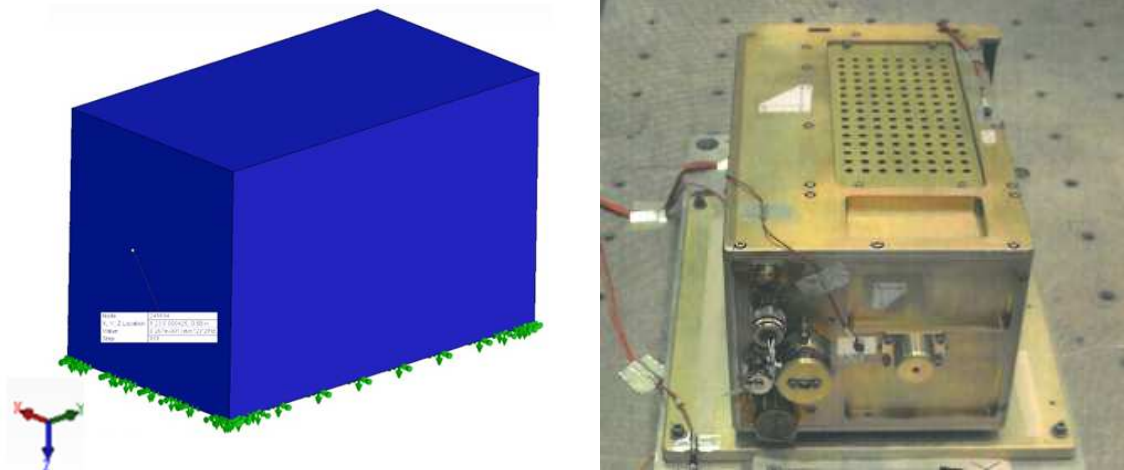


Figure 6.32. SSPL rear PSD probe locations (left) and physical model with accelerometers (right)



Figure 6.33. SSPL side PSD probe locations (left) and physical model with accelerometers (right)

The responses for the X-Axis random vibration analysis is shown below. Axis specific measurements were made in order to accurately compare experimental data from unidirectional accelerometers with simulation data. Figure 6.34 feature results from

the primary X-Axis, Y-Axis, and Z-Axis accelerometers, from top to bottom, respectively.

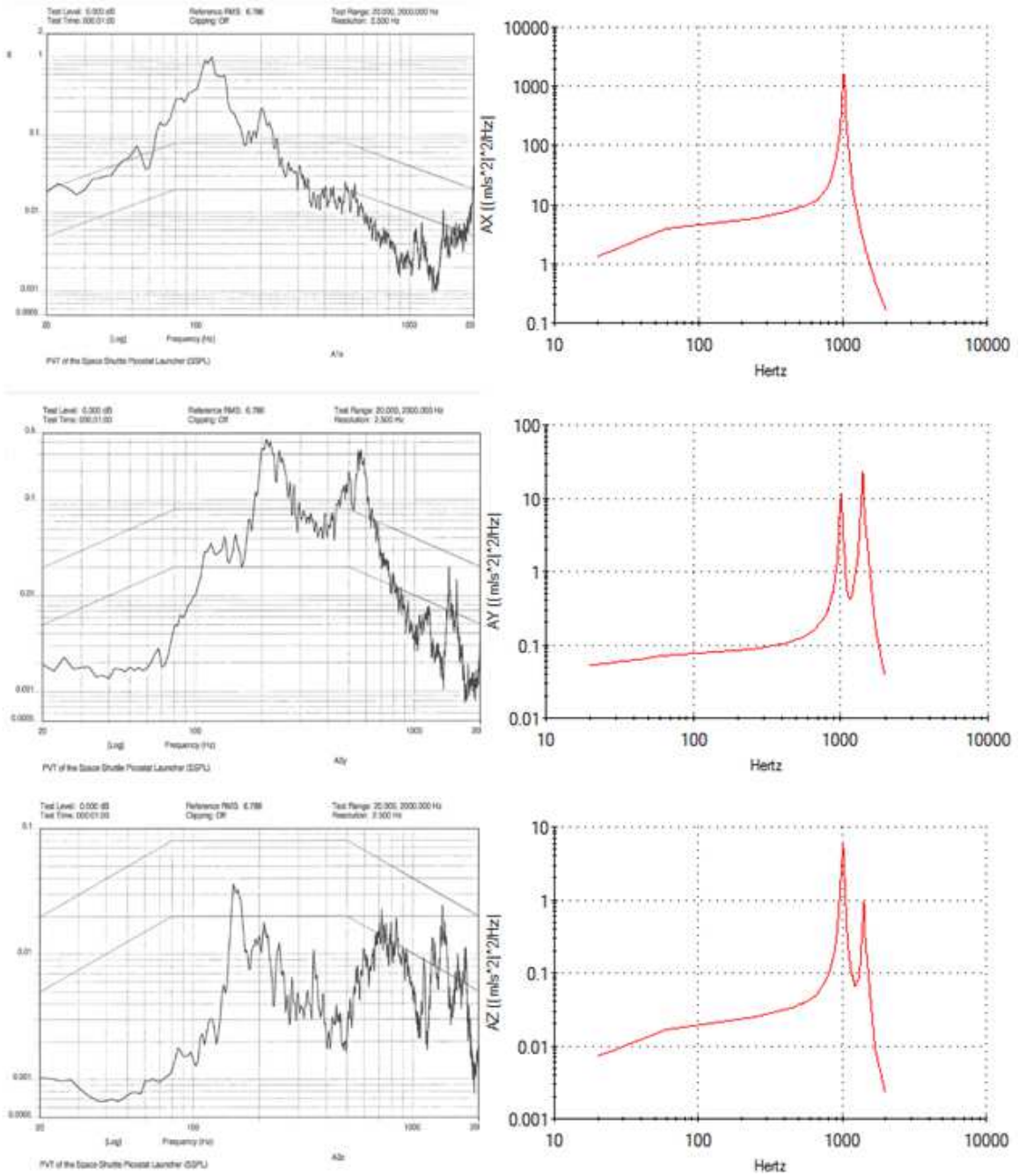


Figure 6.34. DragonSat and SSPL PSD response for X-Axis excitation

6.6.3 DragonSat Random Vibration (Y-Axis)

Similarly, Fig. 6.35 feature Y-Axis PSD response from the primary X-Axis, Y-Axis, and Z-Axis accelerometers, from top to bottom, respectively.

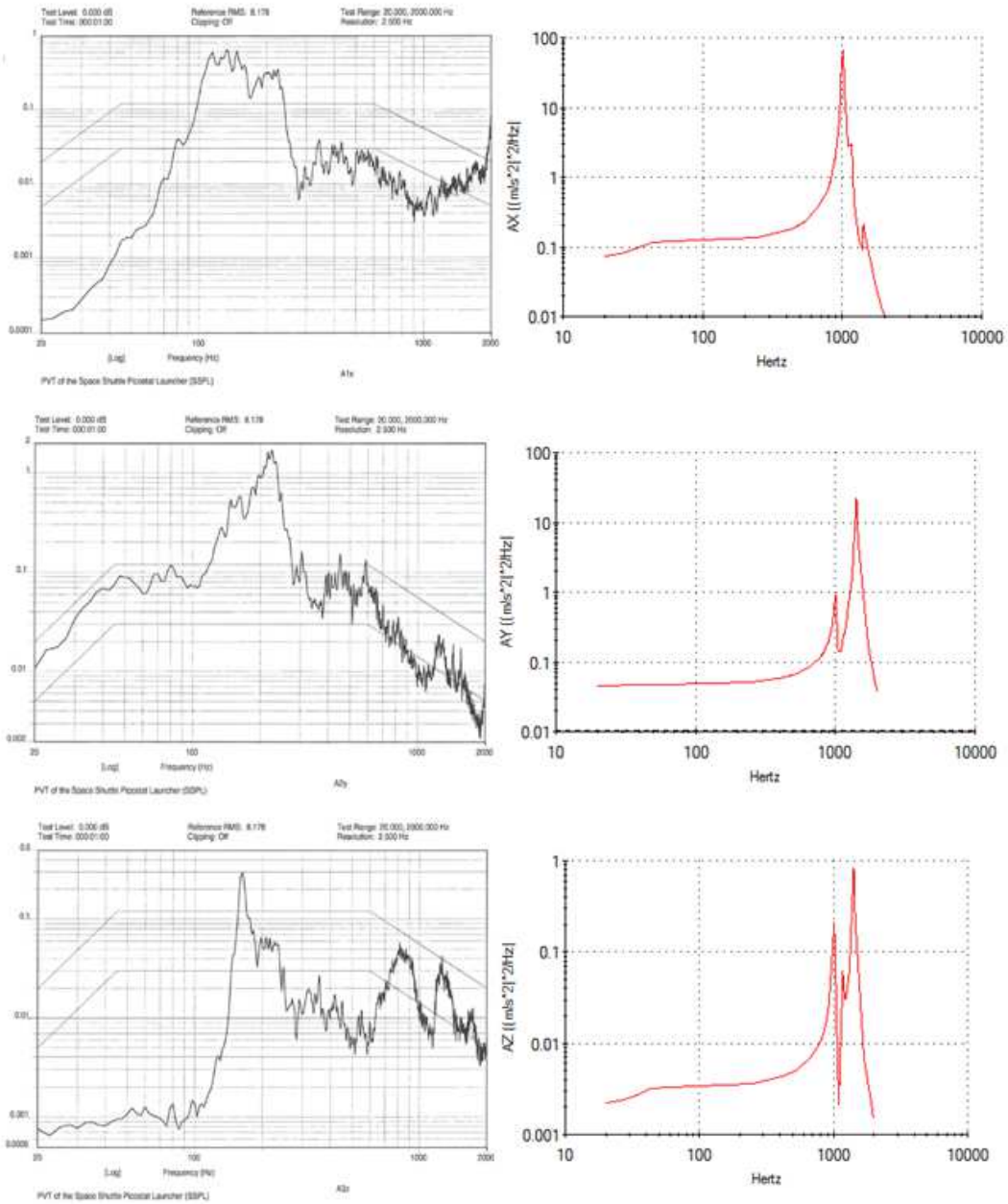


Figure 6.35. DragonSat and SSPL PSD response for Y-Axis excitation

6.6.4 DragonSat Random Vibration (Z-Axis)

Lastly, Fig. 6.36 features the Z-Axis PSD response of the primary X-Axis, Y-Axis, and Z-Axis accelerometers, from top to bottom, respectively.

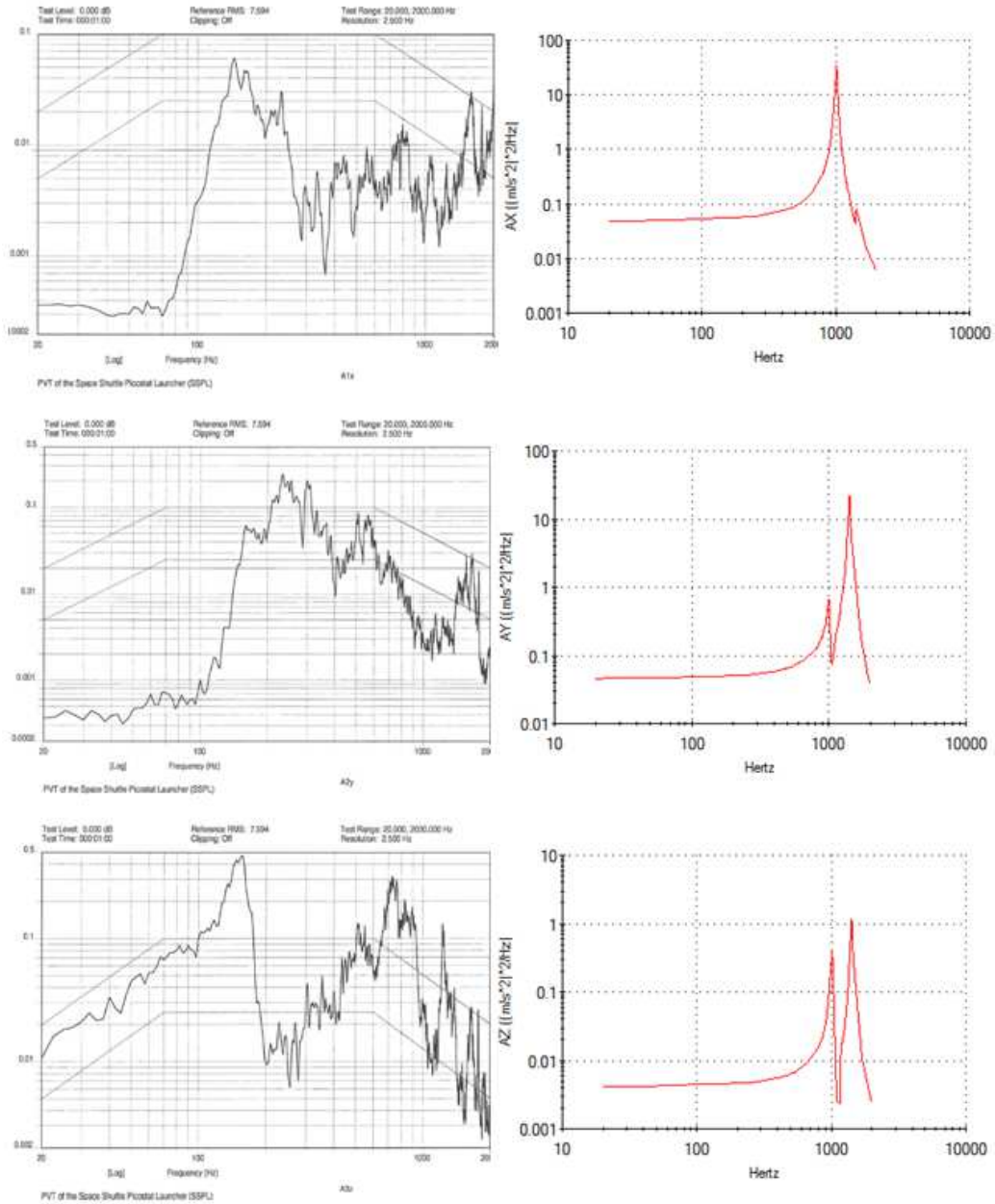


Figure 6.36. DragonSat and SSPL PSD response for Z-Axis excitation

The above random vibration results will be discussed and utilized to evaluate SolidWorks in the following section.

7. CONCLUSIONS

As previously stated, this research was meant to provide real world examples of small satellite behavior predictions using CAD based FEA solvers. This goal was addressed in the characterizations of the four structural models presented above. These responses, discussed for individual payloads in further detail below, show the predictive and investigative capabilities of CAD based FEA solvers. Clearly peak RMS loading lends insights to both overall system behavior and component level areas of concern. These structural response results not only highlight how satellite systems benefit from complete FEA solutions but also provide a baseline body of work from which future space system analyses might consider. Improvements to modeling processes learned from this research could then feed forward to drive more accurate reliable solutions for otherwise difficult to validate satellite payloads.

As a secondary goal, and due to the on-going nature of AGSL's internal satellite design, this research focused on creating useful models for future result comparison. This objective was achieved by utilizing result probe locations in representative testing configurations wherever possible. In instances where accelerometer locations had not yet been established or where the exact measurement location was unknown, external nodes reactions were recorded and the corresponding locations proposed for future hardware testing. Additionally, the aforementioned model simplifications were maintained throughout the ongoing design iterations of AGSL internal designs, even where higher fidelity modeling could have been achieved, in an effort to reserve computational power

for future model updated. For example, as the AGS4 design matures and an agreement regarding the exact packing configuration is achieved, the proposed probe locations may not be viable acquisition locations. Due to an effort to create useful models which feed forward to future designs, additional model components, i.e. packing material, can be added without limiting simulation performance.

Perhaps the most obvious objective of this research was to utilize a CAD package to predict three satellites' structural responses based on simulation and experimental data. While the below discussion serves to assess the predicted responses in both test and launch environments, it is worth noting the following direct benefits of the results presented within this report. Namely, the observed ability of the CAD program to highlight payload components requiring further attention from a design standpoint. This ability to isolate areas of high displacement or extreme temperature gradients leads itself to an iterate design process and performance confidence. Due to the complexity of such systems, vetting every instance of instability or high stress concentration would be nearly impossible without the use of the aforesaid CAD and CAD based FEA practices. On this merit alone, SolidWorks and other similar CAD packages prove to be invaluable design tools as well as effective structural response predictors.

The following section is meant to address the TML evaluation process alluded to throughout the totality of this research. Great effort has been taken up to this point to remain impartial to solution validity as simulation data was compiled. All programmatic validation metrics were established before results had been obtained and aside from crude solution sanity checks, no processing of the data was completed prior to this

section. To maintain this level of ethical reporting and present an accurate assessment of SolidWorks for continued use at AGSL, the following format will be utilized for each of the six models investigated: summary of validation metrics, determination if comparison between experimental and simulation data is possible, post-processing of data, evaluation of metric success, discussion of potential error and outline of possible ways to increase future accuracy. Based on the results of the aforementioned model investigations, a conclusion regarding SolidWorks' tool maturity will be reached and a suggestion for future use presented.

7.1 Version 2 Investigation

A successful V2 payload was identified as one capable of capturing experimental result trends and predicting relative responses. Additionally, the requirement that a component's random vibrate response be within plus/minus half an order of magnitude of experimental values was levied on the simulation model. Due to the fact that NPS completed V2 testing in Monterey, California in late 2011 and because the testing adhered to strict procedures, a comparison between V2 simulation data and experimental data will prove insightful.

In order to accurately compare the PSD results for the V2 model, it is important to note that the log scale of the experimental results is a factor of two higher than the simulated results. Moreover, as a default output, SolidWorks reports PSD results in $(\text{m/s}^2)^2/\text{Hz}$. These units of ASD must be scaled in order to meaningfully evaluate the above metrics. The conversion between the SolidWorks default and the standard

experimental output, g^2/Hz , is 96.04. This value, which represent $(9.8\text{m/s}^2)^2$, is utilized to scale down the simulation solution for experimental comparisons.

One primary peak was identified in the experimental prediction of the V2 payload in the X-Axis. The peak occurred at approximately 700Hz. The simulated results showed a peak at 1500Hz. For this axis the validation metric was deemed a failure. For the Y-Axis, on the other hand, experimental testing showed a peak at 1300Hz while simulations produced a peak at 1250Hz. For this axis the validation metric was met and the simulation accepted. Lastly, for the final axis, both experimental and simulated random vibration results show a double peak spike. In the experimental results, the first and more pronounced of these peaks occurred at 1100Hz while the latter peak was at 1400Hz. The simulation reading for the Z-Axis, on the other hand, showed the lower peak occurring at 1100Hz and the higher frequency peak arising at 1250Hz. These values meet the metrics established for V2 and thus for the third and final axis, the metric was successful.

Perhaps the most obvious source of model error for the V2 payload simulation was the use of a fixed geometry restraint for the bottom plate of the test pod. This fictitious rigidity could have easily caused artificially higher frequency responses and damped or eliminated responses at lower frequencies. In the simple plate simulation, this impact on the results was especially apparent in the out-of-plane simulations and could potentially explain why the Y-Axis simulation results were so close to the experimental results. Additionally, this research utilized the lowest damping ratio value within the presented range of acceptable quantities. Either the damping ratio or boundary

condition selection could have adversely affected the validity of the above results. To quantify such impacts, the following sensitivity tests were completed.

7.1.1. Version 2 Sensitivity Analysis

In order to capture both the highest and lowest possible responses given a variety of boundary conditions and damping ratios the V2 simulation, as described in Section 5 was rerun with the following alterations. Originally the mesh utilized had a maximum element size of 4mm and 700K nodes. The mesh used to obtain the below results had a maximum element size of 2mm, 2M elements and 3M nodes. Another change made to the model was that four interior sheet metal walls were included in the payload. The thin Al 6061-T6 walls are 0.02in thick and mounted externally to the payload unit and baffle set. These walls were not included in the original model because of low relative mass and potentially cumbersome meshing thicknesses.

After the walls were integrated into the model, four additional simulations were rerun for each of the three axes. The simulations included the following configurations: a 0.03 damping ratio model with a fixed geometry bottom plane, a 0.03 damping ratio model with a roller slider boundary condition on the bottom plane and fixed mounting holes, a 0.07 damping ratio model with a fixed geometry bottom plane, and a 0.07 damping ratio model with a roller slider boundary condition on the bottom plane and fixed mounting holes. For three different probe locations, accelerometer A, B, and D from Section 5, the X-Axis results are presented below, Figs. 7.1-7.3.

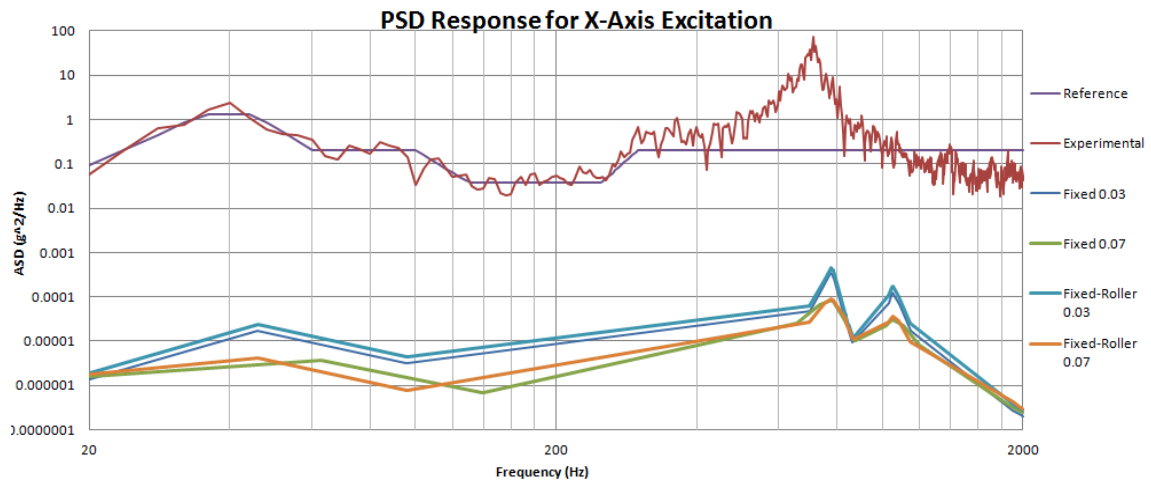


Figure 7.1. LLNL V2 PSD response for X-Axis excitation, Sensor A

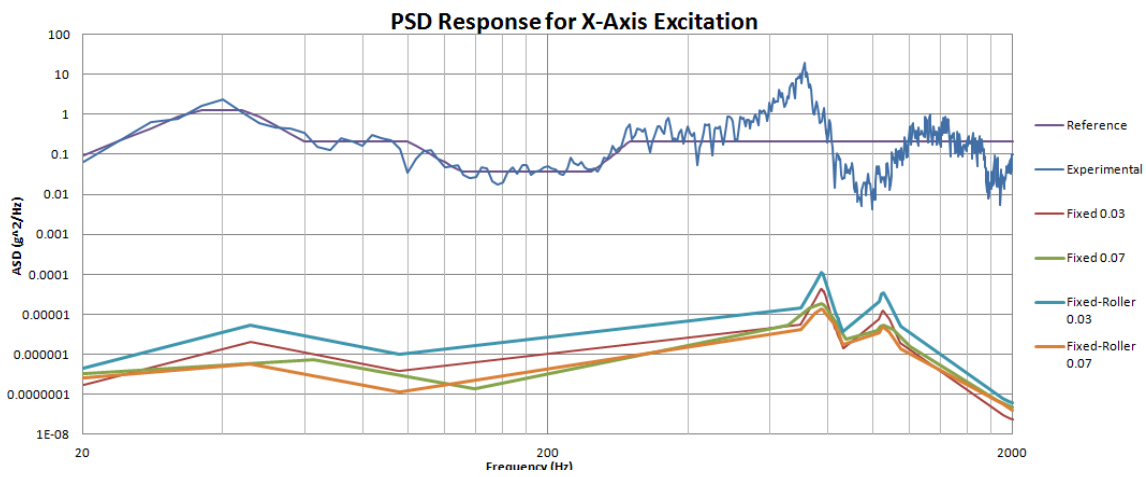


Figure 7.2. LLNL V2 PSD response for X-Axis excitation, Sensor B

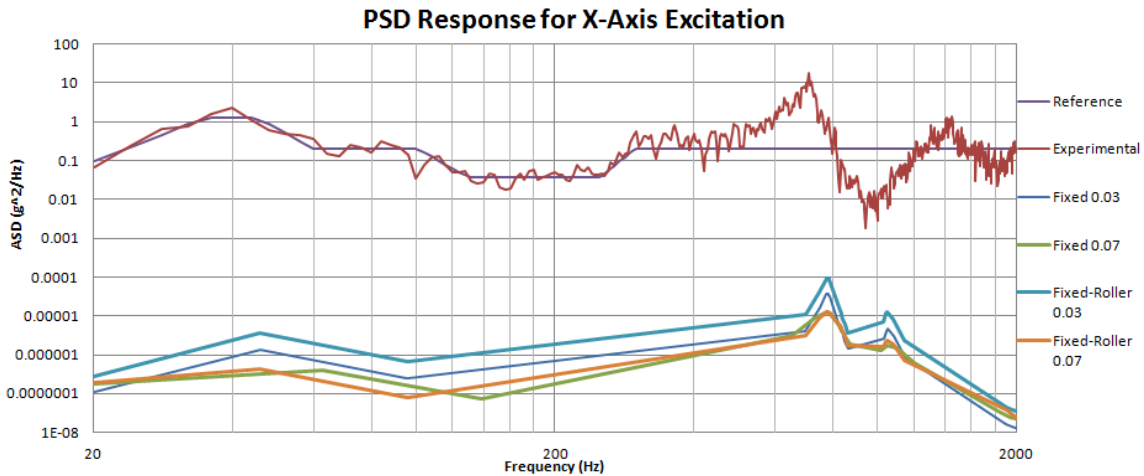


Figure 7.3. LLNL V2 PSD response for X-Axis excitation, Sensor D

As can be seen above, for each of the probes locations of the X-Axis simulations, the combination roller/slider and fixed geometry mounting holes, with a damping ration of 0.03 produced results closest to the experimental data. Whereas in the initial simulation's results featured a single peak at 1500Hz, the results above show a much higher agreement between experimental and simulated data. For example, Sensor A's experimental data showed a predominate peak at 700Hz while the simulated data showed a frequency response at 790Hz. Likewise, Sensor B's laboratory data shows a primary frequency peak and a smaller response at approximately 700Hz and 1300Hz, respectively. The simulated results for this sensor showed peaks at 774Hz and 1052Hz. Lastly, the experimental results compiled from Sensor D showed peaks at 700Hz and 1450Hz. The simulated data for Sensor D showed responses at approximately 775 and 1050Hz. All three of the sensor used to collect frequency response data for the X-Axis

pass the validation metric's success criterion and could be utilized for structural response prediction.

The results for the Y-Axis simulations are presented below, Figs. 7.4 and 7.5. The results for the +Y and +X face sensors, previously discussed in Section 5, represent the out-of-plane response for this payload.

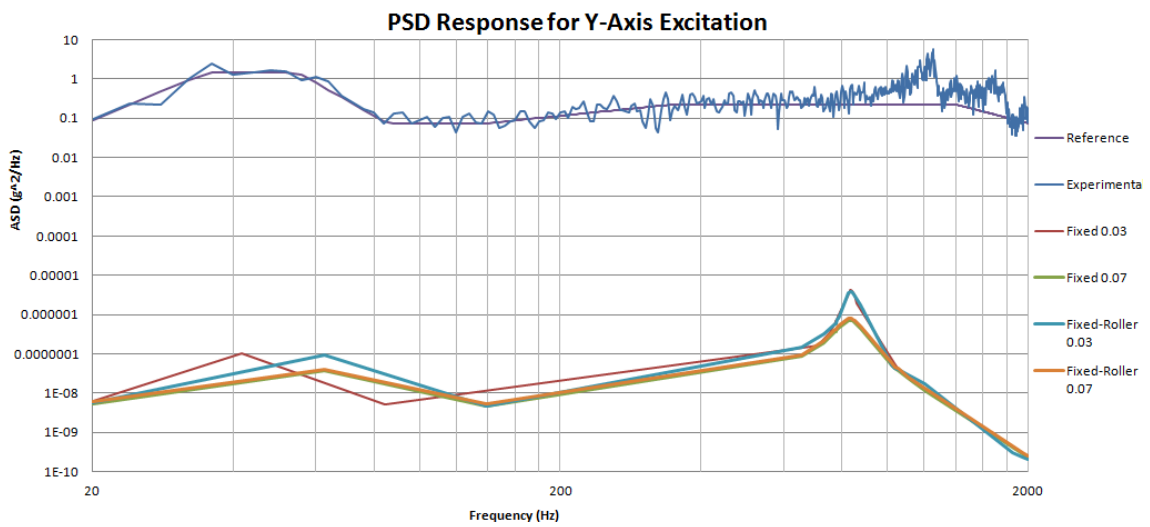


Figure 7.4. LLNL V2 PSD response for Y-Axis excitation, +Y face sensor

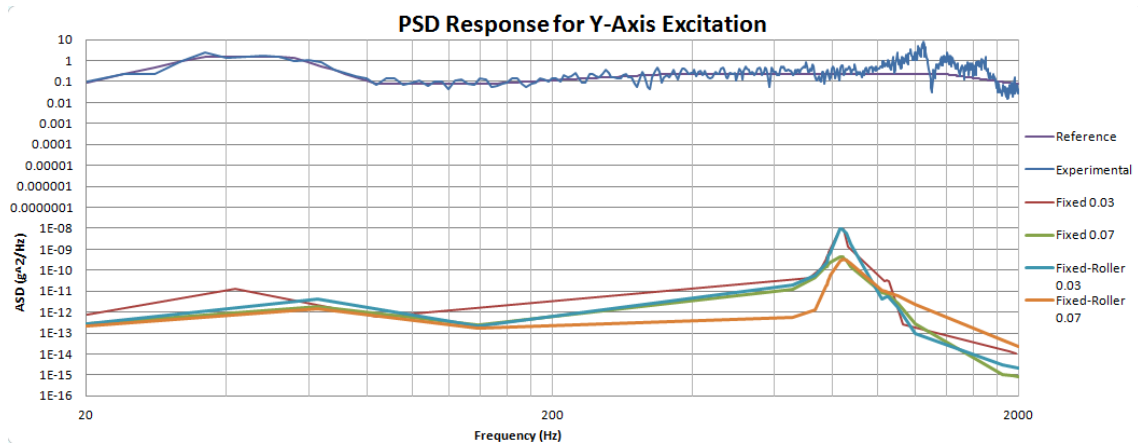


Figure 7.5. LLNL V2 PSD response for Y-Axis excitation, +X face sensor

Above, the both the +X and +Y face simulation responses featured peaks at 850Hz while the experimental data had a peak at 1250Hz. These results do not show an improvement over the originally simulated model and therefore suggest that the fixed plate boundary conditions may have been more suitable for capturing out-of-plane responses for this particular payload. The Z-Axis sensitivity simulation results are presented below, Figs. 7.6 and 7.7.

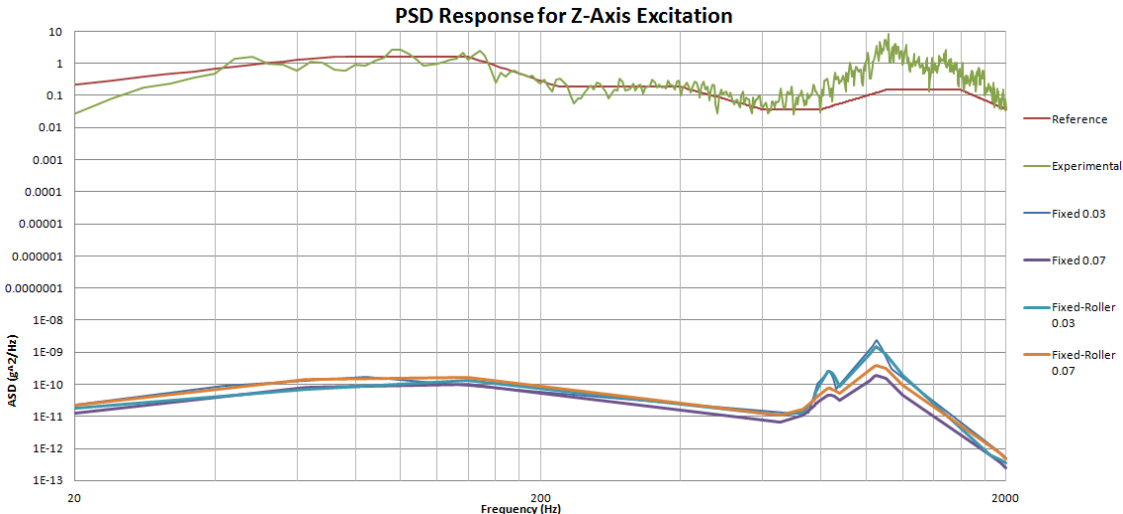


Figure 7.6. LLNL V2 PSD response for Z-Axis excitation, -Z face sensor

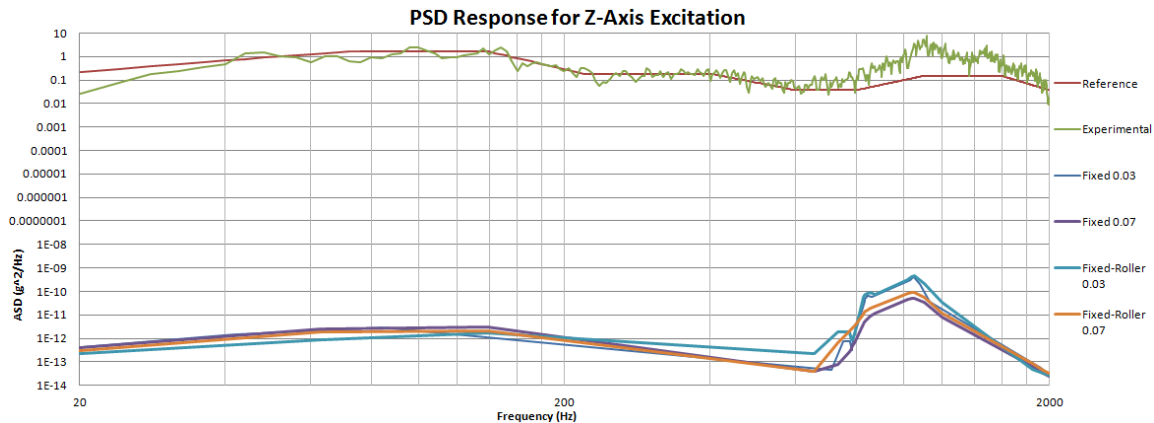


Figure 7.7. LLNL V2 PSD response for Z-Axis excitation, +X face sensor

The above results for the $-Z$ face location show frequency responses at 830Hz and 1052Hz. The simulated response measured on the +X face probed location peaked at approximately 1040Hz. Again, these responses were not an obvious improvement over the results of the initial simulation despite remaining within the tolerance of the validation metric. Ultimately, the sensitivity analysis revealed axis specific improvements for the V2 payload. Without a doubt, the lower damping ratio simulations were closer to experimental behavior and should continued to be utilized for additional models.

7.2 Version 3 Investigation

Accuracy for the V3 model was defined as peaks in experimental and simulation random vibe responses correlating to within half an order of magnitude. The ongoing nature of experimental testing for the V3 payload excludes the following metrics from being evaluated with physical test data. The above are suggestions for validation once

experimental data becomes available and may be worth reconsidering if the V2 model updating was successfully completed.

7.3 Colony I and Colony II Investigations

Both thermal simulations were employed to design a system capable of maintaining an approximate temperature of 5°C at the imager interface by generating a ~20°C temperature change across a TEC. Accuracy, while never defined, was loosely based on the simulations' predictive capabilities of on-orbit environments. Due to the nature of the simulations and an inability to recreate space thermal factors in a test facility, thermal outputs were considered exclusively predictive. Future model accuracy could be validated with reading from integrated payload thermistors. A recommended validation metric for the CII thermal simulation, should this method be employed, is that measured minimum and maximum temperatures for a quasi-steady state orbit fall within the predicted simulation profile ranges.

7.4 AggieSat4 Investigation

It was suggested that the AGS4 model be validated based on future internal accelerometer placements within an M0-1 bag, external to the foam-packing mold. Accuracy for the AGS4 random vibration was defined as peak responses in agreement to within $\pm 25\text{Hz}$. However, due to the fact that foam packing material was not physically modeled and because the flight configuration will include an M0-1 bag, results from the simulation may not have an obvious correlation to experimental data. Due to the ongoing

nature the AGS4 design and testing work, the metrics proposed herewith cannot be evaluated at this time. As with the STARE campaign, the suggestion stands to reevaluate the AGS4 simulation and model once both the flight and testing configurations have been solidified.

7.5 AggieSat2 Investigation

Accuracy standards for the AGS2 model were made purposefully rigorous to push the limits of the CAD tool. Namely, for the DragonSat model, simulation accuracy was defined as resonant frequencies within $\pm 100\text{Hz}$ of experimental data.

Due to the fact that AGS2 is a historical study, included in this research primarily due to the vast amounts of information available regarding the system's physical behavior, a comparison between simulation and experimental results is possible. As was the case in the V2 evaluation, SolidWorks PSD resonances must be converted from $(\text{m/s}^2)^2/\text{Hz}$ to g^2/Hz .

The experimental testing of AGS2 reported X-Axis responses in the three primary directions. In the X-direction, the response occurred at 110Hz. In the Y-direction two peaks are visible, the first at 200Hz and the second at 600Hz. Lastly, in the Z-direction three peaks were observed, one at 150Hz, another at 700Hz, and the final at 1500Hz. Simulation results in the X-, Y-, and Z- directions were as follows: in the X-direction, 1000Hz, in the Y-direction, 1000Hz and 1600Hz, and in the Z-direction, 1000Hz and 1600Hz.

In the Y-Axis results of the AGS2 experimental testing, the X-direction had a single wide peak spanning from 150-250Hz. The Y-direction exhibited a frequency spike at 200Hz. And the Z-direction measurement peaked in three unique locations: 150Hz, 800Hz, and 1400Hz. Simulation results for AGS2 again show excessively high frequency responses. The X-direction response showed a peak at 1000Hz. Two peaks occurred in the Y-direction, the first at 1000Hz and the second at 1500Hz. Lastly, while the tri-peak results of the Z-direction appeared initially promising, simulated results showed acceleration rises at 1000Hz, 1100Hz, and 1500Hz.

Lastly, the Z-Axis experimental data had a peak which occurred in the X-direction, of about 150Hz. In the Y-Axis, an acceleration surge was seen at 250Hz. The Z-direction response of the experimental data revealed two peaks; one at 150Hz and the other at 750Hz. Simulation results for the Z-Axis PSD in the X-direction suggested a 1000Hz response. The Y-direction probe revealed twin peaks at 1000Hz and 1500Hz. Finally, the Z-direction results show almost equivalent magnitude spikes at 1000Hz and 1500Hz.

All three readings for each of the three primary axes failed to meet validation metric standards. As previously discussed, the largest source of error in the AGS2 model was the SSPL model. Without mechanical drawings of the launcher, this uncertainty may never be rectified. However, higher fidelity from the EDU may help pacify the above discrepancy.

7.6 Recommendations

Based on the results of the aforementioned model investigations, SolidWorks Simulation has been evaluated as a TML-1 for use at AGSL. This evaluation does not limit the current role the CAD software has in the laboratory and should not be viewed in an adverse light. TML-1 tools are classified as sufficient for investigative studies, for which SolidWorks is currently being utilized. Additionally, this research highlights pitfalls in current modeling processes and how such shortcomings impact the validity of results. Moving forward, it is recommended that future results be subjected to sensitivity analyses, similar to those presented for the LLNL V2 payload, in order to obtain results which most closely describe reality.

REFERENCES

¹Simulia. “Enhanced FEA and Simulation Software Reduces Development Time and Costs.” Sealing Technology. (2012), Vol. 2011: 4-5.

²Szabo, Barna and Ricardo Actis. “Simulation Governance: Technical Requirements for Mechanical Design .” Computer Methods in Applied Mechanics and Engineering (2012), Vol. 249: 158-168.

³William Weaver, Jr. and Paul Johnson. Finite Elements for Structural Analysis. Englewood Cliffs, NJ: Prentice-Hall Inc., 1984.

⁴Allen, Davis H. and Walter E. Haisler. Introduction to Aerospace Structural Analysis. New York: John Wiley & Sons, 1985.

⁵Akin, J. Ed. Finite Element Analysis Concepts via SolidWorks. Washington, D.C.: World Scientific, 2009.

⁶Petyt, Maurice. Introduction to Finite Element Vibration Analysis. Cambridge, England: Cambridge University Press, 1990.

⁷Maia, Nuno and Julio Silva. Theoretical and Experimental Modal Analysis. Somerset, England: Research Studies Press Ltd., 1997. 1-67.

⁸Adams, Vince and Abraham Askenazi. Building Better Products with Finite Element Analysis. Sante Fe, NM: OnWord Press, 1999.

⁹Mottershead, J. E. “Model Updating in Structural Dynamics: A Survey.” Journal of Sound and Vibration (1993), Vol. 163: 347-375.

¹⁰Anderson, Andrew, Benjamin Ellis and Jeffery Weiss. “Verification, Validation and Sensitivity Studies in Computational Biomechanics.” Comput Methods Biomech Biomed Engin (2007), Vol. 3: 171-184.

¹¹Park, Nam-Gyu, et al. “A Computational Technique to Identify the Optimal Stiffness Matrix for a Discrete Nuclear Fuel Assembly Model.” Nuclear Engineering and Design (2012), Vol. 255: 51-58.

¹²Kenigsbuch, R. and Y. Halevi. "Model UpDating in Structural Dynamics: A Generalized Reference Basis Approach." Mechanical Systems and Signal Processing (1998), Vol. 12: 75-90.

¹³Kleindorfer, George B., Laim O'Neil and Ram Ganeshan. "Validation in Simulation: Various Poisitions in the Philosophy of Science." Management Science 44 (1998), Vol. 44: 1087-1099.

¹⁴Peng, Hao, Xiang Ling and Juan Li. "Numerical Simulation and Experimental Verification on Thermal Performance of a Novel Fin-plate Thermosyphon." Applied Thermal Engineering (2012), Vol. 40: 181-188.

¹⁵Fan, Qingwei, et al. "Thermal Stress and Strain Distributions of a Laboratory Scale Wall Fired Furnace: A Numerical Study and Experimental Verification." Engineering Failure Analysis (2012), Vol. 25: 227-237.

¹⁶Cowels, Bradford, Dan Backman and Rollie Dutton. "Verification and Validation of ICME Methods and Models for Aerospace Applications." Integrating Materials and Manufacturing Innovations (2012), Vol. 1: 1-16.

¹⁷Zhang, Dong Lin, et al. "Optimal Design of Bogie Parameters Determination Test Bench Gantry Framework Based on SolidWorks/Simulation." Trans Tech Publications (2011) Vol. 199: 1253-1256.

¹⁸Defense Industry Daily Staff. "Small Is Beautiful: US Military Explores Use of Microsatellites." 2011, 30-June. Defense Industry Daily. Defense Industry Daily LLC. 2013, 15-May <<http://www.defenseindustrydaily.com/Small-Is-Beautiful-US-Military-Explores-Use-of-Microsatellites-06720/>>.

¹⁹McGowan, Eileen. Space Transportation Costs: Trends in Price Per Pound to Orbit 1990-2000. Consulting Report. Bethesda, MD: Futron Corporation, 2002.

²⁰DePasquale, Dominic and John Bradford. Nano/Microsatellite Market Assessment. Publication. Washington D.C.: SpaceWorks Enterprises, 2013.

²¹Sewell, Rebecca. "LONESTAR Mission 2 Requirements Specification." AggieSat Laboratory. Requirements Document. College Station: Texas A&M University, July 2011.

²²Space Exploration Technologies Corp. C3-1 Dragon Interface Definition Document. Interface Document. Los Angeles, CA.

²³McPhail, Margaret. JSC Fastener Integrity Testing Program. Johnson Space Center Procedural Requirements. NASA. Houston, TX: Safety and Mission Assurance, 2008.

²⁴NASA. General Specification Vacuum Stability Requirements of Polymeric Material for Space Application. Specifications. Houston, TX: Non-Metallic Materials Technology Section, 1974.

²⁵NASA. Payload Safety Policy and Requirements for the International Space Station. Requirements Document. Johnson Space Center. Houston, TX: International Space Station Program, 2010.

²⁶Graves, John T. Small Satellite Applications of Commercial Off the Shelf Radio Frequency Integrated Circuits. Thesis. Texas A&M University. College Station, TX, 2011.

²⁷Scott, William B. "Modeling and Simulation Cutting Costs of EW Systems Testing." Aviation Week and Space Technology (2000), Vol. 153: 68.

²⁸Zori, Laith and Brad Eckhardt. "Computer Simulation Helps Keep Down Costs for NASA's "Lifeboat" for the International Space Station." Aircraft Engineering and Aerospace Technology (2002), Vol. 74: 442.

²⁹Aberdeen Group. Getting It Right The First Time. Simulation Driven Design Menchmark Report. Boston: Aberdeen Group, Inc, 2006

³⁰Bu, Quixiang. "5m Drum's FEA and Optimum Design Based on SolidWorks Simulation." Trans Tech Publications (2011), Vol. 221: 555.

³¹Feiyu, Zhang and Wang Qingyan. "Simulation of Two Kinds of Topdrive Stem Based on SolidWorks." Trans Tech Publications (2012), Vol. 224: 128-132.

³²Xing, Hongyan, Yanbin Zhang and Wuyang Huang. "Design and Simulation of Drum Solid-state Fermentation Equipment Based on SolidWorks." Trans Tech Publications (2012), Vol. 476: 438.

³³Peng, Ying. “Research of Thermal Analysis Collaboratively Using ANSYS Workbench and SolidWorks Simulation.” Trans Tech Publications (2012), Vol. 127: 262.

³⁴The American Society of Mechanical Engineers. ASME V&V 10-2006: Guide to Verification and Validation in Computational Solid Mechanics. Guildlines. ASME, 2006.

³⁵Szabro, Barna A. and Ricardo L. Actis. “On the Role of Hierarchic Spaces and Models in Verification and Validation.” Comput. Methods Appl. Mech. Engrg. (2009), Vol. 198: 1273-1280.

³⁶Cowles, B. A. and Dr. Dan Backman. Verification and Validation of ICME Methods and Models for Aerospace Applications. Guidelines and Recommended Best Practices. Wright-Patterson Air Force Base, OH: USAF AFRL/RXLM, 2011.

³⁷Incropera, Frank P., David P. Dewitt, Theodore L. Bergman, and Adrienne S. Lavine. Introduction to Heat Transfer. 5th ed. Hoboken, NJ: John Wiley & Sons, 2007. Print.

³⁸Zeid, Ibrahim. Mastering CAD/CAM. McGraw-Hill Higher Education, New York, NY, 2005. 670-728.

³⁹Dittberner, A., Studholme, M., Lozada, V. Space-Based Telescopes for Actionable Refinement of Ephemeris (STARE) Payload Test Report, Ver. 1. Test Report. Naval Postgraduate School. Monterey, CA, 2011.

⁴⁰Woolger, Colin. “Invar - Nickel Iron Alloy.” Materials World (1996): 332-333.

⁴¹ERIKS. “Sealing Elements Technical Handbook O-rings.” Handbook.

⁴²Irvine, Thomas. “DAMPING PROPERTIES OF MATERIALS Revision C.” November, 2004. June, 2013. <<http://syont.files.wordpress.com/2007/05/damping-properties-of-materials.pdf>>.

⁴³F. Stern, R. Wilson, H. Coleman, E. Paterson. “Verification and Validation of CFD Simulations.” Fluids Engineering Division. New Orleans, LA: ASME, 2001, Vol. 123: 793-802.

⁴⁴Wenschel Lan, Vidur Kaushish, Dan Sakoda, Jim Newman. Force Limited Vibration Testing on NPSCuL– What to Expect When You’re Expecting To Fly. 10th Annual CubeSat Workshop. Monterey, CA: Naval Postgraduate School Space Systems Academic Group, 2013.

⁴⁵Holman, J.P. Heat Transfer. 9th Edition. New York, NY: McGraw Hill, 2002. 25-56.

⁴⁶Sze, S. M. Semiconductor Sensors. Hoboken, NJ: J. Wiley, 1994. 535.

⁴⁷Hsu, Tai-Ran. “Mems & Microsystems Design & Manufacture.” India: McGraw-Hill Education, 2002. 235-270.

⁴⁸Gilmore, David G. Spacecraft Thermal Control Handbook. Vol. 1. El Segundo, CA: The Aerospace Press, 2002.

⁴⁹Siegel, Robert and John R. Howell. Thermal Radiation Heat Transfer. Second Edition. New York, NY: Hemisphere Publishing Corporation, 1981.

⁵⁰Pumpkin Inc. “CubeSat-class Payload Carrier Nanosatellite Assembly User Manual - First Release.” MISC 2 ICD. 2011.

⁵¹Stewart, P., Hays, K. Colony II Bus Payload Developer Guide. Version 1.2. Guide. Huntington Beach, CA: The Boeing Company, 2011.

⁵²V-Infinity. “Peltier Module.” Datasheet, CP20151. 2009.

⁵³Micron Technology Inc. “1/2-Inch Megapixel CMOS Digital Image Sensor.” MT9M001C12STM (Monochrome), Datasheet, MT9M001_DS_1.frm - Rev.C. 2004.

⁵⁴Compact, Single Frequency GPS+GLONASS Receiver Enhances Satellite Availability and Positioning. Datasheet, OEMV-1G Version 1a. 2010.

⁵⁵Riot, V., Olivier, S., Pertica, A., Bauman, B., Simms, L., De Vries, W. “Real-time Space Situational Awareness Initiative CubeSat sensor System Engineering Overview.” Version 1.1.13. System Overview Document. 2012.

⁵⁶Pumpkin Inc. “Miniature 3-Axis Reaction Wheel & Attitude Determination and Control System for CubeSat Kit Nanosatellites.” Datasheet, IMI-100 ADACS Hardware Revision: A, Document Revision E. 2010.

⁵⁷Space Technology Library. “Space Mission Analysis and Design.” Ed. W.J. (ed.), and Wertz, J.R. (ed.) Larson. 3rd. El Segundo, CA: Microcosm Press, 1999. 203-221; 533-575.

⁵⁸Space Technology Library. Space Mission Engineering: The New SMAD. Ed. David F. Everett, Jeffery J. Puschell James R. Wertz. El Segundo, CA: Springer Microcosm Press, 2011.

⁵⁹Diaz-Aguado, M.F. Formation Autonomy Spacecraft with Thrust, Relative Navigation, Attitude and Crosslink Program (FASTRAC) Thermal Vacuum Test and Thermal Model. Masters Thesis. Austin, TX: University of Texas , 2005.

⁶⁰Mather, J.C., Fixsen, D.J., Shafer, R.A., Mosier, C., Wilkinson, D.T. “Calibrator Design for the COBE Far Infrared Absolute Spectrophotometer (FIRAS).” The Astrophysical Journal (1999), Vol. 512: 511.

⁶¹Cooley, Jace. AGS4 Special Requirements. Requirements Document. College Station, TX: AggieSat Laboratory, 2013.

⁶²International Space Station Program. ISS Pressurized Volume Hardware Common Interface Requirements Document . Requirements. Houston, TX: NASA-Johnson Space Center, 2011.

APPENDIX

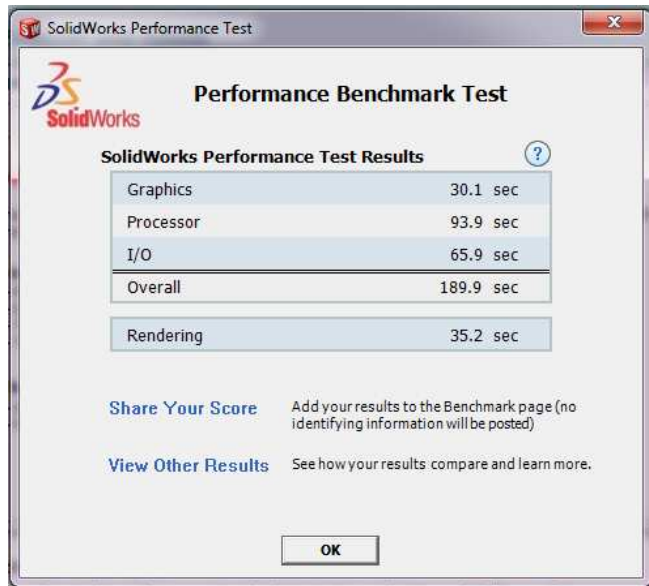


Figure A-1. Computer Specifications and Benchmark Results

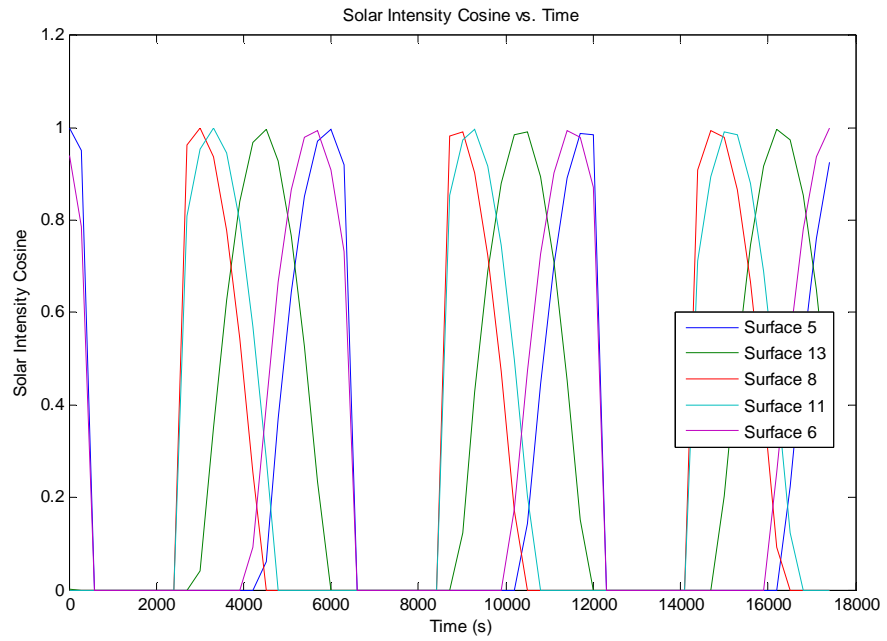


Figure A-2. Solar Incidence Cosine Curves for 3 Orbits Generated by MATLAB for use with the SolidWorks Simulation

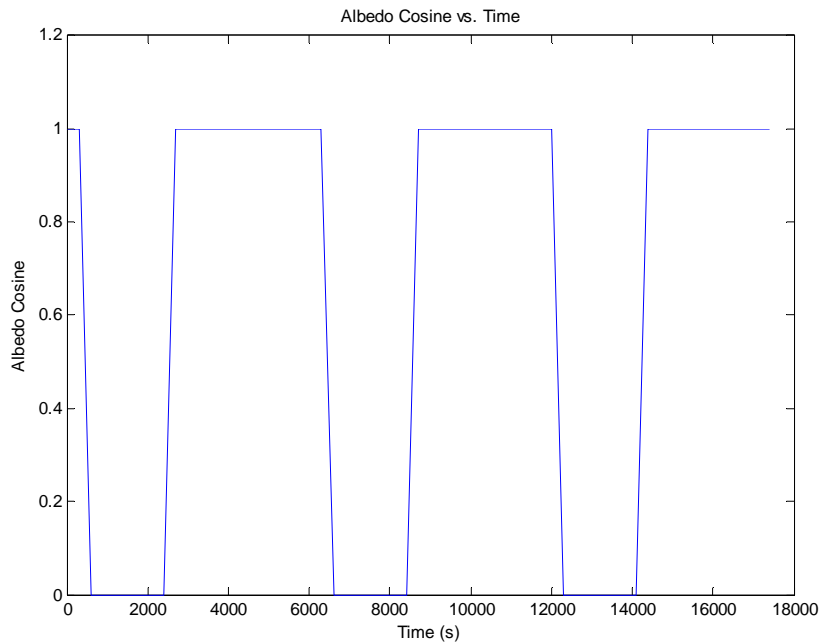


Figure A-3. Albedo Cycling Curve for 3 Orbits Generated by MATLAB for use with the SolidWorks Simulation

```

%% Inputs
alt=700; %km          orbits=3;          delt=300; %sec
%Surface unit vectors, f4 and f5 are deployable panel surfaces, others
%not included assumed to face Earth.
f1=[-1,0];          f2=[0,1];          f3=[1,0];
f4=[cos(20*pi/180),sin(20*pi/180)];
f5=[-cos(20*pi/180),sin(20*pi/180)];

%% Orbit and Time Calculations
%Angle computation for eclipse based on Earth radius and spacecraft radius
horz=sqrt((6375+alt)^2-6375^2);  temp=asin((1/(6375+alt))*horz);
fie=(pi-2*temp)/2;
%Orbit period
period=2*pi*sqrt(((6375+alt)^3)/398600);
%Circular orbit rate
rate=2*pi/period;          steps=floor(orbits*period/delt);
%Sun vector in spacecraft frame
theta=pi;          sun=[cos(theta),sin(theta)];
%% Iterative Calculation
for i=1:steps
    test=dot(sun,[0,-1]);
    %Check if spacecraft is in eclipse
    if test>=cos(fie)
        X(i,:)= [0 0 0 0 0];
        Y(i,1)=0;
    else
        %if not in eclipse, set albedo value and check and compute for faces in sunlight
        Y(i,1)=1;
        %face1, Surface 5
        test=dot(f1,sun);
        if test>0
            X(i,1)=test;
        else
            X(i,1)=0;
        end

        %face2, Surface 13
        test=dot(f2,sun);
        if test>0
            X(i,2)=test;
        else
            X(i,2)=0;
        end

        %face3, Surface 8
        test=dot(f3,sun);
        if test>0
            X(i,3)=test;
        else
            X(i,3)=0;
        end

        %face4, Surface 11
        test=dot(f4,sun);
        if test>0
            X(i,4)=test;
        else
            X(i,4)=0;
        end

        %face5, Surface 6
        test=dot(f5,sun);
        if test>0
            X(i,5)=test;
        else
            X(i,5)=0;
        end
    end
    %update sun angle and vector
    theta=theta+rate*delt;          sun=[cos(theta),sin(theta)];
    %update time
    T(i,1)=(i-1)*delt;
end

```

Figure A-4. MATLAB Sun Angle Computational M-file

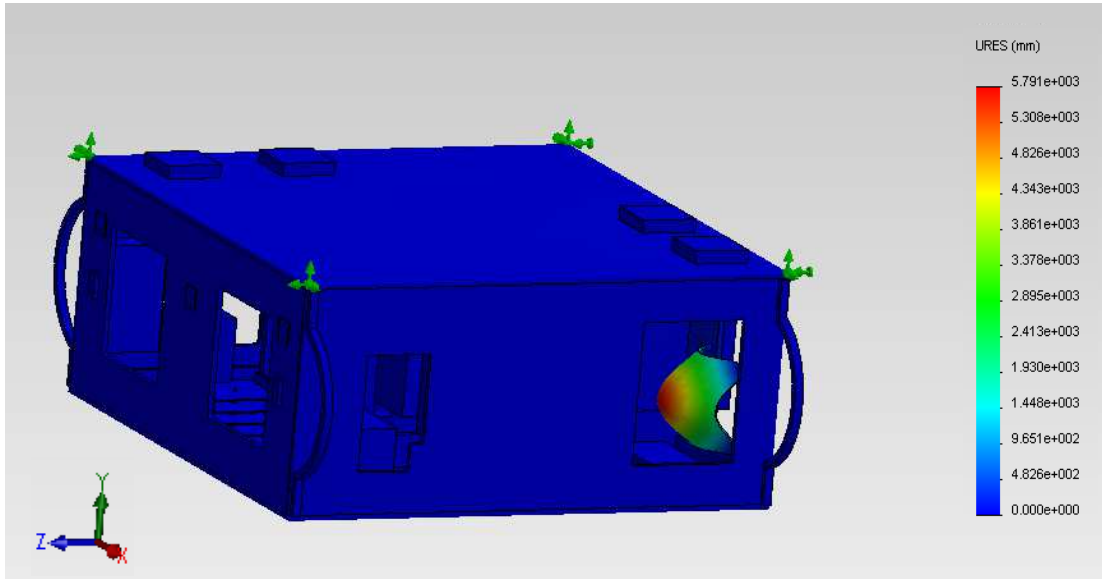


Figure A-5. AGS4 2nd mode natural frequency

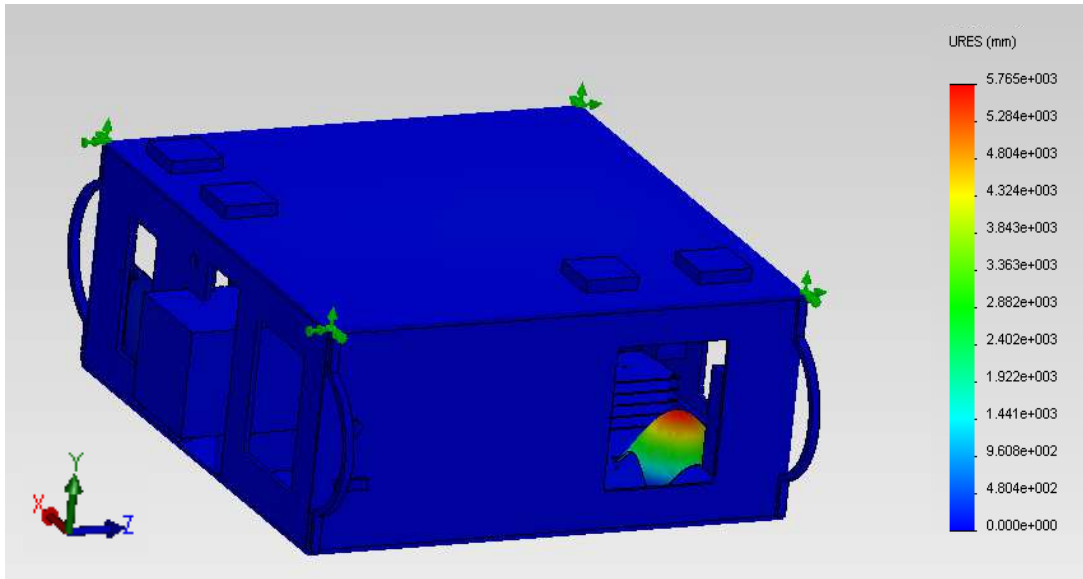


Figure A-6. AGS4 3rd mode natural frequency

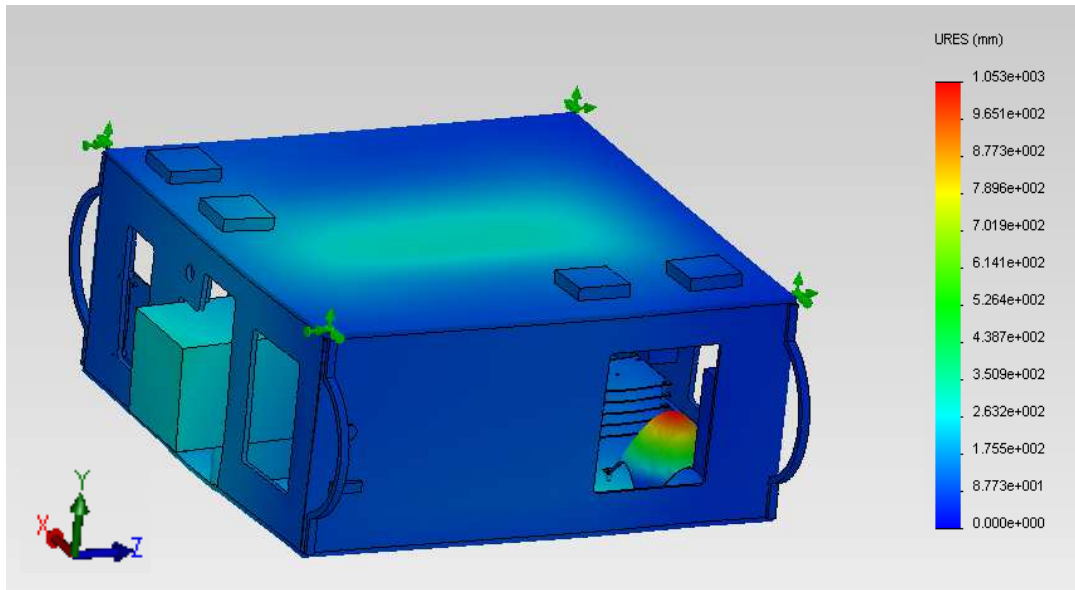


Figure A-7. AGS4 4th mode natural frequency

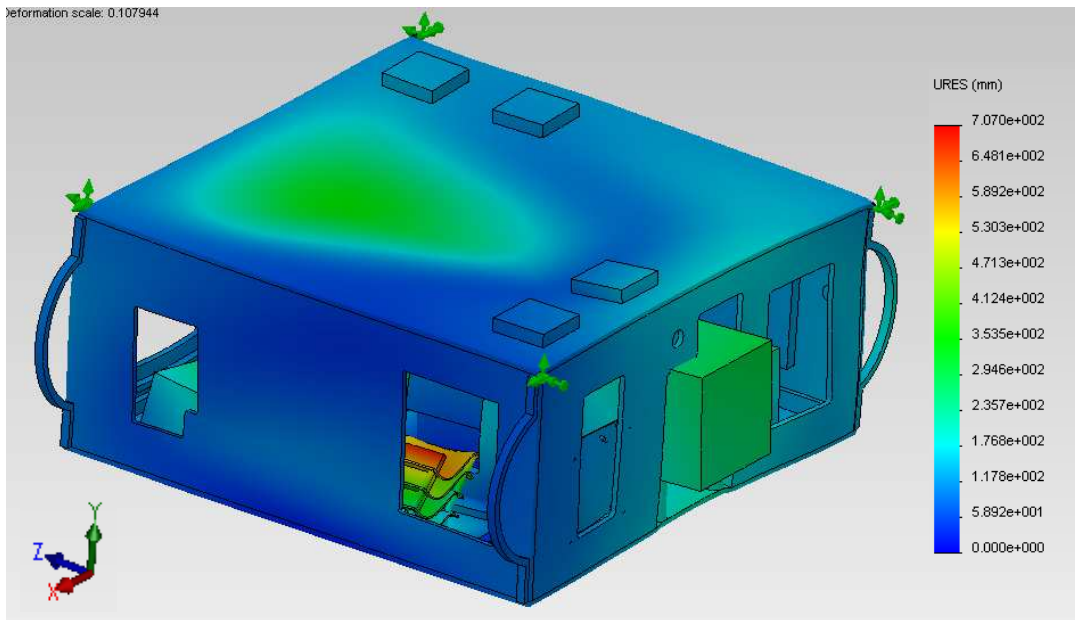


Figure A-8. AGS4 5th mode natural frequency

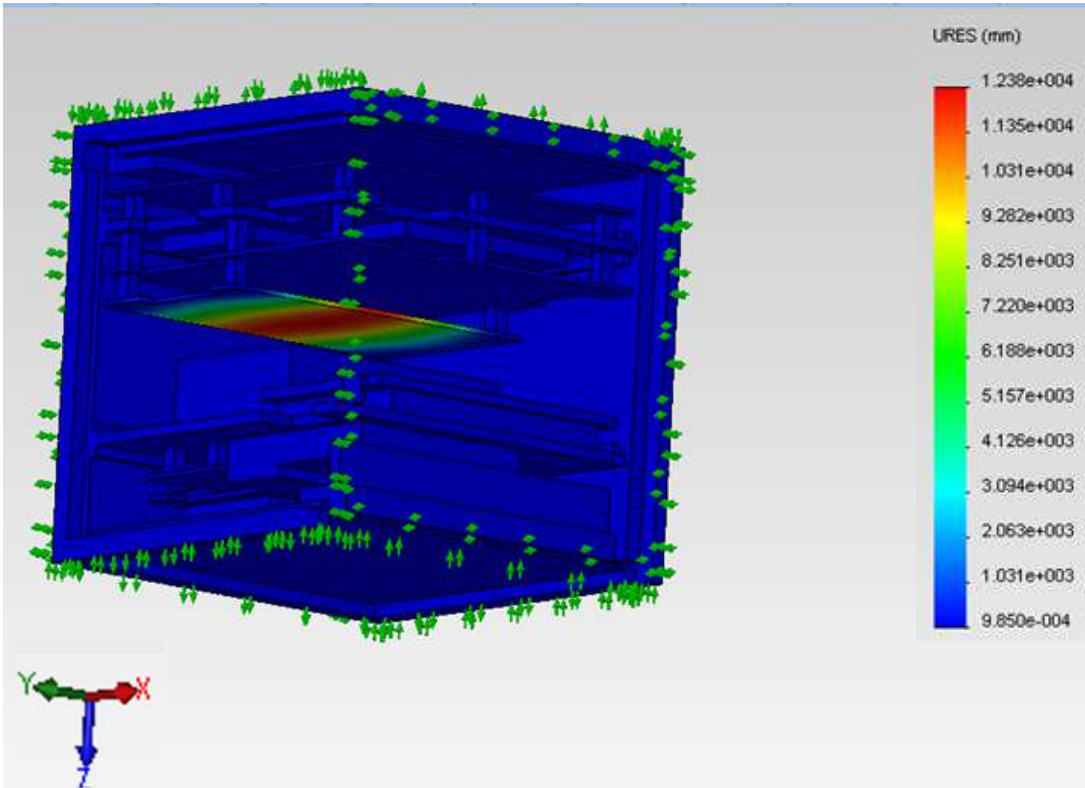


Figure A-9. AGS2 3rd mode natural frequency

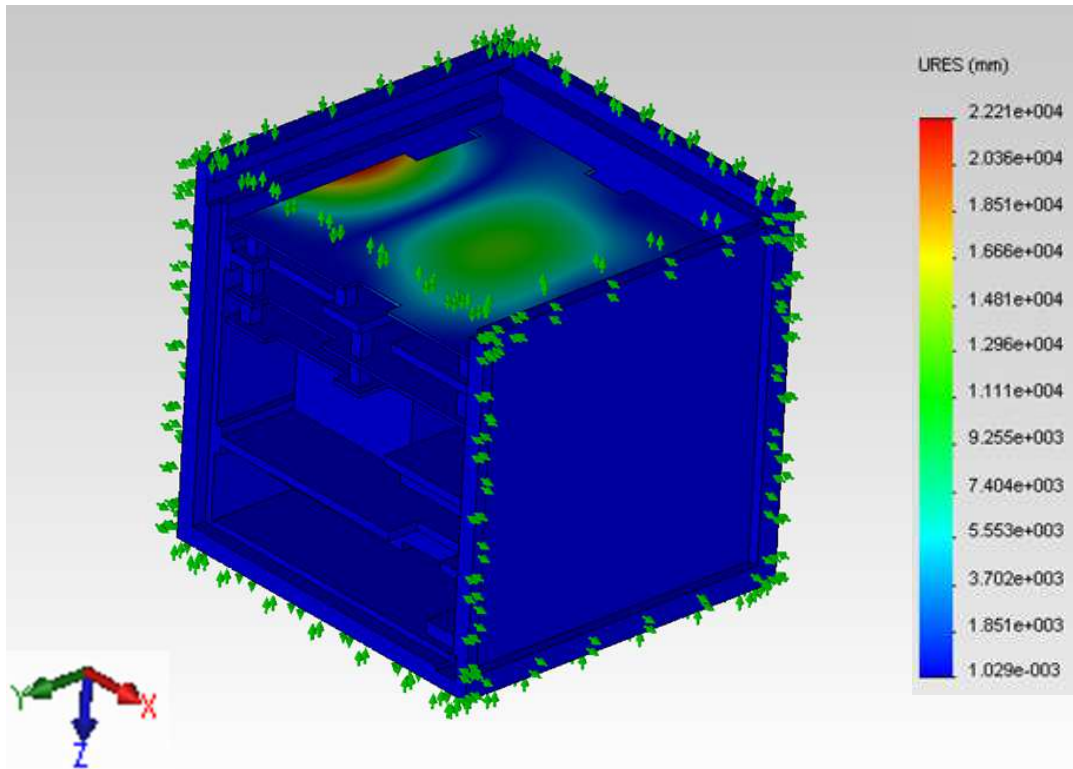


Figure A-10. AGS2 4th mode natural frequency

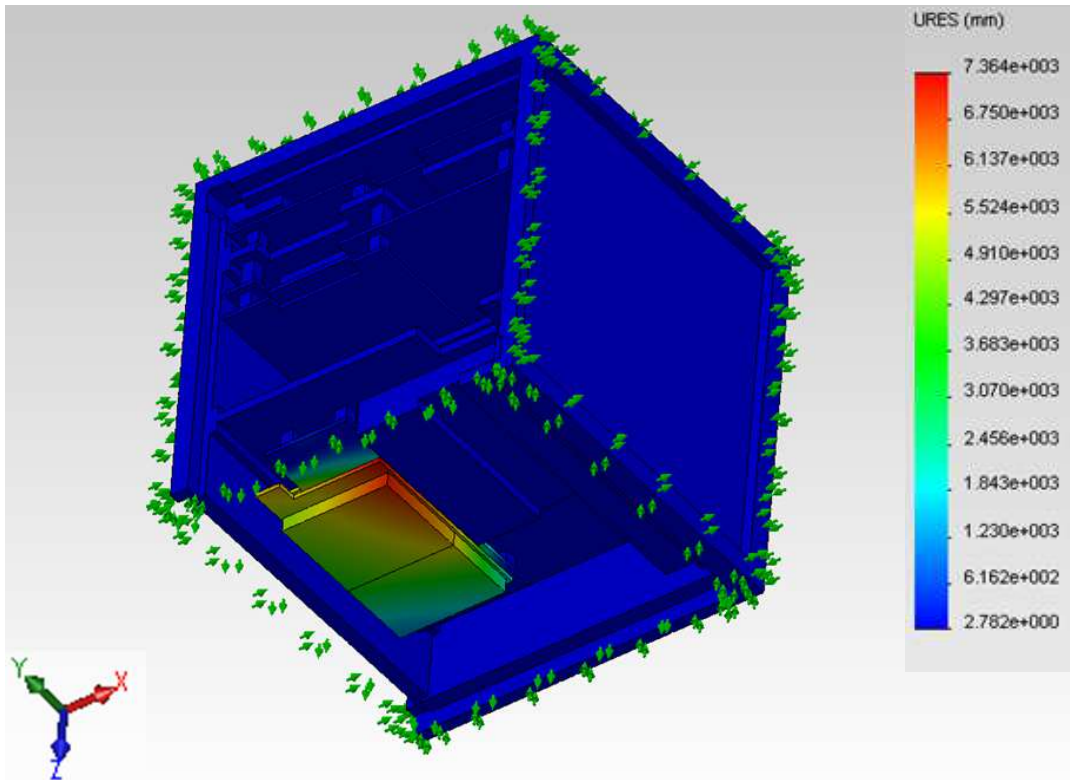


Figure A-11. AGS2 5th mode natural frequency

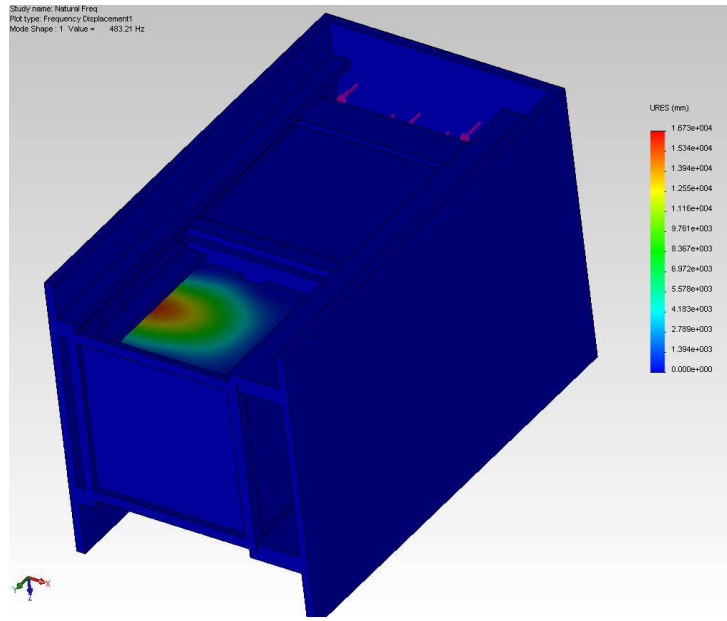


Figure A-12. DragonSat and SSPL 1st mode natural frequency

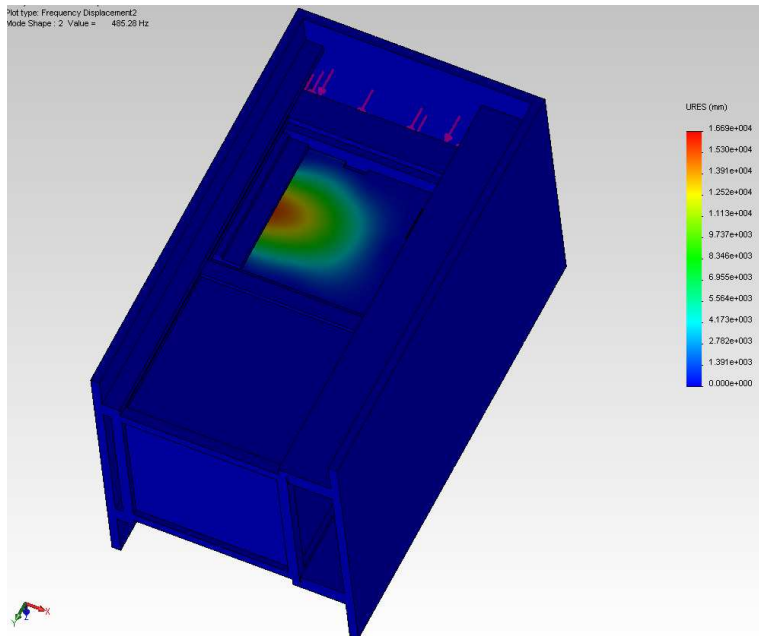


Figure A-13. DragonSat and SSPL 2nd mode natural frequency

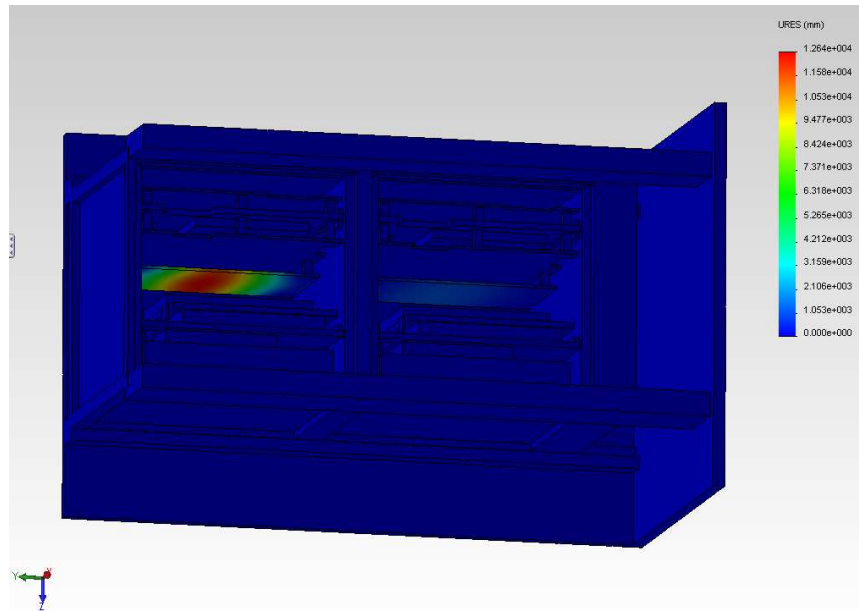


Figure A-14. DragonSat and SSPL 3rd mode natural frequency

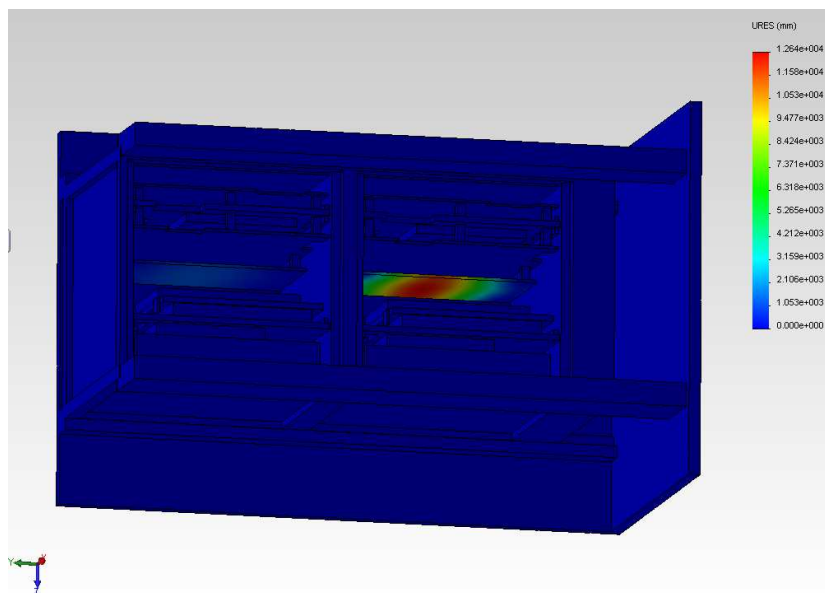


Figure A-15. DragonSat and SSPL 4th mode natural frequency

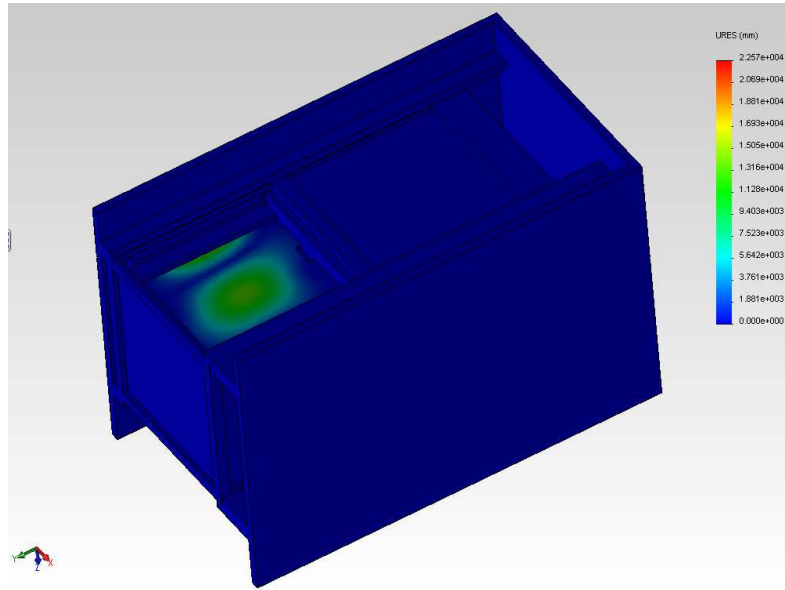


Figure A-16. DragonSat and SSPL 5th mode natural frequency

TO: Vincent Riot, Lead Systems Developer, Lawrence Livermore National Laboratory
FROM: Angela McLelland, Master's Candidate, Texas A&M University
DATE: February 6, 2012
SUBJECT: Validation of SolidWorks Professional 2011 for Transient Thermal Modeling

This memorandum will serve to summarize the validation test utilized by Texas A&M University, TAMU, in ensuring SolidWorks Professional 2011 a viable tool for transient heat transfer analyses. Such an investigation was meant to develop confidence in the SolidWorks package and to aid in the upcoming thermal strap design requested by Lawrence Livermore National Laboratory, LLNL. While not completely representative of specific on-orbit conditions, the model employed for this simulation captured general features of space missions, such as radiation heat loads and subsequent thermal responses. Additionally, the simulation had both a reliable and verifiable analytic solutions which allowed for expedited assurance in the tool.

Contextual Background

As requested, TAMU has started studying potential thermal strap designs for use on the Colony II bus. Nominally, these straps must have the ability to efficiently removing heat from the hot side of a Peltier Electric Cooler, PEC. Because heat removal from a PEC is the limiting design constraint it is imperative that the straps provide ample avenues for heat transfer yet do not unnecessarily increase the overall mass of satellite. To achieve such a design, TAMU will use SolidWorks Professional 2011 to generate consistently accurate proofs of design.

The Model

For the purposes of verifying temperature profiles generated by SolidWorks, a one dimensional, ceramic 'wall' was modeled with a 1000°C radiation load on the right side of the wall and the left side exposed to room air, see Figure 1.

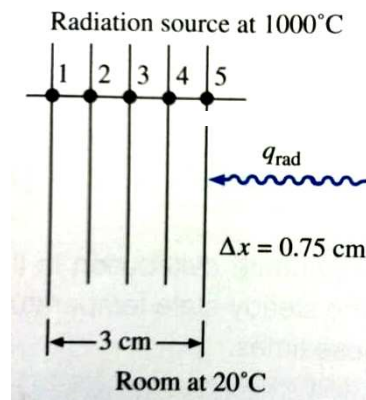


Figure 1: Nodal System [1]

The thickness of the wall was specified as 3cm and the height and length were 160 times larger, to neglect boundary conditions. An initial temperature of 20°C was applied to the entire wall and the simulation was run for a total of 150 sec. A probe was used to measure the temperature at five nodes at the center section of the wall, Figure 2, and the following results were obtained.

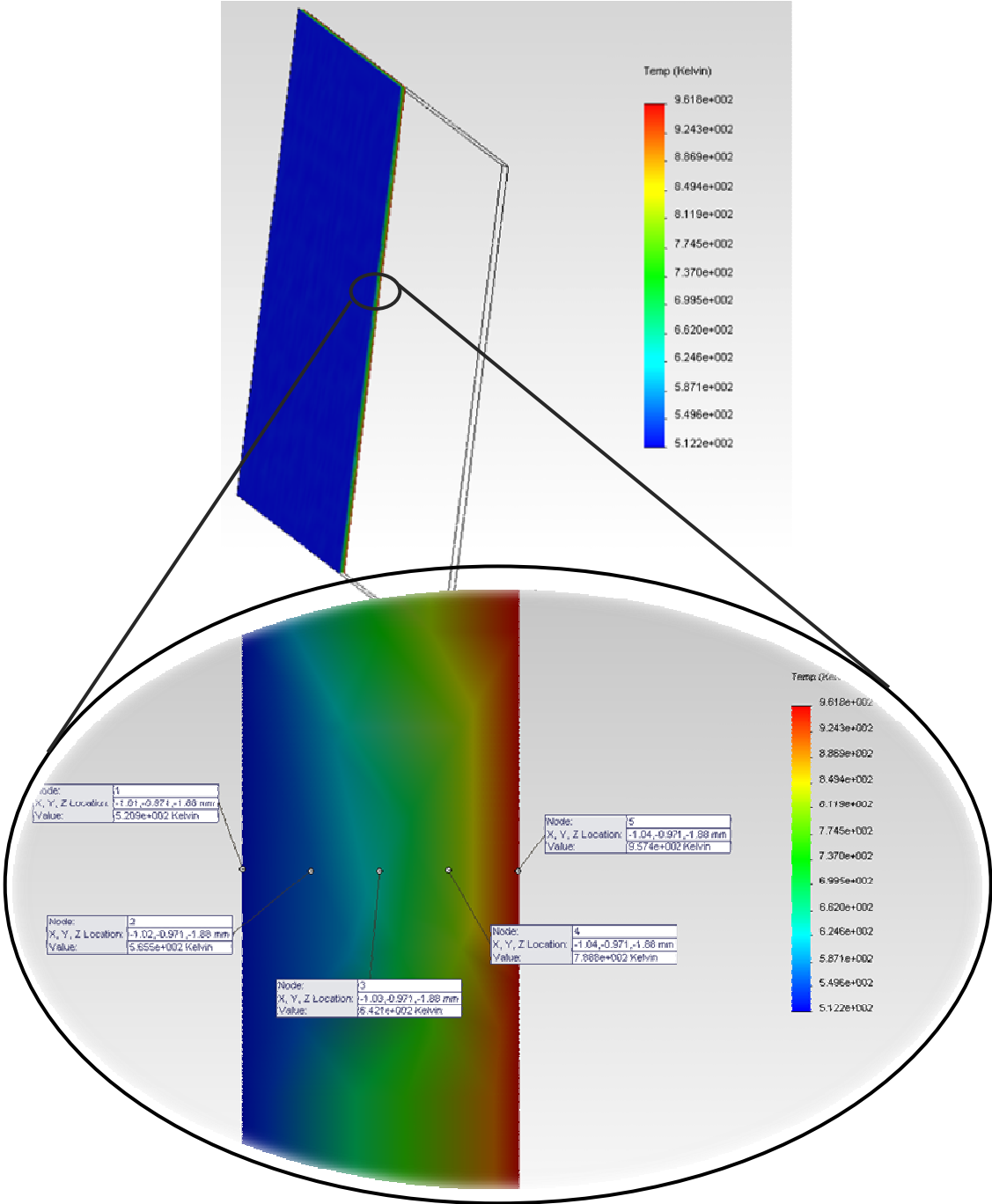


Figure 2: Probed locations for transient results

Transient Results

The final temperatures at these locations were then plotted to produce a rough temperature profile through the wall's cross section, Figure 3 (Right). Furthermore, temperatures at the outer nodes were measured at 520°K on the left side of the wall and 960°K on the right side of wall. As can be seen, these results identically match the expected results of the simulation, Figure 3 (Left), which were obtained through numerical methods applied at the each of the five nodes.

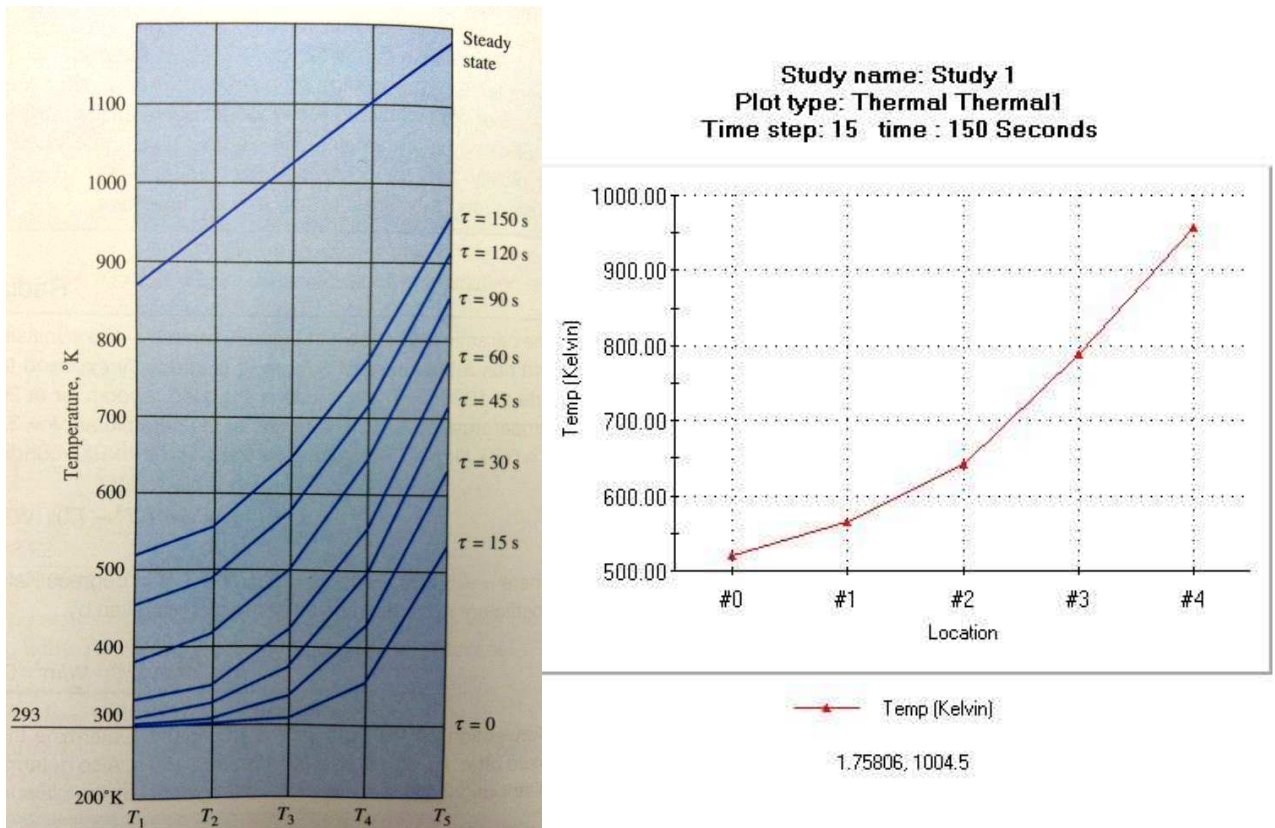


Figure 3: Published transient response (Left), SolidWorks generated response at 150 sec. (Right)

This test confirmed SolidWorks as a viable tool for solving transient heat transfer problems with radiation loads and provided an opportunity to explore the user interface with which future analyses will be tested. Ideally, this assessment would lead to additional testing of available PEC modules in SolidWorks, using an upgraded flow packages. Due to the cost prohibitive nature of this option however, the current test plan will involve an iterative process that uses hand calculations, orbit propagations, and simplified SolidWorks models to hone in on realistic PEC behavior.

Specifically, this process will include 1D numerical calculations, with margin, to develop a basic sizing standard. Conjointly, simplified flux boundary conditions will be explored as a possible alternative to actual PEC modules in SolidWorks. Both the results of this simulation and 1D calculations will then be compared to the results of a simplified laboratory test in order to ensure the physical performance of the PEC is being accurately represented. If testing proves this approach to be inaccurate, a secondary approach could involve utilizing Matlab and SolidWorks to generate orbit propagations, accurate emissivity and view factor values, and a steady state/long term transient thermal model of the entire 3U system. While this model would not feature the imager, representative heat loads would be modeled where appropriate. The steady state temperature results, gained from this simulation, would then be used as input boundary conditions for a simplified SolidWorks strap model that would approximate the PEC interface.

Further consideration is still needed in order to more directly capture physical PEC behavior, as TAMU's current SolidWorks package does not have this functionality. TAMU will therefore continue to research cost effective software to achieve this goal while maintaining progress on the aforementioned plan.

If you have any questions or comments, please do not hesitate to contact me at: mclelland.angela@gmail.com.

Reference(s): Holman, J. P. *Heat Transfer*. New York: McGraw-Hill, 1981. Print